Analysis and design of novel electromagnetic metamaterials

Analysis and Design of Novel Electromagnetic Metamaterials

by

Yunchuan Guo

Doctoral Thesis

Submitted in partial fulfilment of the requirements for the award of

Doctor of Philosophy of Loughborough University

April 2006

To my parents

Abstract

This thesis introduces efficient numerical techniques for the analysis of novel electromagnetic metamaterials. The modelling is based on a Method of Moments modal analysis in conjunction with an interpolation scheme, which significantly accelerates the computations. Triangular basis functions are used that allow for modelling of arbitrary shaped metallic elements. Unlike the conventional methods, impedance interpolation is applied to derive the dispersion characteristics of planar periodic structures.

With these techniques, the plane wave and the surface wave responses of fractal structures have been studied by means of transmission coefficients and dispersion diagrams. The multiband properties and the compactness of the proposed structures are presented. Based on this method, novel planar left-handed metamaterials are also proposed. Verifications of the left-handedness are presented by means of full wave simulation of finite planar arrays using commercial software and lab measurement. The structures are simple, readily scalable to higher frequencies and compatible with low-cost fabrication techniques.

Key words: metamaterial, electromagnetic band gap (EBG), artificial magnetic conductor (AMC), left-handed material (LHM), fractal, method of moments (MoM), impedance matrix interpolation, dispersion diagram.

Acknowledgements

I would like to thank my supervisors, Dr. Alexandros Feresidis and Professor Yiannis Vardaxoglou, for their constructive input and support. I would also like to thank a number of other people who have contributed to this work including Dr. George Goussetis and Mr. Shenhong Wang. I am also grateful to my dear parents and my girlfriend Lisha for their kindly encouragements. I would also like to express my gratitude towards the Department of Electronics and Electrical Engineering, Loughborough University, for funding this work.

Publications from the research work of this thesis:

Journals

1. Y. Guo, G. Goussetis, A.P. Feresidis and J.C. Vardaxoglou, "Experimental Validation of Uniplanar Left-Handed Metamaterials", submitted to *IEEE Microwave and Wireless Components Letters*

2. Y. Guo, G. Goussetis, A.P. Feresidis and J.C. Vardaxoglou, "Efficient Modelling of Novel Uniplanar Left-Handed Metamaterials", *IEEE Transactions on Microwave Theory and Techniques*, April 2005

3. G. Goussetis, A.P. Feresidis, S. Wang, Y. Guo and J.C. Vardaxoglou, "Uniplanar Left-Handed Artificial Metamaterials", *Journal of Optics A: Pure and Applied Optics*, February 2005

4. Y. Guo, A.P. Feresidis, G. Goussetis and J.C. Vardaxoglou, "Efficient Modelling Technique for Fractal Electromagnetic Band-Gap Arrays", *IEE Proceedings – Science, Measurement and Technology*, November 2004

Conferences

1. G. Goussetis, A. P. Feresidis, Y. Guo, and J. C. Vardaxoglou, "Novel Planar Negative Refractive Index Metamaterials", *2005 IEEE AP-S International Symposium and URSI North American Radio Science Meeting*, USA, July 2005

2. Y. Guo, A.P. Feresidis and J.C. Vardaxoglou, "Analysis and Design of Uniplanar Left-Handed Metamaterials", *Loughborough Antennas and Propagation Conference*, UK, April 2005

3. G. Goussetis, A. P. Feresidis, **Y.** Guo, and J. C. Vardaxoglou, "Novel Planar Left-Handed Metamaterials", *EPFL Latsis Symposium 2005*, Switzerland, February 2005

4. J. C. Vardaxoglou, A. P. Feresidis, G. Goussetis, S. Wang and Y. Guo, "Metallodielectric EBG Surfaces: Miniaturisation, Tunability and Antenna Applications", *First Workshop of the METAMORPHOSE NoE*, Belgium, November 2004

5. G. Goussetis, Y. Guo, A.P. Feresidis and J.C. Vardaxoglou, "Miniaturised and Multiband Artificial Magnetic Conductors and Electromagnetic Band Gap Surfaces", *2004 IEEE AP-S International Symposium and URSI North American Radio Science Meeting*, USA, June 2004

6. Y. Guo, A.P. Feresidis, G. Goussetis and J.C. Vardaxoglou, "Efficient Modelling of Novel Fractal Loaded Electromagnetic Band Gap Arrays", *Fifth International Conference on Computation in Electromagnetics*, UK, April 2004

Contents

List of Figures

1. Introduction

1.1 Metamaterials

Electromagnetic metamaterials are artificial structures that can be designed to exhibit specific electromagnetic properties not commonly found in nature. The prefix "meta" means "beyond" in Greek. These structures are regarded as metamaterials because they are beyond our experience and the descriptions we give to normal bulk materials. They are usually fabricated as periodic arrays of metal elements embedded in stratified dielectric substrates. A large variety of elements can be used such as dipoles, tripoles, patches and rings. Some examples of element geometries are shown in Fig. 1.1. These elements may be arranged in a rectangular double-periodic grid or an off-axis triangular lattice.

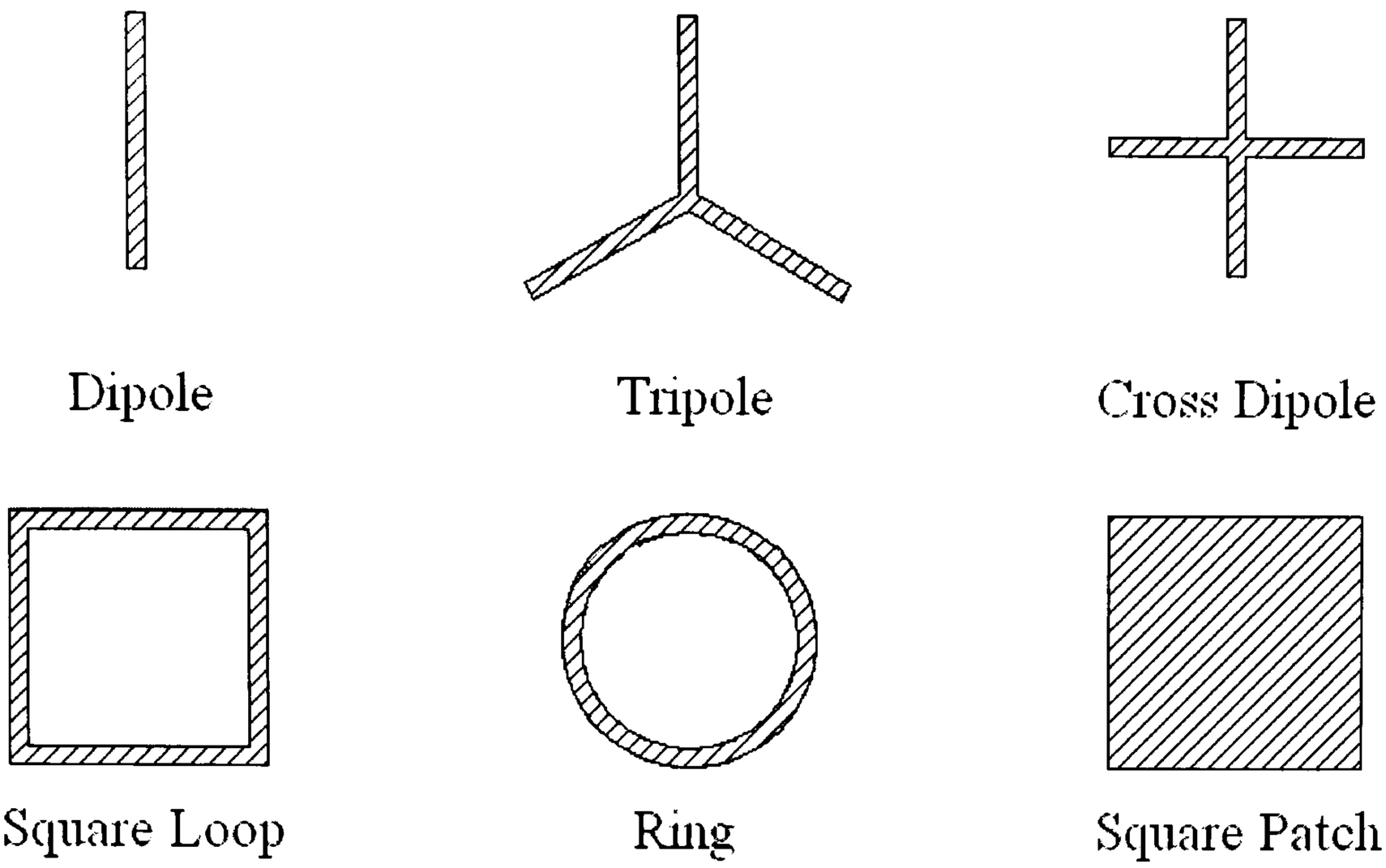

Fig. 1.1 Some array element geometries.

In recent years, these structures are widely applied in antennas for fixed and mobile communications system because of their interesting features when interacting with electromagnetic waves. According to the different responses to electromagnetic waves, metamaterials are classified as follows:

- Frequency Selective Surfaces (FSS)
- Electromagnetic Band Gap Materials (EBG)
- Artificial Magnetic Conductors (AMC)
- Left-handed Materials (LHM)

Frequency Selective Surfaces (FSS), which have band gap characteristics for an incident plane wave, have been analyzed by many researchers in the past several decades [1]-[10]. Fig. 1.2 is the typical response of an FSS made of conducting elements. The band gap (or stopband) has been highlighted with grey colour. The resonant frequency f_0 depends on the dimensions of the elements as well as the

periodicity. Approximately, the wavelength of resonance is twice the element length for a dipole array, four times of arm length for a tripole array, and equals to the perimeter of the element for a loop array, as is shown in Fig. 1.3. For this frequency selectivity, the Frequency Selective Surfaces are normally used as plane-wave filters and antenna radomes.

The concept of Electromagnetic Band Gap (EBG) materials was formerly introduced by Yablonovitch as Photonic Band Gap (PBG) crystals [11], which prevent the propagation of electromagnetic waves in specified frequency bands. Traditional PBG crystals are made of two different dielectric materials with a periodicity in one, two or three dimensions. Extending this concept, electromagnetic materials named Metallodielectric Photonic Band Gap (MPBG) materials based on metallic elements have emerged, which show characteristics of frequency band gaps for microwaves and millimetre-waves [12], [13]. These materials are generally classified as Electromagnetic Band Gap materials[14]. Unlike FSS, EBG materials are utilised for filtering bounded surface waves. The dispersion diagram of an tripole EBG array on a triangular lattice with skewed angle of 60 degrees is shown in Fig. 1.4. The bold lines in the dispersion diagram indicate the propagation modes along the contour of the irreducible Brillouin zone. The frequency ranges, in which there are not any propagation modes, are the surface wave band gaps of the EBG material. Many applications of EBG materials have been made in antenna and microwave designs in order to enhance antenna gain, and achieve lower back radiation and lower mutual coupling [15]-[20].

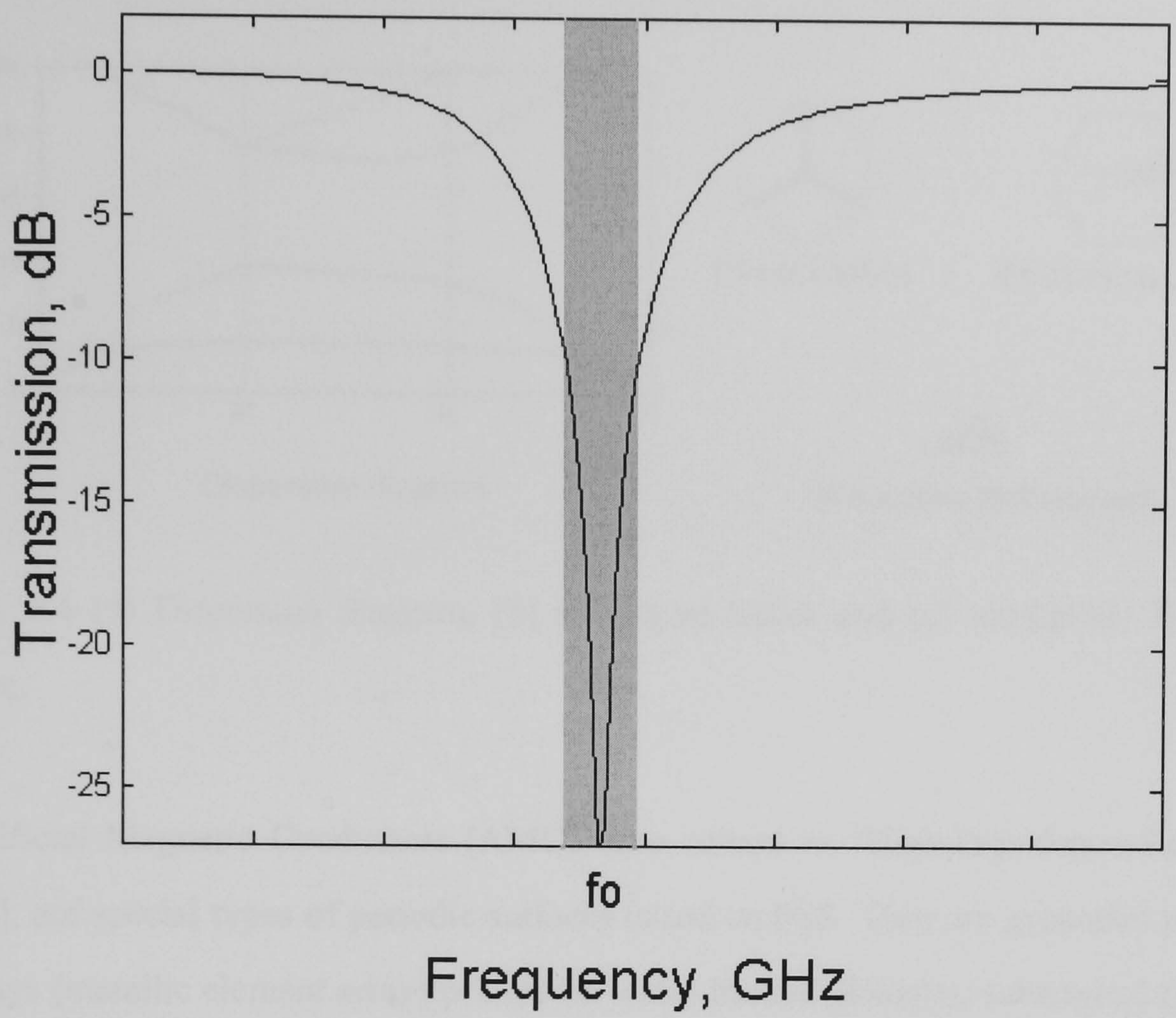

Fig. 1.2 Transmission coefficient of FSS.

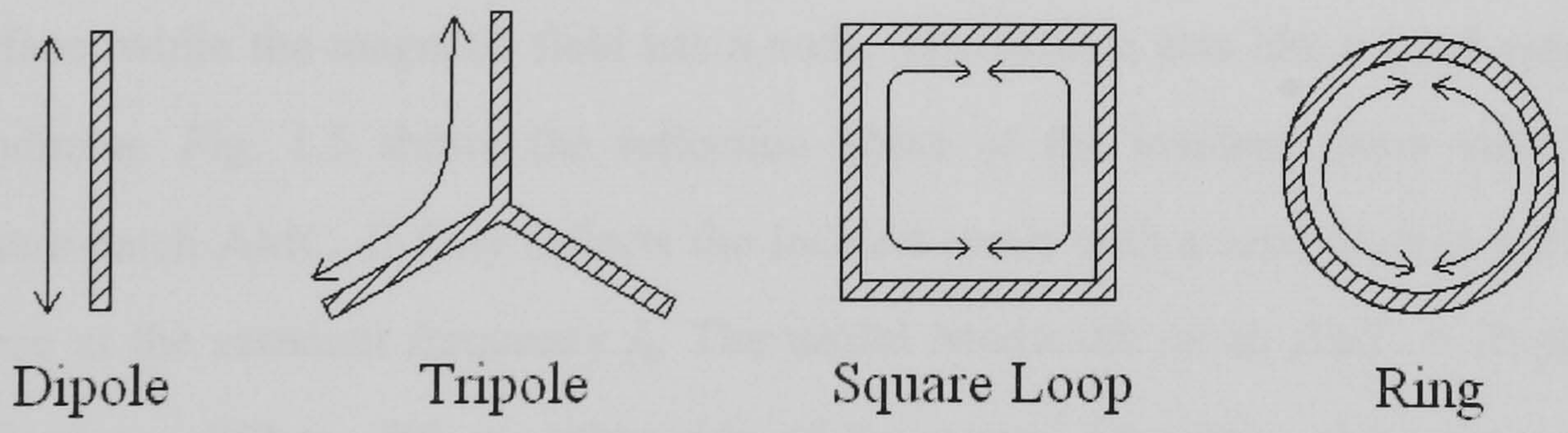

Fig. 1.3 Element geometries and half wavelength.

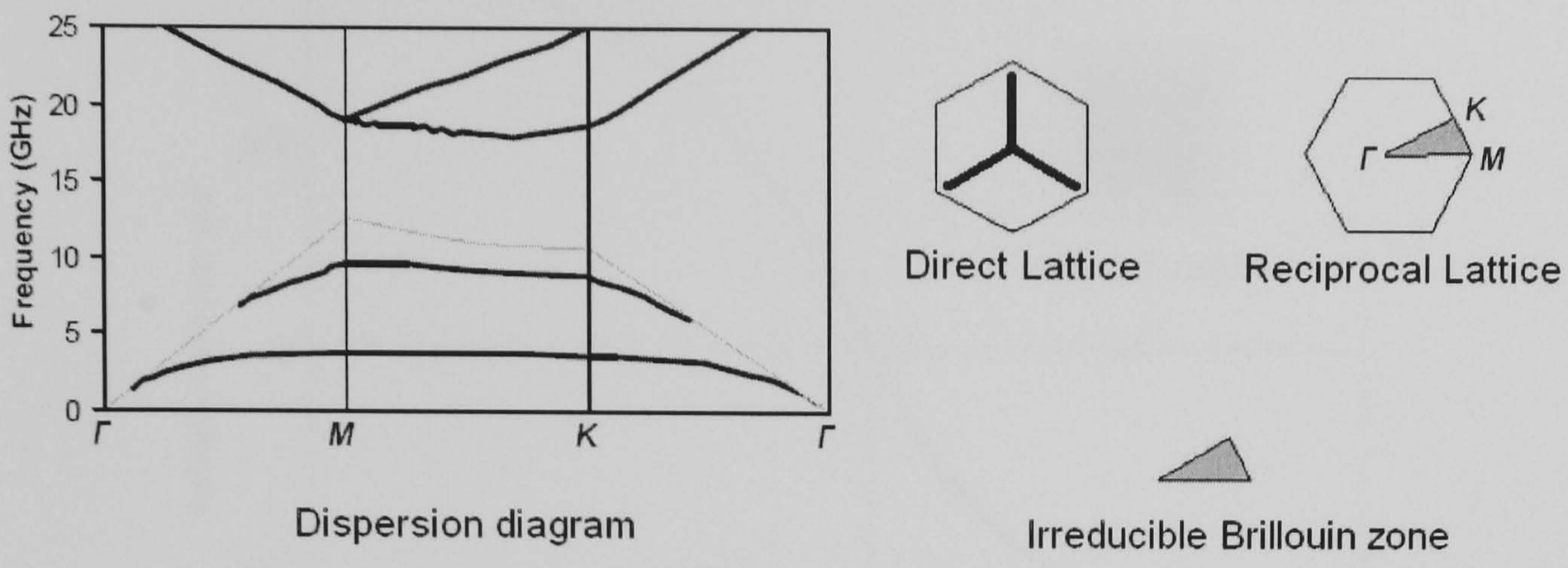

Fig. 1.4 (a) Dispersion diagram, (b) reciprocal lattice and (c) irreducible Brillouin zone.

Artificial Magnetic Conductors (AMC), also named as "High-Impedance Surfaces" [21], are special types of periodic surfaces based on FSS. They are grounded periodic arrays (metallic element arrays printed on metal-backed dielectric substrates) showing a high surface impedance under plane wave incidence. The common metal surface, which is a good electric conductor, has low impedance. With plane wave incidence, the electric field has a node at the surface, and the magnetic field has an antinode. In contrast, for the High-Impedance Surfaces, the electric field has an antinode at the surface, while the magnetic field has a node. The surface acts like a good magnetic conductor. Fig. 1.5 shows the reflection phase of the incident plane wave by a square-patch AMC. It fully reflects the incident wave with a zero degrees reflection phase at the resonant frequency f_0. The useful bandwidth of an AMC is in general defined as +90° to -90° on either side of the central frequency, since these phase values would not cause destructive interference between direct and reflected waves. With these features, AMCs have been applied to low-profile resonant cavity antennas and microstrip patch antennas [22]-[24].

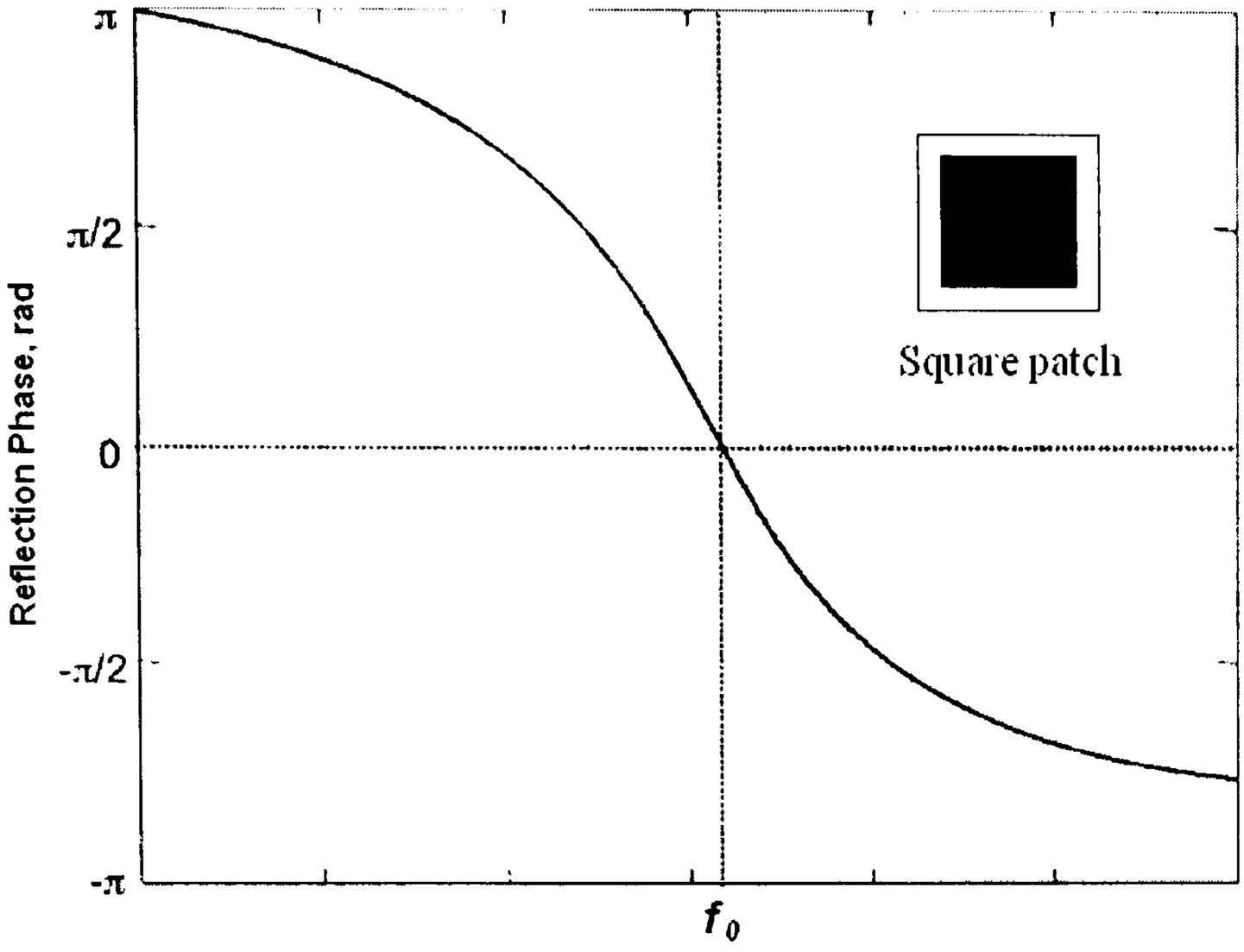

Fig. 1.5 Reflection phase of AMC.

Left-Handed Materials (LHM) were first theorized by Veselago as double negative materials (DNG) for their simultaneously negative permittivity (ε) and permeability (μ) [25]. The term "left-handed" describes the fact that the vectors **E**, **H** and **k** form a left-handed triplet, instead of a right-handed triplet, as is the case in conventional right-handed (RH) media. Inside this kind of materials, the unique electromagnetic properties as reversal of Snell's Law, the Doppler Effect and the Cerenkov Effect are anticipated. Although Veselago's prediction was brought out in 1967, experimental verifications of the effective permeability and the left-handedness were presented by Pendry [26] and Smith [27] three decades later. Smith's LHM is three dimensional multi-layered arrays of metallic split ring resonators (SRR) and thin metallic wires. In recent years, based on the transmission line approach, planar LHM have been designed by other researchers [28]-[30]. Compared with Smith's LHM, these structures have much broader bandwidth and lower profile, and are more suitable for microwave applications [31]-[35].

1.2 Computational Electromagnetics

1.2.1 Numerical Methods

Electromagnetic scattering problems could be described by either integral equations or differential equations. Method of Moments (MoM) is the most general and widely used approach for integral equations. By applying MoM, the unknown quantity (usually the surface current density) is approximated as a linear series of known functions (basis functions) multiplied by unknown coefficients. After substituting the approximation into the field integral equation, both sides of the equation are multiplied by suitable functions (testing functions) and are integrated in the testing domain. In order to yield the unknown coefficients, the linear system can be solved using either matrix inversion or an iterative method.

Since the unknown quantity is formulated with integral equations in MoM, it also could be approximated using differential equations. Finite Difference (FD) method, Finite Element Method (FEM) and Transmission Line Method (TLM) are of this type. Not like those for integral equations, basis functions for differential equations must satisfy the boundary conditions and must be differentiable at least of the same order as is the order of the differential operator. To meet this requirement, an adaptive mesh is usually used to discrete the region of interest. Basis functions are selected based on the mesh nodes or the mesh edges. Once the discrete unknown values are determined, other unknown values can be obtained by interpolation.

Differential equation techniques are powerful in solving 3D complex problems. However, they have the disadvantage that the absorbing boundary conditions (ABC)

are required to produce a finite computational domain when analysing open structures, and they will lose much of the accuracy in solving the electric large problems. Integral equation techniques possess the advantage that open regions do not need the ABC, while the large amount of basis functions for complex geometries may lead to dense and large matrices, which make the simulation program to be a time-consuming monster. Each method has its own advantages and drawbacks. No matter which method we use, the final aim is always yielding the most accurate results with the least cost.

1.2.2 Commercial Software Packages

Commercial electromagnetic simulation software packages are used in the following chapters as the comparison and the validation of the numerical technique proposed in the thesis. These software packages are based on the numerical methods mentioned above.

Ansoft Designer™ [36], which is formerly Ensemble, is well known as software for microstrip structures and planar circuits. The simulation technique used in Designer is based on the mixed potential integral equation (MPIE) and Method of Moments (MoM). With the periodic Green's function, Designer becomes a powerful tool for two-dimensional (2D) periodic structures such as FSS and EBG. Surface current, transmission and reflection response can be plotted in the post-processing procedure.

Ansoft HFSS™ [37], which is one of the strongest three-dimensional (3D) simulators in computational electromagnetics (CEM), is another famous simulation tool by Ansoft Corporation. It brings the power of Finite Element Method (FEM) to the simulation of complex 3D electromagnetic structures by leveraging advanced

techniques such as automatic adaptive mesh generation and refinement, tangential vector finite elements, and Adaptive Lanczos Pade Sweep (ALPS) [38]. HFSS automatically computes multiple adaptive solutions until a user-defined convergence criterion is met. Field solutions to predict high frequency behaviours such as dispersion and the using of Periodic Boundary Conditions (PBC) enable HFSS to be the especial tool for EBG and LHM.

Micro-Stripes™ [39] is a 3D electromagnetic simulation software package distributed by Flomerics and is the most extensively used TLM based simulator. The most recent version, Micro-Stripes v6.5, offers a complete set of features that are usually required for electromagnetic simulations. Some of them are the advanced modelling interface, S-parameters calculation, non-uniform meshing (multi-gridding), Perfect Matched Layer (PML) absorbing boundary conditions and symmetry conditions such as electric and magnetic walls. By using features as multi-gridding and symmetry conditions, depending on the simulated geometry, the solution time can be significantly reduced. Good visualisation tools such as surface current, near field and 3D radiation patterns are also available.

1.3 Overview of the Thesis

This thesis begins with proposing an efficient numerical technique for electromagnetic metamaterials. This technique is based on the mixed potential integral equations (MPIE) and Method of Moments (MoM). Triangular patch sub-domain basis functions are adopted because they are more versatile in modelling of arbitrary-shaped elements than entire-domain basis functions and rooftop sub-domain basis functions. Considering the configurations of the metamaterials, periodic Green's function based on the Bloch-Floquet theorem and closed-form Green's function for

stratified dielectric media are used in setting up the MoM equations. Since the analysis of the metamaterials is mainly in the frequency domain, impedance matrix interpolation technique is applied to drastically speed up the computations in a wide frequency range.

With these methods, the research effort in this thesis focuses on the analysis and design of novel electromagnetic metamaterials. Miniaturised and multiband EBG, miniaturised and multiband AMC and planar LHM are proposed and investigated. These structures are arrays of compact and complex-shaped elements, such as fractal and spiral elements, over grounded dielectric substrates. To provide a description of the main properties of the EBG and LHM, dispersion diagrams of surface waves are produced by solving the homogeneous form of MoM equations. Leaky waves are not considered or investigated in this thesis. Finally, the calculated results are validated by the simulations using commercial software Ansoft HFSS and experimental measurements.

The outline of the chapters of the thesis is as follows:

Chapter 1 gives out a brief introduction to the background of this thesis. Classification and characterization of metamaterials are mentioned in this chapter. Commercial software packages used to compare with the proposed approach and their related numerical techniques are also introduced. The organisation of this thesis is outlined.

Chapter 2 introduces an efficient algorithm based on MPIE and MoM to solve the scattering problems of metamaterials. The goal of this algorithm is to model the arrays' arbitrary-shaped elements in stratified dielectric substrates. Periodic Green's functions are used for this modelling. Impedance Matrix Interpolation is applied to save the computing time. Surface current, plane-wave response and dispersion

diagram are plotted to visualize the output data in the post-processing procedure.

Chapter 3 applies the algorithm to EBG and AMC material designs. The goal of this chapter is to design miniaturised and multiband EBG and AMC surfaces. Several shapes of elements, such as fractal tripoles, convoluted tripoles and periodically loaded tripoles, are discussed in this chapter. The research focuses on the fractal tripoles EBG and AMC arrays. Transmission magnitude of FSS surfaces, dispersion diagram of EBG surfaces, and reflection phase of AMC surfaces are produced in the analysis. The miniaturised and multiband features are proved by these simulations and validated by the measurement results.

Chapter 4 introduces the rationale of LHM and describes the application of the analysis method in order to produce LHM designs. The goal of this chapter is to design planar LHM in the absence of grounding vias. The investigation includes a closed rectangular loop, a split rectangular loop and two variations of the split loop that increase magnetic and electric effects according to the dual transmission line concept for LHM. Further to these structures, an isotropic design of spiral arrays in square unit cells is presented. The left-handedness of these designs is proved by the dispersion diagrams and validated by a full-wave simulation of finite structures using HFSS.

Chapter 5 describes the design of the experiment as well as the measured results that confirm that this left-handed propagation can be observed in practice. The measurement is based on microstrip transmission line models, which are partly replaced by the planar left-handed materials. According to the dispersion diagram, power can be delivered through these structures in the frequency ranges where there are the left-handed and right-handed modes. While in the other frequency ranges, the structures show band-gap features. The left-handed propagation is proved by

measuring the phase difference between the two ports of these structures.

Chapter 6 finally draws the conclusions from the work presented in this thesis. Results in the previous chapters are discussed. Further improvements of the numerical scheme for more requirements in modelling and computing are considered and future developments are proposed.

References

[1] J. C. Vardaxoglou, *Frequency Selective Surfaces: Analysis and Design*, Research Studies Press Ltd., Taunton, 1997

[2] T. K. Wu, *Frequency Selective Surface and Grid Array*, John Wiley & Sons, Inc., New York, 1995

[3] B. A. Munk, *Frequency Selective Surfaces: Theory and Design*, John Wiley & Sons, Inc., New York, 2000

[4] R. Mittra, C. H. Chan, and T. Cwik, "Techniques for Analyzing Frequency Selective Surfaces-A Review", *Proceedings of IEEE*, Vol. 76, no. 12, pp. 1593-1615, 1988

[5] R. Pous, and D. M. Pozar, "A Frequency-Selective Surface Using Aperture-Coupled Microstrip Patches", *IEEE Trans. Antennas Propag.*, Vol. 39, no. 12, pp. 1763-1769, 1991

[6] E. A. Parker, and A. N. A. El Sheikh, "Convoluted Array Elements and Reduced Size Unit Cells for Frequency-Selective Surfaces", *IEE Proceedings - Microwaves, Antennas and Propagation.*, Vol. 138, no. 1, pp. 19-22, 1991

[7] A. Janhsen, and V. Hansen, "Arrays of Finite or Infinite Extent in Multilayered Media for Use as Passive Frequency-Selective Surfaces", *IEE Proceedings - Microwaves, Antennas and Propagation.*, Vol. 138, no. 1, pp. 1-8, 1991

[8] B. Philips, E. A. Parker, and R. J. Langley, "Finite Curved Frequency Selective Surfaces", *Electronic Letters*, Vol. 29, no. 10, pp. 882-883, 1993

[9] T. R. Schimert, A. J. Brouns, C. H. Chan, and R. Mittra, "Investigation of Millimeter-Wave Scattering from Frequency Selective Surfaces", *IEEE Trans. Microwave Theory Tech.*, Vol. 39, no. 2, pp. 315-322, 1991

[10]C. Antonopoulos, R. Cahill, E. A. Parker, and I. M. Sturland, I.M, "Multilayer Frequency-Selective Surfaces for Millimetre and Submillimetre Wave Applications", *IEE Proceedings - Microwaves, Antennas and Propagation.*, Vol. 144, no. 6, pp. 415-420, 1997

[11] E. Yablonovitch, "Inhibited Spontaneous Emission in Solid-State Physics and Electronics", *Phys. Rev. Lett.*, Vol. 58, no. 20, pp. 2059-2062. 1987

[12] Y. L. R. Lee, A. Chauraya, D. S. Lockyer, and J. C. Vardaxoglou, "Dipole and Tripole Metallodielectric Photonic Band Gap (MPBG) Structures for Microwave Filter and Antenna Applications", *IEE Proc. Optoelectron.*, Vol. 147, no. 6, pp. 395-400, 2000

[13] A. P. Feresidis, G. Apostolopoulos, N. Serfas, and J. C. Vardaxoglou,, "Closely Coupled Metallodielectric Electromagnetic Band-Gap Structures Formed by Double-Layer Dipole and Tripole Arrays", *IEEE Trans. Antennas Propag.*, Vol. 52, no. 5, pp. 1149-1158, 2004

[14] Y. Rahmat-Samii, and H. Mosallaei, "Electromagnetic Band-gap Structures: Classification, Characterization, and Applications", *Eleventh International Conference on Antennas and Propagation, IEE Conf. Publ.* no. 480, Vol. 1, pp.

560-564, 2001

[15] A. P. Feresidis, and J. C. Vardaxoglou, "High gain planar antenna using optimised partially reflective surfaces", *IEE Proc. Microw. Antennas Propag.* Vol. 148, no. 6, pp. 345-350, 2001

[16] F. Yang, and Y. Rahmat-Samii, "A Low Profile Circularly Polarized Curl Antenna over Electromagnetic Band Gap (EBG) Surface", *Microw. Opt. Technol. Lett.*, Vol. 31, no. 4, pp. 264-267, 2001

[17] F. Yang, and Y. Rahmat-Samii, "Microstrip Antennas Integrated with Electromagnetic Band-Gap (EBG) Structures: A Low Mutual Coupling Design for Array Applications", *IEEE Trans. Antennas Propag.*, Vol. 51, no. 10, pp. 2936-2946, 2003

[18] R. Gonzalo, P. Maaget, and M. Sorolla, "Enhanced Patch Antenna Performance by Suppressing Surface Waves Using Photonic Bandgap Substrates", *IEEE Trans. Microwave Theory Tech.*, Vol. 47, no. 11, pp. 2131-2138, 1999

[19] H. Hsu, M. J. Hill, J. Papapolymerou, and R. W. Ziolkowski, "A Planar X-Band Electromagnetic Band-Gap (EBG) 3-Pole Filter", *IEEE Microwave and Wireless Components Letters*, Vol. 12, no. 7, pp. 255-257, 2002

[20] F. Elek, R. Abhari, and G. V. Eleftheriades, "A Uni-Directional Ring-Slot Antenna Achieved by Using an Electromagnetic Band-Gap Surface", *IEEE Trans. Antennas Propag.*, Vol. 53, no. 1, pp. 181-190, 2005

[21] D. Sievenpiper, L. Zhang, R. F. J. Broas, N. G. Alexopolous, and E. Yablonovitch, "High-Impedance Electromagnetic Surfaces with a Forbidden Frequency Band", *IEEE Trans. Microwave Theory Tech.*, Vol. 47, no. 11, pp. 2059-2074, 1999

[22] S. Wang, A. P. Feresidis, G. Goussetis, and J. C. Vardaxoglou, "Low-Profile Resonant Cavity Antenna with Artificial Magnetic Conductor Ground Plane", *Electron. Lett.*, Vol. 40, no. 7, pp. 405-406, 2004

[23] A. P. Feresidis, G. Goussetis, S. Wang, and J. C. Vardaxoglou, "Artificial Magnetic Conductor Surfaces and Their Application to Low-Profile High-Gain Planar Antennas", *IEEE Trans. Antennas Propag.*, Vol. 53, no. 1, pp. 209-215, 2005

[24] A. Erentok, P. L. Luljak, and R. W. Ziolkowski, "Characterization of a Volumetric Metamaterial Realization of an Artificial Magnetic Conductor for Antenna Applications", *IEEE Trans. Antennas Propag.*, Vol. 53, no. 1, pp. 160-172, 2005

[25] V. G. Veselago, "The Electrodynamics of Substances with Simultaneously Negative Values of ε and μ", *Sov. Phys. Usp.*, Vol. 10, no. 4, pp. 509-514, 1968

[26] J. B. Pendry, A. J. Holden, D. J. Robbins, and W. J. Stewart, "Magnetism from Conductors and Enhanced Nonlinear Phenomena", *IEEE Trans. Microwave Theory Tech.*, Vol. 47, no. 11, pp. 2075-2084, 1999

[27] D. R. Smith, Willie J. Padilla, D. C. Vier, S. C. Nemat-Nasser and S. Schultz, "A Composite Medium with Simultaneously Negative Permeability and Permittivity", *Phys. Rev. Lett.*, Vol. 84, no. 18, pp. 4184-4187, 2000

[28] G. V. Eleftheriades, A. Iyer and P. Kremer, "Planar Negative Refractive Index Media Using Periodically L-C Loaded Transmission Lines", *IEEE Trans. Microwave Theory Tech.*, Vol. 50, no 12, pp. 2702-2711, 2002

[29] A. Sanada, C. Caloz and T. Itoh, "Planar Distributed Structures With Negative Refractive Index", *IEEE Trans. Microwave Theory Tech.*, Vol. 52, no. 4, pp. 1252–1263, 2004

[30] G. Goussetis, A. P. Feresidis, S. Wang, Y. Guo, and J. C. Vardaxoglou, "Planar Left-Handed Artificial Metamaterials", *J. Opt. A: Pure Appl. Opt.* Vol. 7, no. 2, pp. S44–S50, 2005

[31] M. A. Antoniades, G. V. Eleftheriades, "Compact Linear Lead/Lag Metamaterial Phase Shifters for Broadband Applications", *IEEE Antennas Wireless Propag. Lett.*, Vol. 2, pp. 103-106, 2003

[32] S. Lim, C. Caloz, T. Itoh, "Metamaterial-Based Electronically Controlled Transmission-Line Structure as a Novel Leaky-Wave Antenna with Tunable Radiation Angle and Beamwidth", *IEEE Trans. Microwave Theory Tech.*, Vol. 53, no. 1, pp. 161–173, 2005

[33] H. Kim; A. B. Kozyrev, A. Karbassi, and D. W. van der Weide,"Linear Tunable Phase Shifter Using a Left-Handed Transmission Line", *IEEE Microwave and Wireless Components Letters*, Vol. 15, no. 5, pp. 366-368, 2005

[34] M. A. Antoniades, G. V. Eleftheriades, "A Broadband Wilkinson Balun Using Microstrip Metamaterial Lines", *IEEE Antennas Wireless Propag. Lett.*, Vol. 4, pp. 209-212, 2005

[35] M. A. Antoniades, G. V. Eleftheriades, "A Broadband Series Power Divider Using Zero-Degree Metamaterial Phase-Shifting Lines", *IEEE Microwave and Wireless Components Letters*, Vol. 15, no. 11, pp.808-810, 2005

[36] *Ansoft Designer*, ver. 2.0, Ansoft Corporation, 2004

[37] *High Frequency Structure Simulator* (HFSS), ver. 9.0, Ansoft Corporation, 2003

[38] D. K. Sun, Z. Cendes, J. F. Lee, "ALPS-A New Fast Frequency-Sweep Procedure for Microwave Devices", *IEEE Trans. Microwave Theory Tech.*, Vol. 49, no. 2, pp. 398-402, 2001

[39] *Micro-Stripes*, ver. 6.5, Flomerics, 2004

2. Modelling Techniques for Metamaterials

2.1 Introduction

As is discussed in Chapter 1.2, Method of moments (MoM) is a versatile approach for open region problems of stratified planar structures. A general model of metamaterials is analysed in this chapter using MoM to solving mixed potential integral equation (MPIE). The MPIE requires a less singular vector potential to evaluate the mutual impedance integral, while in the electric field integral equation (EFIE) the two-dimensional infinite integrals with highly oscillating and slowly decaying integrands cannot be avoided. Surface current on the simple regular-shape element, such as dipole, tripole and ring, can be expanded by the entire domain basis functions. For elements with complex shapes, sub-domain basis functions have to be applied. Two kinds of sub-domain basis functions are introduced in this chapter, namely the

rooftop basis function and the triangular patch basis function. Compared with rooftop basis functions, the triangular patch basis functions have a better adaptability for arbitrary-shape elements. To meet the requirement of modelling periodic metamaterial structures, the generally formed free-space Green's function is modified to be the periodic Green's function that accounts for the periodicity. The analyses of metamaterials are usually in frequency domain. To derive the responses versus frequency, MoM equations have to be solved once at each frequency point. When the frequency range of interest is wide, or the number of basis functions is large due to complex element geometries, the calculation will cost much time such as several days even weeks. Fortunately, unlike the resonant behaviours and rapid frequency variations of the currents and fields, the impedance matrix elements usually have a regular and smooth variation versus frequency. That enables us to calculate the impedance matrix at only few frequency points and get the impedance matrix at other points of the remaining frequency range of interest using interpolation, which could drastically speed up the computing. This technique can applied to derive the transmission and reflection responses for plane waves as well as the dispersion diagrams for surface waves. Finally, different types of output data in different formats, such as surface current, plane wave response and dispersion diagram, are provided in the post-processing.

2.2 Method of Moments

Electromagnetic problems usually involve linear integral equations. The general form of such linear equation is the operator equation

$$Lf = g \tag{2.1}$$

where L is a linear operator (boundary conditions), g is a known function (excitation), and f is an unknown function. MoM is the most popular approach to solve the problem in (2.1) [1]. By applying MoM, f is expanded in a series of function f_1, f_2, f_3, ... in the domain of L, as

$$f = \sum_{i=1}^{n} a_i f_i \tag{2.2}$$

where a_i are unknown coefficients to be determined, f_i are known expansion functions or basis functions. The expansion in (2.2) has to satisfy the boundary conditions required in (2.1). Substituting (2.2) into (2.1), we have

$$\sum_{i=1}^{n} a_i L f_i = g\,. \tag{2.3}$$

In order to derive the coefficients $\{a_i\}$, we take the inner products of (2.3) with a set of suitable weighting functions w_j, which are usually chosen to be the same as the basis functions f_i (Galerkin's method).

$$\sum_{i=1}^{n} a_i \langle w_j, L f_i \rangle = \langle w_j, g \rangle, \qquad j = 1,2,\cdots,n \quad . \tag{2.4}$$

The equation (2.4) can be written in matrix form as

$$[l_{ji}][a_i] = [g_j] \tag{2.5}$$

where $[l_{ji}] = \begin{bmatrix} \langle w_1, Lf_1 \rangle & \cdots & \langle w_1, Lf_n \rangle \\ \vdots & \ddots & \vdots \\ \langle w_n, Lf_1 \rangle & \cdots & \langle w_n, Lf_n \rangle \end{bmatrix}$, $[a_i] = \begin{bmatrix} a_1 \\ \vdots \\ a_n \end{bmatrix}$, and $[g_j] = \begin{bmatrix} \langle w_1, g \rangle \\ \vdots \\ \langle w_n, g \rangle \end{bmatrix}$.

Thus, the operator equation can now be solved by deriving $\{a_i\}$ using either a direct matrix inversion or an iterative method.

2.3 Integral Equation

A general geometry of double-periodic infinite array used as a metamaterial surface is presented in Fig. 2.1. The figure also shows the wave vector $\vec{k}^i$ of a linearly polarised plane wave incident in an arbitrary direction. θ and φ are the longitude and latitude angles of vector $\vec{k}^i$. The lattice is over the x-y plane with periodicities of D_u and D_v in two arbitrary directions *u* and *v*, skew angle of which is α.

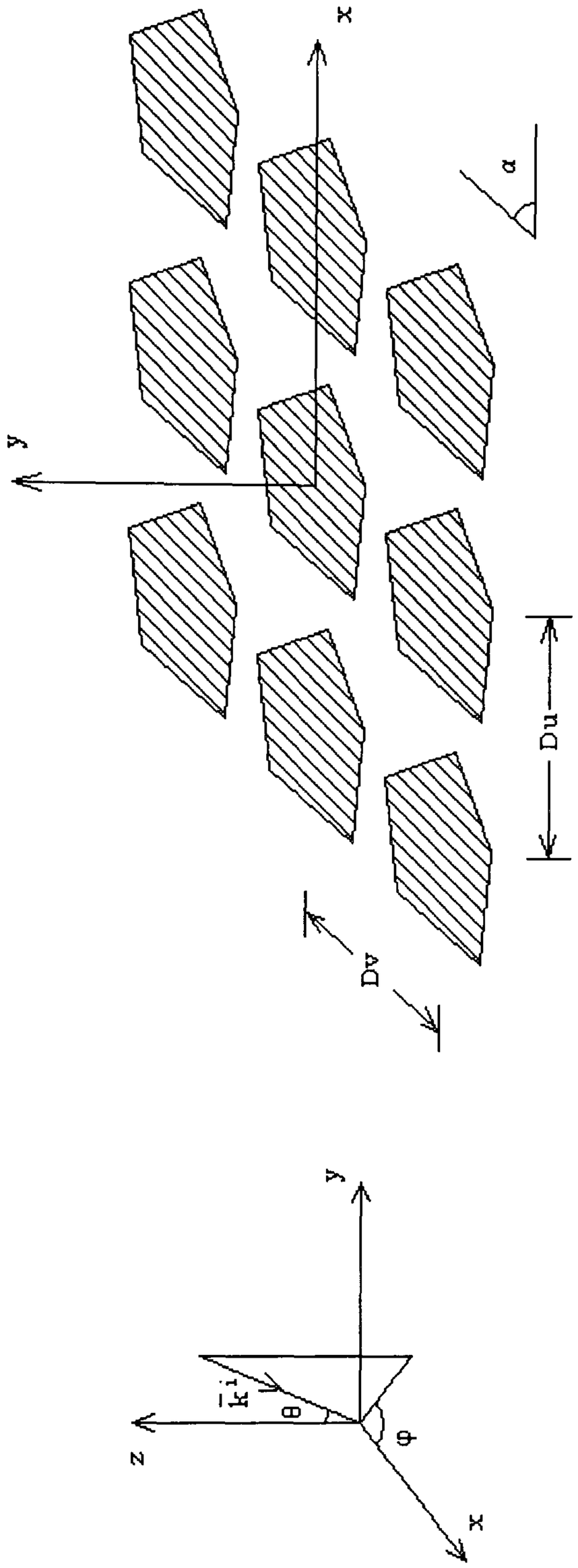

Fig. 2.1 General geometry of 2D metamaterials.

Based on the model in Fig. 2.1, the scattered electric field $\vec{E}^s$ of the array can be expressed with respect to the distribution of the electric surface current $\vec{J}$, using what is known as the electric field integral equation (EFIE)

$$\vec{E}^s = -\int_{S'} \underline{\underline{G}}(\vec{r},\vec{r}')\cdot\vec{J}(\vec{r}')dS' \tag{2.6}$$

where S' is the integral domain of the metal surface, and $\underline{\underline{G}}$ is the well-known dyadic Green's function. In order to avoid the two-dimensional infinite integrals with highly oscillating and slowly decaying integrands that must be evaluated in the EFIE, the mixed potential integral equation (MPIE) [2] is applied in the analysis instead of the EFIE

$$\overrightarrow{E^s}(\vec{r}) = -j\omega\mu\vec{A} - \frac{1}{j\omega\varepsilon}\nabla\left(\nabla\cdot\vec{A}\right) \tag{2.7}$$

where $\vec{A}$ is the magnetic vector potential

$$\vec{A} = \int_{S'} \vec{J}(\vec{r}')G(\vec{r},\vec{r}')dS' \tag{2.8}$$

where G denotes the non-periodic free space Greens function given by

$$G = \frac{\exp\left(-jk|\vec{r}|\right)}{4\pi|\vec{r}|} \tag{2.9}$$

Applying (2.3) into (2.1), the MPIE can take the form of

$$\overrightarrow{E^s}(\vec{r}) = -\int_{S'}\left[j\omega\mu\vec{J}(\vec{r'})G(\vec{r},\vec{r'}) + \frac{\nabla'\cdot\vec{J}(\vec{r'})}{j\omega\varepsilon}\nabla' G(\vec{r},\vec{r'})\right]dS' \tag{2.10}$$

Applying the boundary condition $\hat{n}\times(\vec{E}^i + \vec{E}^s) = 0$ on S', we obtain

$$E^t = -E^s \tag{2.11}$$

According to the MoM, the unknown surface current is expanded as a summation of products of known basis functions and unknown coefficients.

$$\vec{J}(\vec{r'}) = \sum_m I_m \overrightarrow{f_m} \tag{2.12}$$

After the testing procedure, the matrix equation can be derived.

$$\begin{bmatrix} Z_{11} & \cdots & Z_{1M} \\ . & & . \\ . & & . \\ . & & . \\ Z_{M1} & \cdots & Z_{MM} \end{bmatrix} \cdot \begin{bmatrix} I_1 \\ . \\ . \\ . \\ I_M \end{bmatrix} = \begin{bmatrix} V_1 \\ . \\ . \\ . \\ V_M \end{bmatrix} \tag{2.13}$$

The elements are defined as

$$Z_{j,i} = \int\vec{t}_j(\vec{r})\cdot\left(\int j\omega\mu\vec{f}_i(\vec{r'})G(\vec{r},\vec{r'}) + \frac{\nabla'\cdot\vec{f}_i(\vec{r'})\nabla' G(\vec{r},\vec{r'})}{j\omega\varepsilon}dS'\right)dS \tag{2.14}$$

$$V_j = \int\vec{t}_j(\vec{r})\cdot\vec{E}^i(\vec{r})dS \tag{2.15}$$

where $\vec{t}_j(\vec{r})$ is the jth testing function and $\vec{f}_i(\vec{r}')$ is the ith basis function. Now, the unknown coefficients can be obtained using matrix inversion.

$$[I] = [Z]' \cdot [V] \tag{2.16}$$

2.4 Sub-domain Basis Functions

A conventional method to expand the surface current in (2.12) is using entire-domain basis functions. This kind of basis functions applies to the elements with simple regular shapes, such as dipole, tripole, and ring [3], [4]. In modelling of arbitrary-shape geometries, sub-domain basis functions have been found to be more versatile.

2.4.1 Rooftop Basis Function

A well-known type of sub-domain basis functions is the rooftop basis function [5]-[9]. To employ the rooftop basis function, the conductor domain is divided into sub-domains by an $M \times N$ grid (Fig. 2.2, (a)). The summation in (2.12) takes the form of

$$\vec{J}_x = \sum_m \sum_n I_x(m,n)\overrightarrow{f_x}(m,n) \tag{2.17}$$

$$\vec{J}_y = \sum_m \sum_n I_y(m,n)\overrightarrow{f_y}(m,n) \tag{2.18}$$

The basis functions shown in Fig. 2.2, (b) are described as

$$\vec{f}_x(m,n) = \Lambda\left(m+\frac{1}{2}\right)\Pi(n) \tag{2.19}$$

$$\vec{f}_y(m,n) = \Pi(m)\Lambda\left(n+\frac{1}{2}\right) \tag{2.20}$$

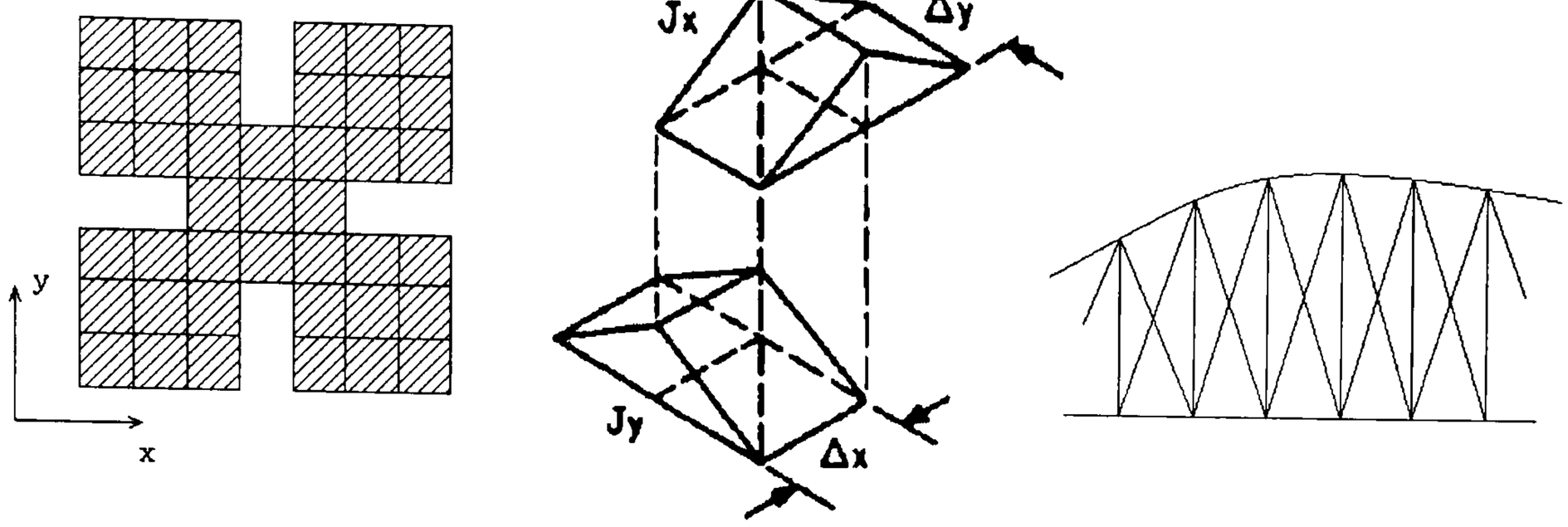

(a) (b) (c)

Fig. 2.2 Representation of surface current using rooftop basis functions.

where

$$\Pi(m) = \begin{cases} 1, & |x - m\Delta x| \le \dfrac{\Delta x}{2} \\ 0, & elsewhere \end{cases} \tag{2.21}$$

$$\Lambda(n) = \begin{cases} 1 - \dfrac{|y - n\Delta y|}{\Delta y}, & |y - n\Delta y| \le \Delta y \\ 0, & elsewhere \end{cases} \tag{2.22}$$

Thus, as is shown in Fig. 2.2, (c), the continuous current functions in both directions can be matched very well by the summations of (2.17) and (2.18).

To make the computing more efficient, rooftop basis function is usually used together with the spectral-form integral equations [6]. Applying the forward and inverse Fourier transforms, EFIE (2.1) is re-written in the spectral domain as

$$\begin{bmatrix} \overrightarrow{E_x^s} \\ \overrightarrow{E_y^s} \end{bmatrix} = -\frac{\eta}{k} F^{-1}\left(\begin{bmatrix} k^2 - k_x^2 & -k_x k_y \\ -k_y k_x & k^2 - k_y^2 \end{bmatrix} \tilde{G}\left(k_x, k_y\right) F\left(\vec{J}(x,y)\right) \right) \tag{2.23}$$

where k is free space wave number, η is modal impedance, F and F^{-1} denote the forward and inverse Fourier transforms respectively,

$$\vec{F}\left(\vec{u}(x,y)\right)=\vec{\tilde{u}}\left(k_x,k_y\right)=\int_{-\infty}^{\infty}\int_{-\infty}^{\infty}\vec{u}(x,y)e^{-j\left(k_x x+k_y y\right)}dxdy \tag{2.24}$$

$$\vec{F}^{-1}\left(\tilde{u}\left(k_x,k_y\right)\right)=\vec{u}(x,y)=\frac{1}{4\pi^2}\int_{-\infty}^{\infty}\int_{-\infty}^{\infty}\vec{\tilde{u}}\left(k_x,k_y\right)e^{+j\left(k_x x+k_y y\right)}dk_x dk_y \tag{2.25}$$

and $\tilde{G}\left(k_x,k_y\right)$ is the spectrum of the Green's function

$$\tilde{G}\left(k_x,k_y\right)=\begin{cases}\dfrac{-j}{2\sqrt{k^2-k_x^2-k_y^2}}, & k^2>k_x^2+k_y^2\\[2ex] \dfrac{1}{2\sqrt{k_x^2+k_y^2-k^2}}, & k^2<k_x^2+k_y^2\end{cases} \tag{2.26}$$

Fourier transforms of the rooftop basis functions are listed below to represent the surface current in spectral domain.

$$\tilde{f}_x(m,n)=\mathrm{sinc}^2\left(\frac{\alpha}{2}\right)\mathrm{sinc}\left(\frac{\beta}{2}\right) \tag{2.27}$$

$$\tilde{f}_y(m,n)=\mathrm{sinc}\left(\frac{\alpha}{2}\right)\mathrm{sinc}^2\left(\frac{\beta}{2}\right) \tag{2.28}$$

where $\alpha = k_{xm}\Delta x$, $\beta = k_{yn}\Delta y$, and $\mathrm{sinc} = \sin(x)/x$.

2.4.2 RWG Basis Function

According to the analysis in section 2.3.1, we can find that the rooftop basis function can be readily applied to elements consisting of rectangular shapes. Other shapes, such as triangle, circle and polygon, seem difficult to be analyzed using rooftop basis function, because rooftop basis function requires the sub domains to be same sized rectangular unit cells placed along x and y directions.

In order to model the more complex elements accurately, another type of basis function, triangular patch basis function, is applied in this paper. Because this kind of basis function has been firstly introduced by Rao, Wilton and Glisson [10], it is also known as RWG basis function. It has been widely applied in recent years [11]-[15]. Unlike the rooftop basis function, there is no requirement of unit size and mesh layout for the RWG basis function, an example of which is shown in Fig. 2.3 (a).

Each RWG basis function is based on each triangle pair. The basis function associated with the *n*th edge is:

$$\vec{f}_n = \begin{cases} \dfrac{l_n}{2A_n^+}\vec{\rho}_n^+, & \vec{r} \in T_n^+ \\ \dfrac{l_n}{2A_n^-}\vec{\rho}_n^-, & \vec{r} \in T_n^- \\ 0, & \textit{elsewhere} \end{cases} \tag{2.29}$$

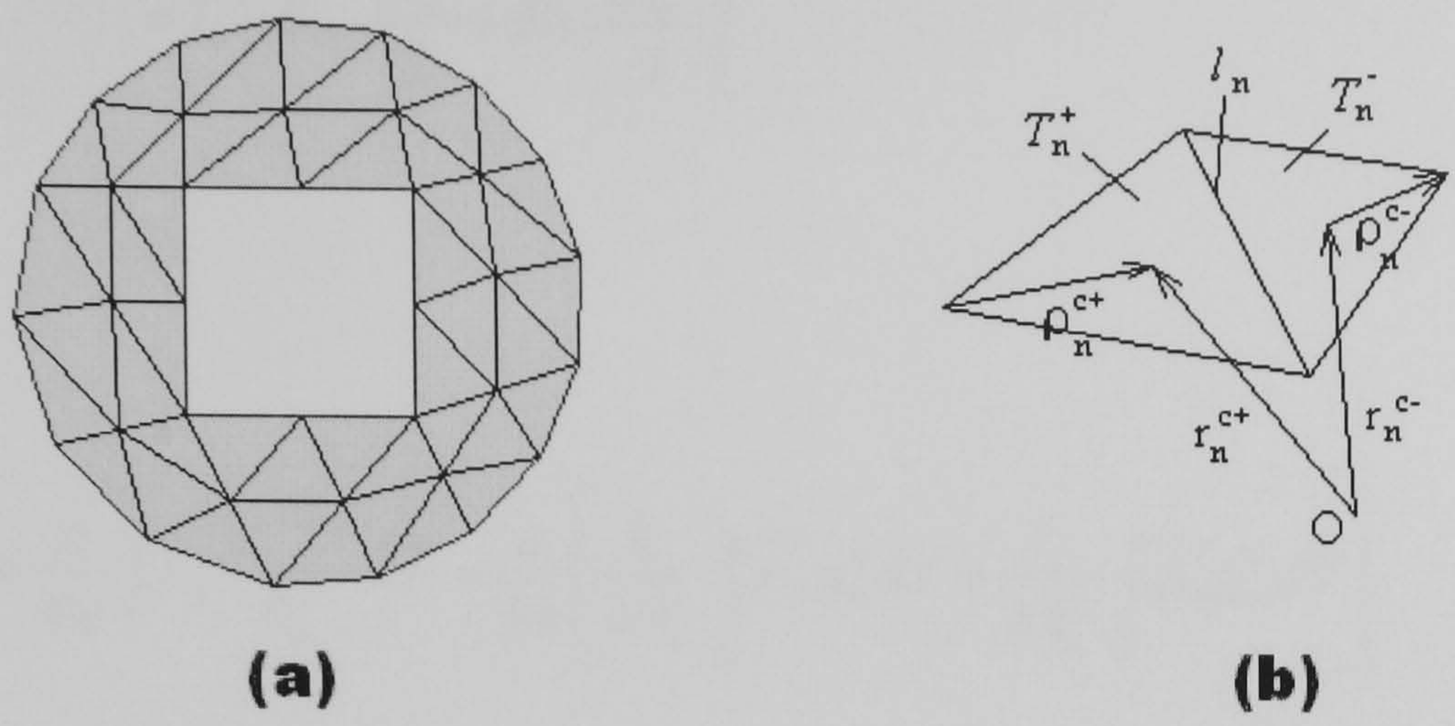

(a) **(b)**

Fig. 2.3 Representation of surface current using RWG basis functions.

where, as shown in Figure 2.3 (b), the centre points of triangles $T_n^{\pm}$ may be designated either by the position vector $\vec{r}_n^{c\pm}$ defined with respect to global coordinate origin O, or by the position vector $\rho_n^{c\pm}$ defined with respect to the free vertex of $T_n^{\pm}$, l_n is the length of the edge and $A_n^{\pm}$ are the areas of triangle $T_n^{\pm}$.

Applying the formula (2.29) into (2.10)-(2.15), we can get the matrix elements of (2.13):

$$Z_{mn} = \int \vec{f}_m \cdot \left(\int j\omega\mu \vec{f}_n G_p + \frac{\nabla' \vec{f}_n \nabla' G_p}{j\omega\varepsilon} dS' \right) dS$$

$$= l_m \left[j\omega \left(\vec{A}_{mn}^{+} \cdot \frac{\vec{\rho}_m^{c+}}{2} + \vec{A}_{mn}^{-} \cdot \frac{\vec{\rho}_m^{c-}}{2} \right) + \Phi_{mn}^{-} - \Phi_{mn}^{+} \right] \tag{2.30}$$

$$V_m = \int \vec{f}_m \cdot \vec{E^i} dS$$

$$= l_m \left(\vec{E}_m^{+} \cdot \frac{\vec{\rho}_m^{c+}}{2} + \vec{E}_m^{-} \cdot \frac{\vec{\rho}_m^{c-}}{2} \right) \tag{2.31}$$

where

$$\vec{A}_{mn}^{\pm} = \frac{\mu}{4\pi} \int \vec{f}_n \frac{e^{-jkR_m^{\pm}}}{R_m^{\pm}} dS' = \frac{\mu}{4\pi} \left[\frac{l_n}{2A_n^{+}} \int_{T_n^{+}} \vec{\rho}_n^{+} g_m^{\pm} dS' + \frac{l_n}{2A_n^{-}} \int_{T_n^{-}} \vec{\rho}_n^{-} g_m^{\pm} dS' \right] \tag{2.32}$$

$$\Phi_{mn}^{\pm} = -\frac{1}{4\pi j\omega\varepsilon} \int \nabla' \vec{f}_n \frac{e^{-jkR_m^{\pm}}}{R_m^{\pm}} dS' = -\frac{1}{4\pi j\omega\varepsilon} \left[\frac{l_n}{A_n^{+}} \int_{T_n^{+}} g_m^{\pm} dS' + \frac{l_n}{A_n^{-}} \int_{T_n^{-}} g_m^{\pm} dS' \right] \tag{2.33}$$

$$R_m^{\pm} = \left| \vec{r}_m^{c\pm} - \vec{r}' \right| \tag{2.34}$$

$$g_m^{\pm} = \frac{e^{-jk\left|\vec{r}_m^{c\pm} - \vec{r}'\right|}}{\left|\vec{r}_m^{c\pm} - \vec{r}'\right|} \tag{2.35}$$

$$\vec{E}_m^{\pm} = \overrightarrow{E^i}(\vec{r}_m^{c\pm}) \tag{2.36}$$

To numerically compute the integral of function g over a triangle in (2.32) and (2.33), a so-called barycentric subdivision method is employed [16], [17]. As is shown in figure 2.4, a primary triangle is divided into nine equal small sub-triangles by use of the 1/3 rule. The integral of function g is approximated by the average of mid-point values of the nine sub-triangles instead of the originally centric value of the primary triangle in [16]. The numerical formula is given in (2.37).

$$\int_{T_m} g(\vec{r}) dS = \frac{A_m}{9} \sum_{k=1}^{9} g(\vec{r}_k^{c}) \tag{2.37}$$

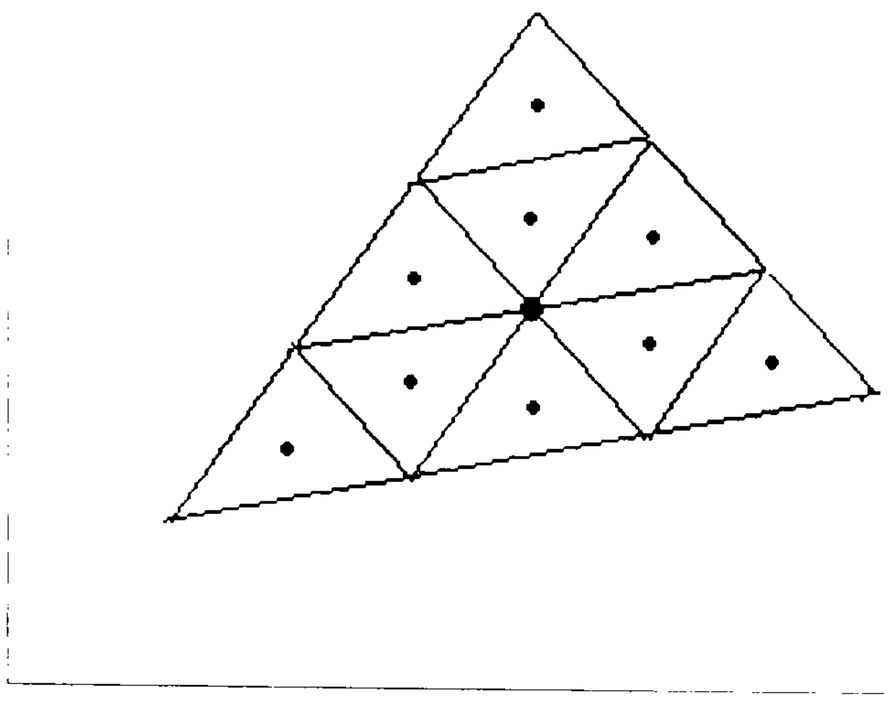

Fig. 2.4 Subdivision of the primary triangle.

2.5 Periodic Green's Function

Green's function is known in electromagnetism as the relation of the charge density and the potential of the scattered electromagnetic field. The free-space Green's function is shown in (2.7). This function applies in the scattering problem of perfect conductors in three-dimensional free space. Considering the scattering problem of metamaterials, Green's function has to be modified to be in the periodic form [18], [19] because of the periodicity of the structure.

Grating lobes appear in the scattering of metamaterials because of the periodic layout. Side lobes, which are equal in amplitude to the main lobe, are repeated along the directions of the periodicity [20]. According to the Floquet theorem [21], [22], if the incident plane wave propagates in the direction $\hat{k}$, the amplitude of all element currents of the array will be the same. Having the model in Fig. 2.1 as an x- and y-directional array, the element current in column p and row q is

$$I_{m,n} = I_{0,0} e^{-jk\left(pD_x x + qD_y y\right)} \tag{2.38}$$

Thus, the surface current $J(x,y)$ can be expressed with Floquet modes as

$$J(x,y) = \sum_{p=-\infty}^{\infty} \sum_{q=-\infty}^{\infty} c_{p,q} f_{p,q}(x,y)$$

where $c_{p,q}$ is the coefficient, $f_{p,q}(x,y)$ is the Floquet mode:

$$f_{p,q}(x,y) = e^{-jk_x^{p,q}(x-x')} e^{-jk_y^{p,q}(y-y')}$$

$$k_x^{p,q} = \frac{2\pi p}{D_x} + k\sin\theta\cos\phi,\ k_x^{p,q} = \frac{2\pi p}{D_x} + k\sin\theta\sin\phi.$$

The free-space Green's function in (2.9) can then be re-written as the periodic Green's function

$$G_P = \sum_{p=-\infty}^{\infty} \sum_{q=-\infty}^{\infty} \frac{e^{-jk_x^{p,q}(x-x')} e^{-jk_y^{p,q}(y-y')} e^{-jk_z^{p,q}(z-z')}}{2jk_z^{p,q} D_x D_y} \tag{2.39}$$

where

$$k_z^{p,q} = \begin{cases} \sqrt{k^2 - \left(\left(k_x^{p,q}\right)^2 + \left(k_y^{p,q}\right)^2\right)}, & k^2 > \left(\left(k_x^{p,q}\right)^2 + \left(k_y^{p,q}\right)^2\right) \\ -j\sqrt{\left(\left(k_x^{p,q}\right)^2 + \left(k_y^{p,q}\right)^2\right) - k^2}, & k^2 \le \left(\left(k_x^{p,q}\right)^2 + \left(k_y^{p,q}\right)^2\right) \end{cases}.$$

The periodic Green's function in (2.39) is expressed as a summation of Floquet modes. Since the p and q are infinite series, it is not numerical in real problems. A finite truncation must be applied to approximate the summations. Choosing proper orders of the series to truncate is important for solving the MPIE. If too many orders are chosen, it will waste too much of the computing time. On the other hand, the results will loose accuracy if the orders are not enough. For that purpose, the decaying property of the coupling between two basis functions is studied.

The coupling between basis functions is studied to decide how many terms of Floquet modes in (2.39) need to be chosen to meet the accuracy requirement. Generally speaking, the numbers of terms to represent the Green's function depends on the size of the basis functions. In other words, when increasing the number of the basis functions for a fixed-size element, the coupling between two basis functions will decay more slowly. A fixed-length dipole array is considered here as an example. The variations of the coupling between two basis functions for different number of basis functions along the dipole are shown in Fig. 2.5. From the figure, we can find that the coupling is decaying more and more slowly with increasing number of the basis functions. Nevertheless, the variation is kept similar when the number of the basis functions is large enough (greater than 15). Thus, when analyzing periodic structures with complex elements (consisting of large number of basis functions), Floquet terms

of 81 by 81 (-40 to 40 for each direction) are enough for required error less than 2%, and Floquet terms of 161 by 161 for required error less than 1%. For other element geometries, similar convergence analysis can be made to meet the requirement of the accuracy.

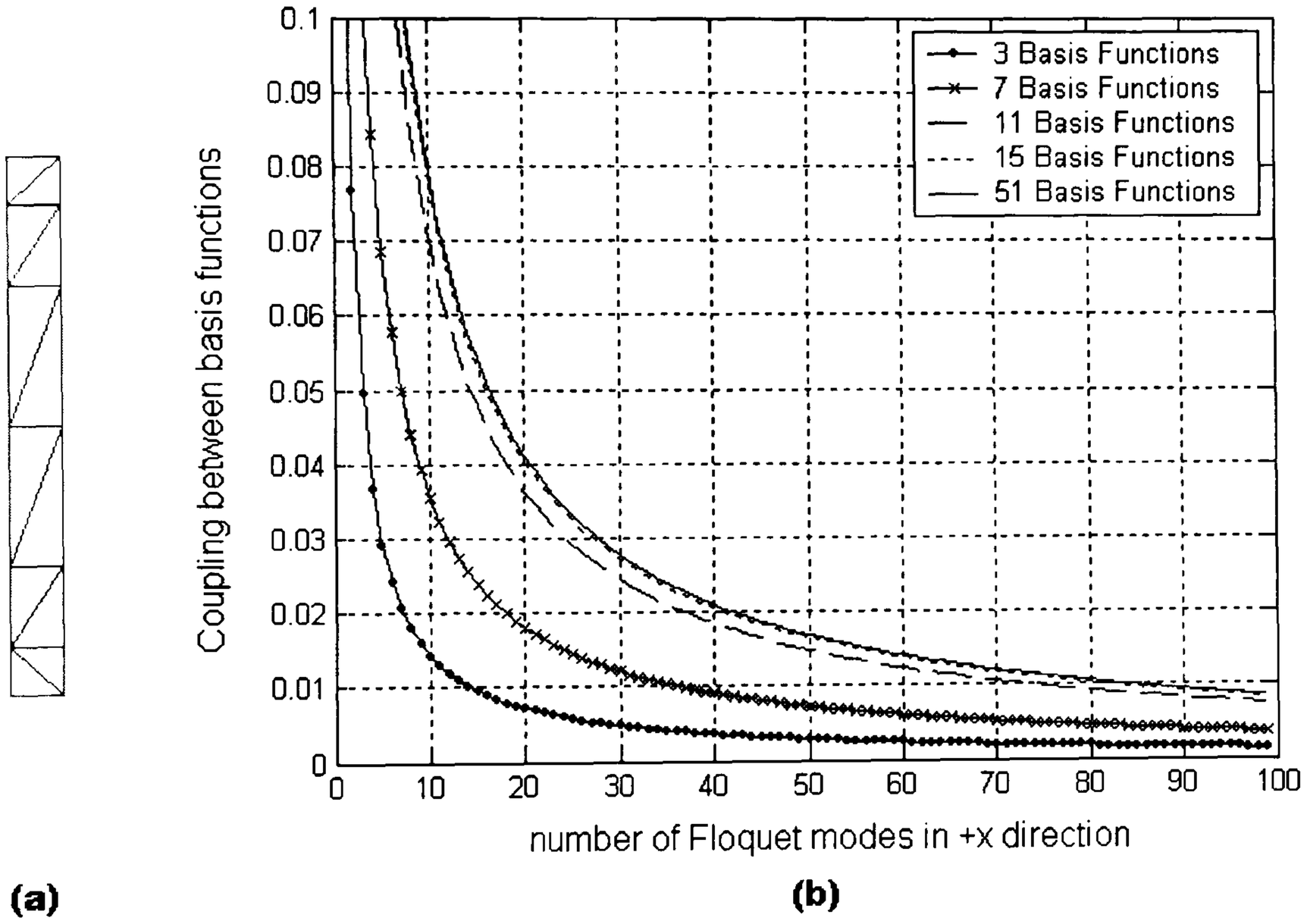

Fig. 2.5 Coupling between basis functions with different number of Floquet modes.

2.6 Impedance Matrix Interpolation

Since the surface currents and the scattered fields show irregular variations versus the frequency because of the resonant behaviours, a great amount of time has to be spent to calculate these quantities at every frequency of interest in order to analyze a metamaterial surface. However, unlike the resonant behaviours and rapid frequency variations of the currents and fields, the impedance matrix elements usually have regular and smooth variations versus frequency. That enables us to calculate the impedance matrix at only few frequency points and get the impedance matrix at other points of the remaining frequency range of interest using interpolation.

The typical frequency variation of the impedance matrix elements of an EBG array is shown in Fig 2.6. Here we used the dipole geometry in Fig. 2.5 as an example. Because the elements in metamaterials act approximately as half wavelength resonators, we chose the functions [23]

$$R(f) = A^R f^2 + B^R f + C^R \tag{2.50}$$

$$I(f) = A^I / f + B^I f + C^I \tag{2.51}$$

as the interpolation functions for the impedance matrix elements, where $R(f)$ and $I(f)$ are real part and imaginary part of the impedance matrix elements respectively $\left(Z_{ji}(f) = R_{ji}(f) + j \cdot I_{ji}(f)\right)$. After calculating the impedance matrices at three frequency points, the interpolation coefficients are derived by solving (2.50) and (2.51):

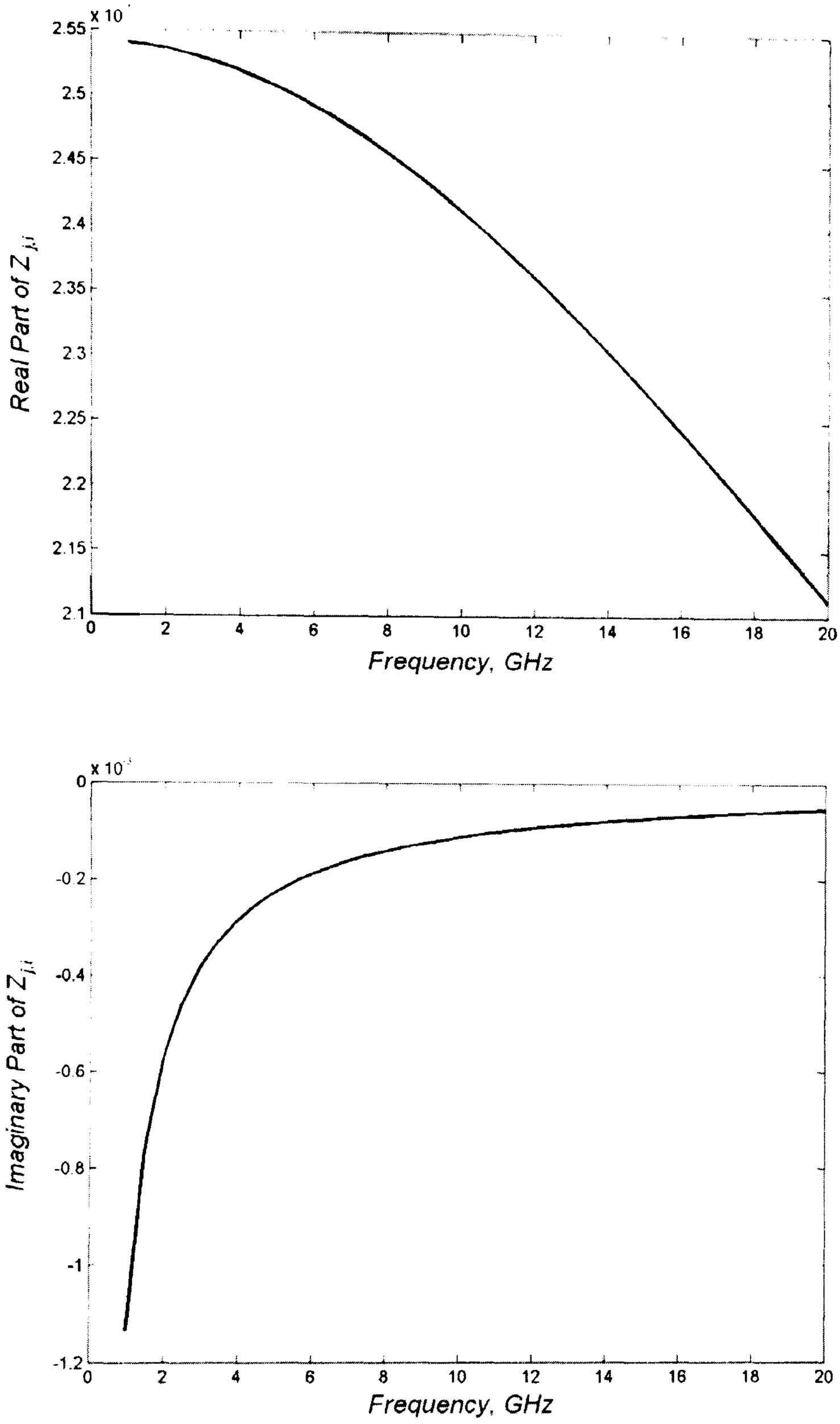

Fig. 2.6 Variation of the impedance matrix elements versus frequency.

$$A_{ji}^{R} = \frac{(\mathrm{Re}[Z_{ji}(f_1)](f_2 - f_3) + \mathrm{Re}[Z_{ji}(f_2)](f_3 - f_1) + \mathrm{Re}[Z_{ji}(f_3)](f_1 - f_2))}{f_1^2(f_2 - f_3) + f_2^2(f_3 - f_1) + f_3^2(f_1 - f_2)} \tag{2.52}$$

$$B_{ji}^{R} = \frac{\mathrm{Re}[Z_{ji}(f_1)] - \mathrm{Re}[Z_{ji}(f_2)] - A_{ji}^{R}(f_1^2 - f_2^2)}{f_1 - f_2} \tag{2.53}$$

$$C_{ji}^{R} = \mathrm{Re}[Z_{ji}(f_1)] - A_{ji}^{R} f_1^2 - B_{ji}^{R} f_1 \tag{2.54}$$

$$A_{ji}^{I} = \frac{f_1 f_2 f_3(\mathrm{Im}[Z_{ji}(f_1)](f_2 - f_3) + \mathrm{Im}[Z_{ji}(f_2)](f_3 - f_1) + \mathrm{Im}[Z_{ji}(f_3)](f_1 - f_2))}{f_1^2(f_2 - f_3) + f_2^2(f_3 - f_1) + f_3^2(f_1 - f_2)} \tag{2.55}$$

$$B_{ji}^{I} = \frac{\mathrm{Im}[Z_{ji}(f_1)] - \mathrm{Im}[Z_{ji}(f_2)] - A_{ji}^{I}(1/f_1 - 1/f_2)}{f_1 - f_2} \tag{2.56}$$

$$C_{ji}^{I} = \mathrm{Im}[Z_{ji}(f_1)] - A_{ji}^{I}/f_1 - B_{ji}^{I} f_1 \tag{2.57}$$

With (2.50) – (2.57), the impedance matrices at every frequency, which are used to calculate the surface currents and scattered fields, can be derived by using the interpolation with (2.50) and (2.51).

2.7 Solving of Homogeneous MoM Equation

In the analysis of EBG and LHM structures, it is required to determine the band gap properties of the structure on the two-dimensional plane of periodicity. Thus it is essential to explore all possible propagation modes that may exist for all possible directions along the two-dimensional plane of the array. The dispersion characteristics of the array for its two-dimensional plane of periodicity can be calculated by solving the homogeneous version of MoM equation (2.13) [1]

$$\begin{bmatrix} Z_{11} & \cdots & Z_{1M} \\ \cdot & & \cdot \\ \cdot & & \cdot \\ \cdot & & \cdot \\ Z_{M1} & \cdots & Z_{MM} \end{bmatrix} \cdot \begin{bmatrix} I_1 \\ \cdot \\ \cdot \\ \cdot \\ I_M \end{bmatrix} = \begin{bmatrix} 0 \\ \cdot \\ \cdot \\ \cdot \\ 0 \end{bmatrix} \tag{2.58}$$

For the analysis of the surface-wave propagation in the x-y plane, the angle θ in Fig. 2.1 is 90 degrees, and the propagation constant β is set to be

$$\beta_x = k_{x0}, \quad \beta_y = k_{y0} \tag{2.59}$$

for lossless cases. The excitation matrix V in (2.13) is set to zero and the values of frequency, f, and propagation constants β_x and β_y that satisfy the equation are identified. For the set of homogeneous linear equations expressed in (2.59) to have non-trivial solutions, the determinant of the impedance matrix Z must be zero. The pairs of f and β values (real) for which the determinant becomes zero correspond to propagating modes. By varying β from zero to the boundary of the irreducible Brillouin zone a number of frequency sweeps are carried out. All the corresponding

determinants of Z are calculated and plotted versus frequency for different values of β. From the determinant plot at 2.5GHz of a tripole array, of which element arms are 5mm long and 0.2mm wide and the periodicity is 10mm , zeros are identified as sharp minima as what Fig. 2.7 shows [24]. Complex values of β that describe leaky modes are not considered in this thesis.

The method mentioned above is the conventional way to generate the dispersion diagram. To make it faster and more efficient, a new method is given out in this thesis. With this new method, the scanning of the propagation constant range is replaced by that of the frequency range, and the impedance interpolation technique can be applied to accelerate the calculation. Details of this method will be introduced in Chapter 3.

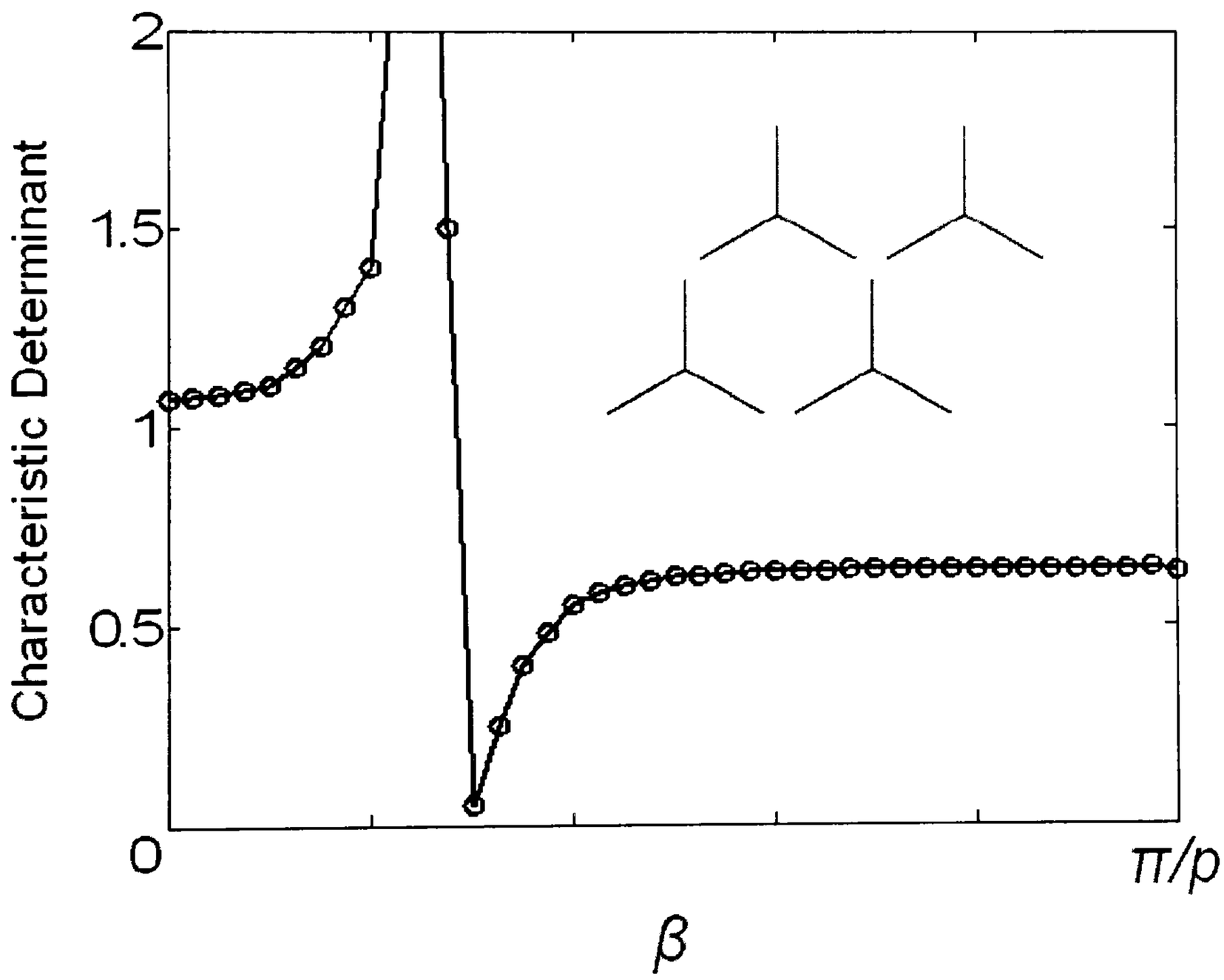

Fig. 2.7 Characteristic determinant versus frequency; mode is identified as a sharp minimum.

2.8 Visualisation of the Results

According to the approaches in the sections above, a systematic procedure to analyze metamaterials has been set up. In order to make a good electromagnetic analysis of the metamaterials, visualisation of the output data is very important. In the post-processing procedure, visualisations of various types of results, such as the surface current, the plane-wave response and the dispersion diagram, are given out in the following for the designs of different kinds of metamaterials.

2.8.1 Surface Current

Current visualization adds tremendous value as a design troubleshooting aid, and is a source of valuable insight into the structure behaviour. Once the MoM equations are solved, the surface current density within each RWG triangle can be derived by applying equation (2.12). An example of the surface current distribution on the element of a square-loop array is given out in Fig. 2.8. In order to apply the RWG basis functions, the element is decomposed by a triangular mesh. A normal-incident plane wave is applied as what is shown in Fig. 2.8. Since each RWG basis function is related to the common edge of a triangle pair, the surface current within the triangle can be expressed as the summation of the currents flowing through the edges, which are shared with its neighbours. Considering of a triangle T_n, which have the common edges, l_a, l_b and l_c, with its three adjacent triangles, once the solution of the unknown coefficients in (2.16) are obtained, the surface current density over T_n is derived as

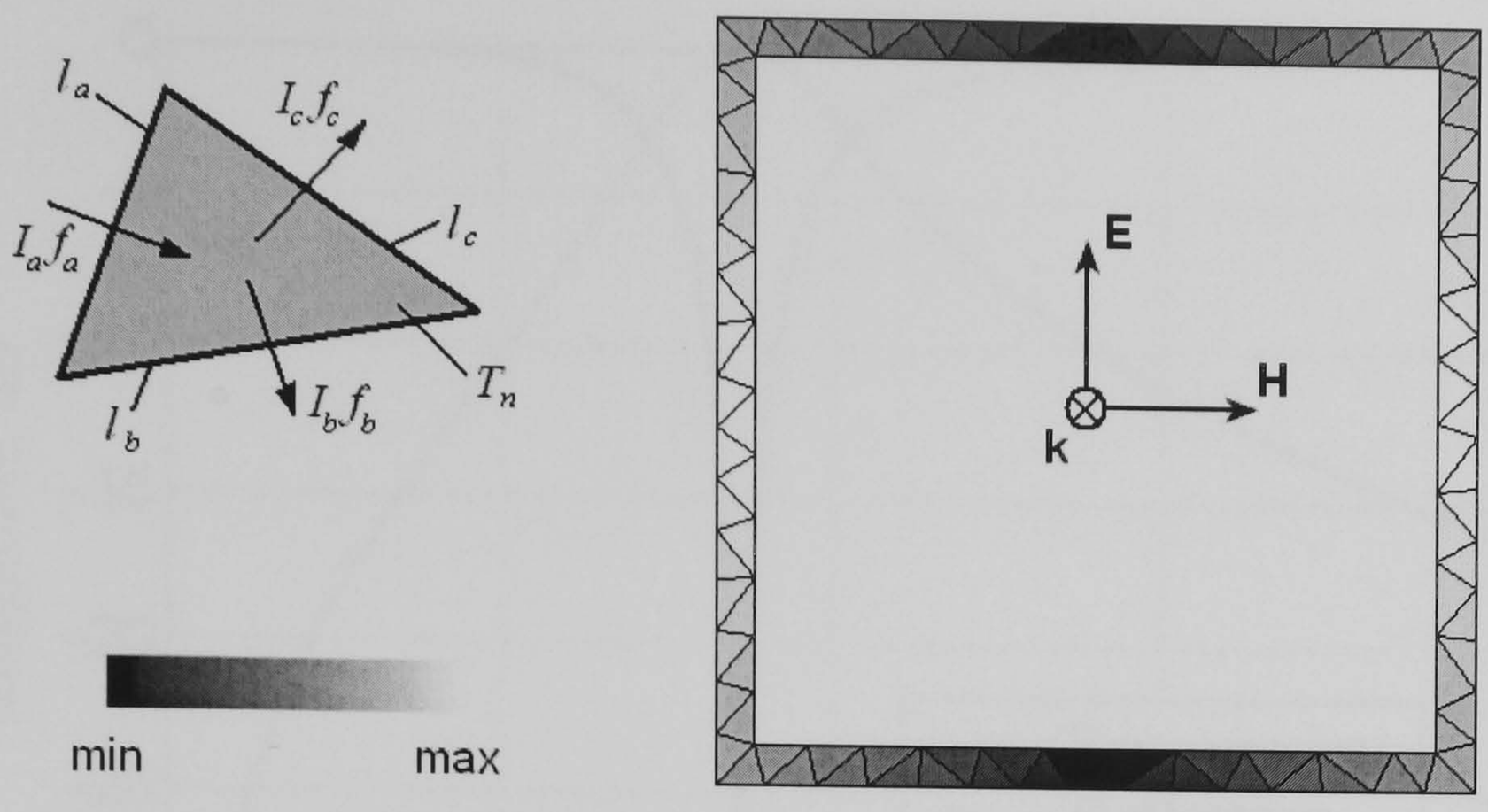

Fig. 2.8 Surface current distribution on the element of a square-loop array.

$$\vec{J}_n = I_a \vec{f}_a + I_b \vec{f}_b + I_c \vec{f}_c \tag{2.60}$$

After all the surface current densities in triangles are calculated, colours in greyscale fill in the triangular mesh in representation of the normalised magnitudes of the surface current densities.

2.8.2 Plane-Wave Response

Transmission and reflection coefficients are the most typical parameters of the plane-wave response, which are widely used in the analysis of metamaterials. The transmission (reflection) coefficient is defined as the ratio of the transmitted (reflected) field strength to the incident field strength of an electromagnetic wave when it is incident upon an interface surface between media with two different refractive indices. For metamaterials, the interface surface is the plane where the metal elements lie on.

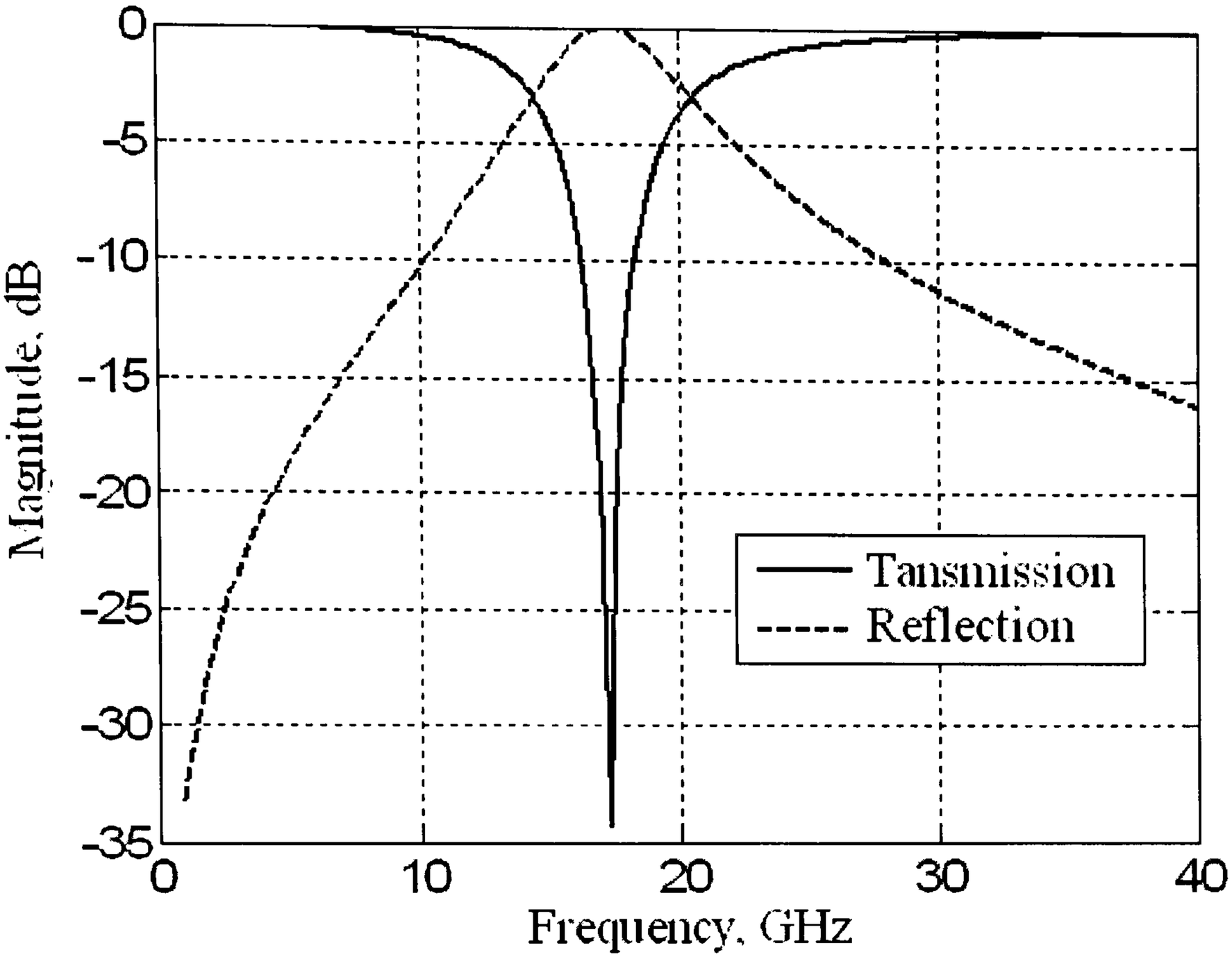

Fig. 2.9 Typical magnitudes of the transmission and reflection coefficients of an FSS array.

Fig. 2.9 shows the magnitudes of the transmission and reflection coefficients of a frequency selective surface (FSS) array in response to plane-wave incidence. The resonant frequency is approximately at 17 GHz, where the total reflection of the incident wave can be observed from the reflection coefficient curve. A transmission band-gap near the resonant frequency can also be found from the transmission coefficient curve.

In order to characterise the Artificial Magnetic Conductor (AMC) surfaces, the phase of the reflection coefficients are usually plotted as in Fig. 2.10. Because of the high-impedance feature of the AMC surfaces, the phase at the resonant frequency (8.5 GHz in Fig. 2.10) is equal to 0. The working frequency range is normally taken as at the range where the phase is within -90 to 90 degrees.

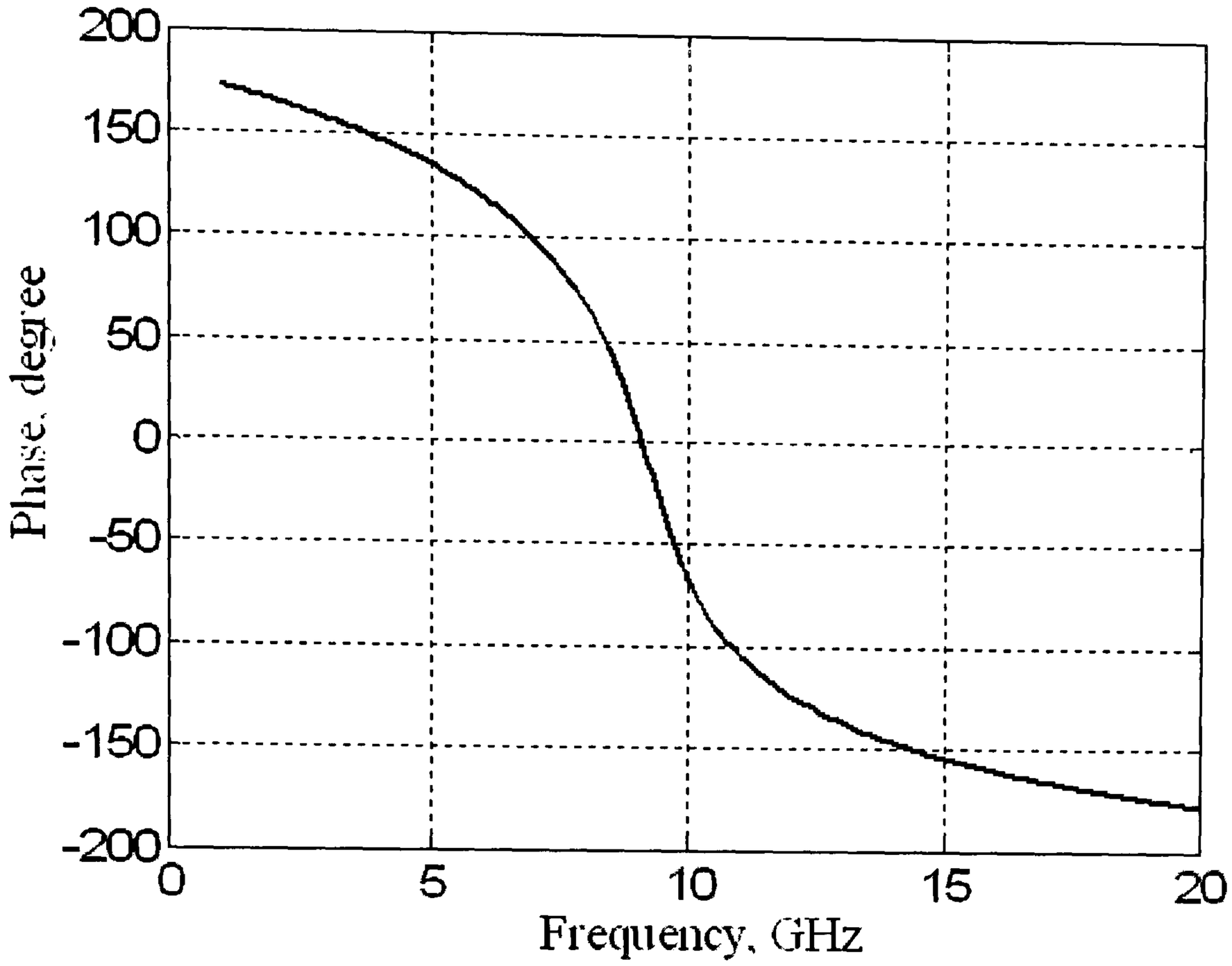

Fig. 2.10 Typical phase of the reflection coefficients of an AMC surface.

2.8.3 Dispersion Diagram

The dispersion diagram of an EBG array on a triangular lattice with skewed angle of 60 degrees is shown in Fig. 2.11. By exploring the whole two-dimensional irreducible Brillouin zone, all the possible modes that exist on the x-y plane could be found [25]. The bold lines in the dispersion diagram indicate the propagation modes (i.e. the modes that are supported by the structure). For the range of frequencies where there is an absence of any propagation mode, that range of frequencies is considered as a band gap.

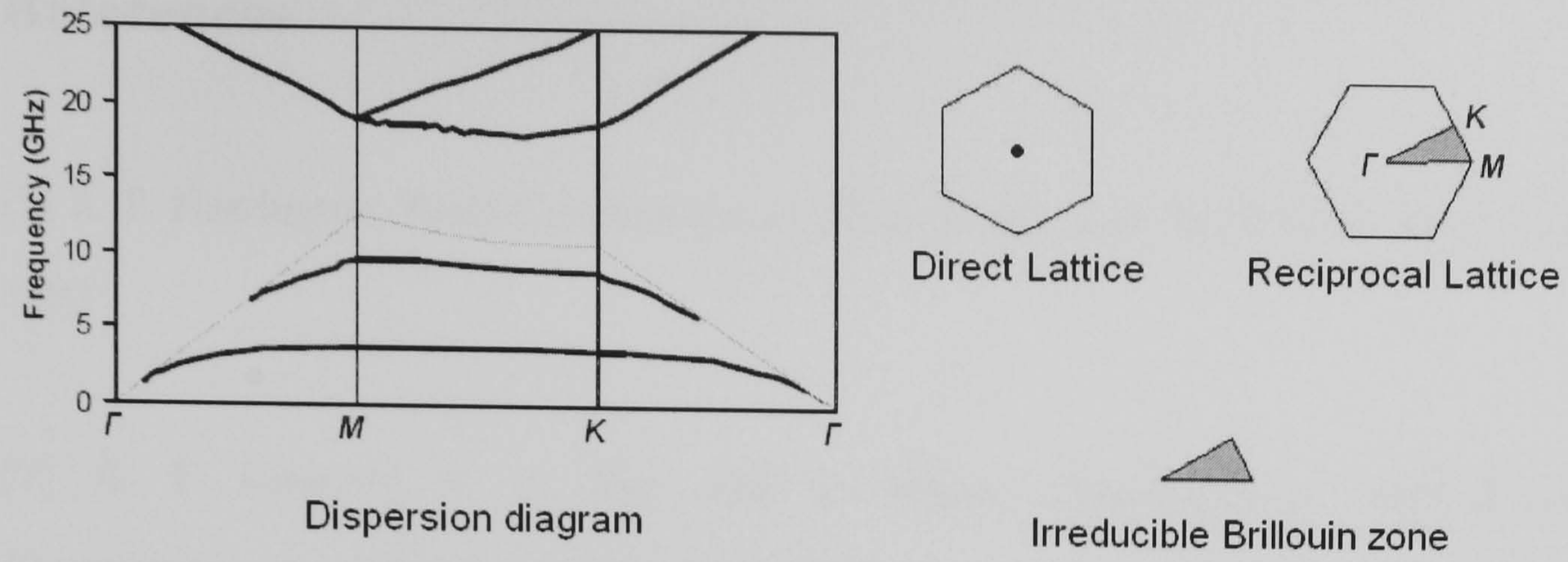

Fig. 2.11 Typical dispersion diagram, direct lattice, reciprocal lattice and irreducible Brillouin zone.

2.9 Conclusions

Efficient modelling techniques for producing the plane wave response and the dispersion diagram of metamaterials have been presented in this chapter. The method is based on solving the mixed potential integral equation using method of moments. RWG basis function is applied in modelling of the arbitrary-shaped array elements. Periodic Green's function is used for the periodic features of metamaterials. An impedance matrix interpolation technique is applied in order to significantly accelerate the computations, especially when a large number of basis functions are required due to the complex geometry of the array elements. Finally the visualisation of the results using surface currents, transmission/reflection coefficients and dispersion diagrams is described.

References

[1] R. F. Harrington, *Field Computation by Moment Methods*, IEEE Press, New York, 1993

[2] A. F. Peterson, S. L. Ray, and R. Mittra, *Computational Methods for Electromagnetics*, IEEE Press, New York, 1998

[3] R. Mittra, C. H. Chan, and T. Cwik, "Techniques for Analyzing Frequency Selective Surfaces – A Review", *Proc. IEEE*, Vol. 76, no. 12, pp. 1593-1614, 1988

[4] J. C. Vardaxoglou, *Frequency Selective Surfaces: Analysis and Design*, Research Studies Press Ltd., Taunton, 1997

[5] A. W. Glisson and D. R. Wilton, "Simple and Efficient Numerical Methods for Problems of Electromagnetic Radiation and Scattering from Surfaces", *IEEE Trans. Antennas Propagat.*, Vol. 28, no. 5, pp. 593-603, 1980

[6] C. H. Chan and R. Mittra, "On the Analysis of Frequency-Selective Surfaces Using Sub-domain Basis Functions", *IEEE Trans. Antennas Propagat.*, Vol. 38, no. 1, pp. 40-50, 1990

[7] T. Wriedt, K. H. Wolff, F. Arndt, and U. Tucholke, "Rigorous Hybrid Field Theoretic Design of Stepped Rectangular Waveguide Mode Converters Including the Horn Transitions into Half-Space", *IEEE Trans. Antennas Propagat.*, Vol. 37, no. 6, pp. 780-790, 1989

[8] B. J. Rubin, and S. Daijavad, "Radiation and Scattering from Structures Involving Finite-Size Dielectric Regions", *IEEE Trans. Antennas Propagat.*, Vol. 38, no. 11, pp. 1863-1873, 1990

[9] H. Y. Yao, W. Xu, L. W. Li, Q. Wu, and T. S. Yeo, "Propagation Property Analysis of Metamaterial Constructed by Conductive SRRs and Wires Using the MGS-Based Algorithm", *IEEE Trans. Microwave Theory Tech.*, Vol. 53, no. 4, pp. 1469-1476, 2005

[10] S. M. Rao, D. R. Wilton, and A. W. Glisson, "Electromagnetic Scattering by Surfaces of Arbitrary Shape", *IEEE Trans. Antennas Propagat.*, Vol. 30, no. 3, pp. 409-418, 1982

[11] J. F. Lee, R. Lee, and R. J. Burkholder, "Loop Star Basis Functions and a Robust Preconditioner for EFIE Scattering Problems", *IEEE Trans. Antennas Propagat.*, Vol. 51, no. 8, pp. 409-418, 2003

[12] H. Chen, L. Tsang, and C. Huang, "Effects of Gaps and Bypass Capacitors on Interconnect of PCB with Multilayered Geometry", IEE Proceedings - Microwaves, Antennas and Propagation, Vol. 148, no. 3, pp. 167-173, 2001

[13] L. Zhang, N. Yuan, M. Zhang, L. W. Li, ans Y. B. Gan, "RCS Computation for a Large Array of Waveguide Slots with Finite Wall Thickness Using the MoM Accelerated by P-FFT Algorithm", *IEEE Trans. Antennas Propagat.*, Vol. 53, no. 9, pp. 3101-3105, 2005

[14] W. Cai, T. Yu, H. Wang, Y. Yu, "High-Order Mixed RWG Basis Functions for Electromagnetic Applications", *IEEE Trans. Microwave Theory Tech.*, Vol. 49, no. 7,

pp. 1295-1303, 2001

[15] Y. Zhang; T. J. Cui, W. C. Chew, and J. S. Zhao, "Magnetic Field Integral Equation at Very Low Frequencies", *IEEE Trans. Antennas Propagat.*, Vol. 51, no. 8, pp. 1864-1871, 2003

[16] Y. Kamen and L. Shirman, "Triangle Rendering Using Adaptive Subdivision", *IEEE Computer Graphic and Applications*, Vol. 18, no. 2, pp. 95-103, 1998

[17] S. Makarov, "MoM Antenna Simulations with Matlab: RWG Basis Functions", *IEEE Antennas and Propagation Magazine*, Vol. 43, no. 5, pp. 100-107, 2001

[18] R. E. Jorgenson and R. Mittra, "Efficient Calculation of the Free-Space Periodic Green's Function", *IEEE Trans. Antennas Propagat.*, Vol. 38, no. 5, pp. 633-642, 1990

[19] S. Singh and R. Singh, "Efficient Computation of the Free-Space Periodic Green's Function", *IEEE Trans. Antennas Propagat.*, Vol. 39, no. 7, pp. 1226-1229, 1991

[20] J. D. Kraus and R. J. Marhefka, *Antennas: For All Applications, Third Edition*, McGraw-Hill, New York, 2002

[21] N. Amitay, V. Galindo, and C. P. Wu, *Theory and Analysis of Phased Array Antennas*, John Wiley & Sons, Inc., New York, 1972

[22] B. A. Munk, *Frequency Selective Surfaces: Theory and Design*, John Wiley & Sons, Inc., New York, 2000

[23] J. Yeo and R. Mittra, "An Algorithm for Interpolating the Frequency Variations of Method-of-Moments Matrices Arising in the Analysis of Planar Microstrip Structures", *IEEE Trans. Microwave Theory Tech.*, Vol. 51, no. 3, pp. 1018-1025, 2003

[24] R. Y. L. Lee, *Design and Modelling of Photonic Band-Gap Response from Doubly Periodic Arrays*, Ph.D. Thesis of Loughborough University, Loughborough, United Kingdom, 1999

[25] J. D. Joannopoulos, R. D. Meade, and J. N. Winn, *Photonic Crystals: Molding the Flow of Light*, Princeton University Press, Princeton, 1995

3. Analysis and Design of EBG and AMC Surfaces

3.1 Introduction

Using the efficient modelling technique presented in chapter 2, electromagnetic band-gap (EBG) structures and artificial magnetic conductor (AMC) surfaces are analysed and designed in this chapter. In recent years, the EBG property of metallic arrays, whereby the surface waves are suppressed by the emergence of the band gap has been studied [1]-[10]. Metallic arrays printed on grounded dielectric substrates have also been presented as AMC surfaces that exhibit zero-phase-shift reflections of incident plane waves [11]-[14]. Because of the requirement for small microwave components in integrated designs and the trend of multiple frequency bands in modern wireless communication systems, miniaturised and multiband metamaterials have drawn the attention of recent research effort. EBG and AMC surfaces based on

tripole arrays are presented in the following sections and novel designs are studied that achieve miniaturisation and multiband performance. In the analysis, large impedance matrices are built in order to derive accurate results for these complex element geometries. Impedance matrix interpolation is used to accelerate the computations that produce the plane-wave responses as well as the dispersion diagrams that characterise surface-wave propagation along the arrays. The accuracy of the results for different interpolation step values are compared and discussed.

3.2 Fractal EBG and AMC Surfaces

There are two different methods to achieve miniaturisation of EBG and AMC surfaces. As was mentioned in chapter 1, the elements of the metamaterial arrays act approximately as half-wavelength resonators for the incident electromagnetic waves. The first method is achieving more electrical length packed in fixed available space of the unit cell in order to miniaturise the resonant elements. Alternatively, miniaturisation can also be achieved by close coupling of two or more arrays in a multi-layer configuration [15]. Compared with the first method, closely coupled structures could give a better miniaturisation ratio. Details of the closely coupled structures are not discussed in this thesis.

Fractal EBG arrays are studied here to with the aim to miniaturise the unit cell and to produce multiband responses. Several fractal geometries may exist. Here we study the fractal EBG array shown in Fig. 3.1. It is comprised of tripole-based fractal elements that emerge after multiple-order loading of single tripole elements [16]. The lengths of the main arms and the branches are 5mm, 2.5mm, 1.25mm and 0.625mm respectively. The width of all the arms is 0.1mm. The elements are placed on a hexagonal lattice with periodicity 10mm.

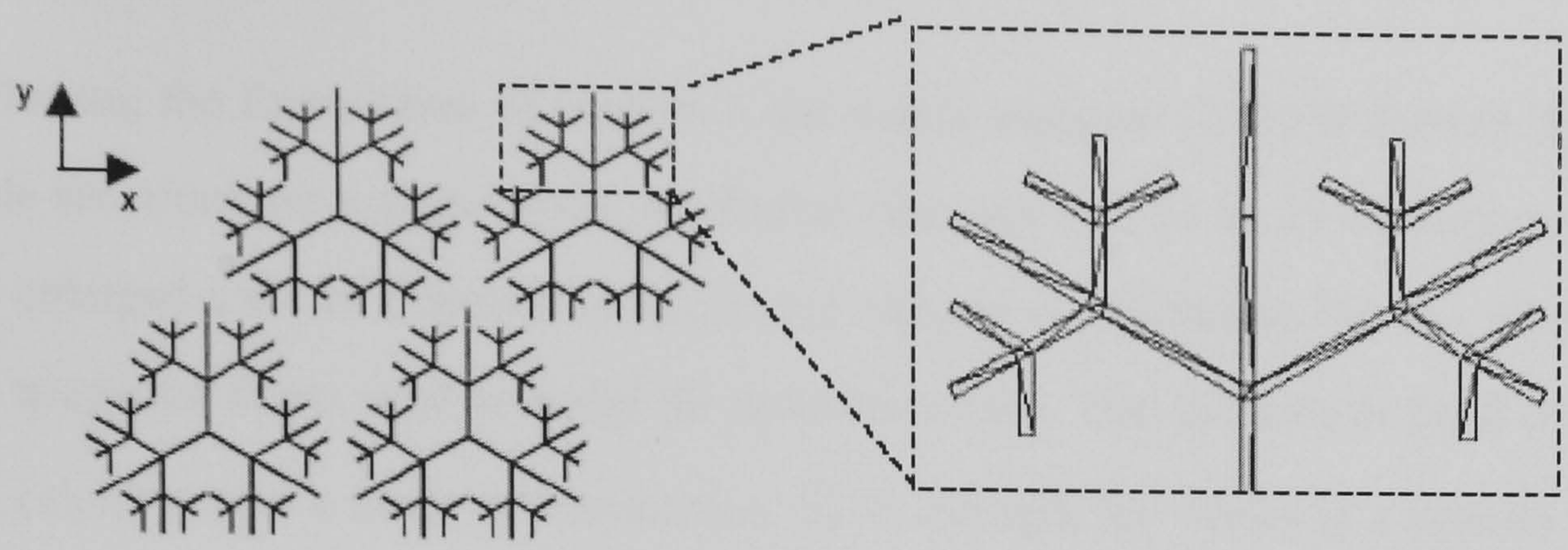

Fig. 3.1 Section of fractal EBG array and enlarged view of a section of the fractal element with basis functions.

3.3 Ungrounded Fractal EBG Surfaces

To study the characteristics of the fractal metamaterials, ungrounded fractal EBG surfaces are first analysed. These surfaces are tripole based arrays over a dielectric substrate with $\varepsilon_r = 2.2$ and thickness 1.13 mm as is shown in Fig. 3.2.

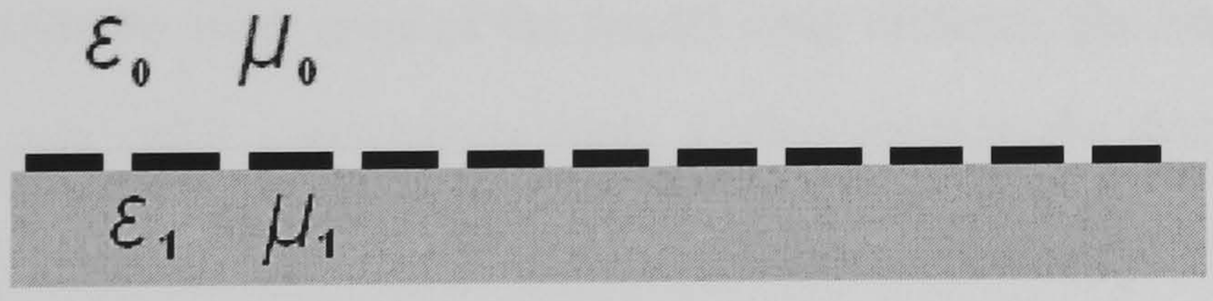

Fig. 3.2 Array with ungrounded dielectric substrate.

3.3.1 Plane-wave Response

Following the formulation of chapter 2, the matrix equation (2.13) is derived. RWG basis functions are used to model the fractal elements with 21 by 21 Floquet modes. An enlarged view of a section of the fractal element is depicted in Fig. 3.1 showing the triangular facets used to model the induced current. The elements of the Z matrix are calculated for a range of frequencies. As an example the values of a random Z_{ji} element are shown in Fig. 3.3. It is evident that the Z matrix element values, both real and imaginary, vary smoothly and regularly with frequency. This allows for the implementation of the interpolation technique described in section 2.6.

The interpolation scheme is employed to compute the fractal EBG array response under plane wave incidence. We consider a dielectric substrate for the array with $\varepsilon_r = 2.2$ and thickness 1.13 mm. The Z matrix is calculated only at three frequency points at 5, 10 and 15GHz, and the remaining matrix values are interpolated using equations (2.50) and (2.51) for the whole frequency range.

In order to show how the miniaturised and multiband features are achieved, we start the study with the plane-wave response of the original tripole array, where the fractal tripole array of Fig. 3.1 is based upon. The tripole element, as shown in Fig. 3.4, has the same size with the main arms of the fractal array element, the length and the width of which are 5 mm and 0.1 mm respectively. Following that, the first-, the second- and the third-order branches with the lengths of 2.5mm, 1.25mm and 0.625mm are added into the geometry step by step (Fig. 3.5 – Fig.3.7).

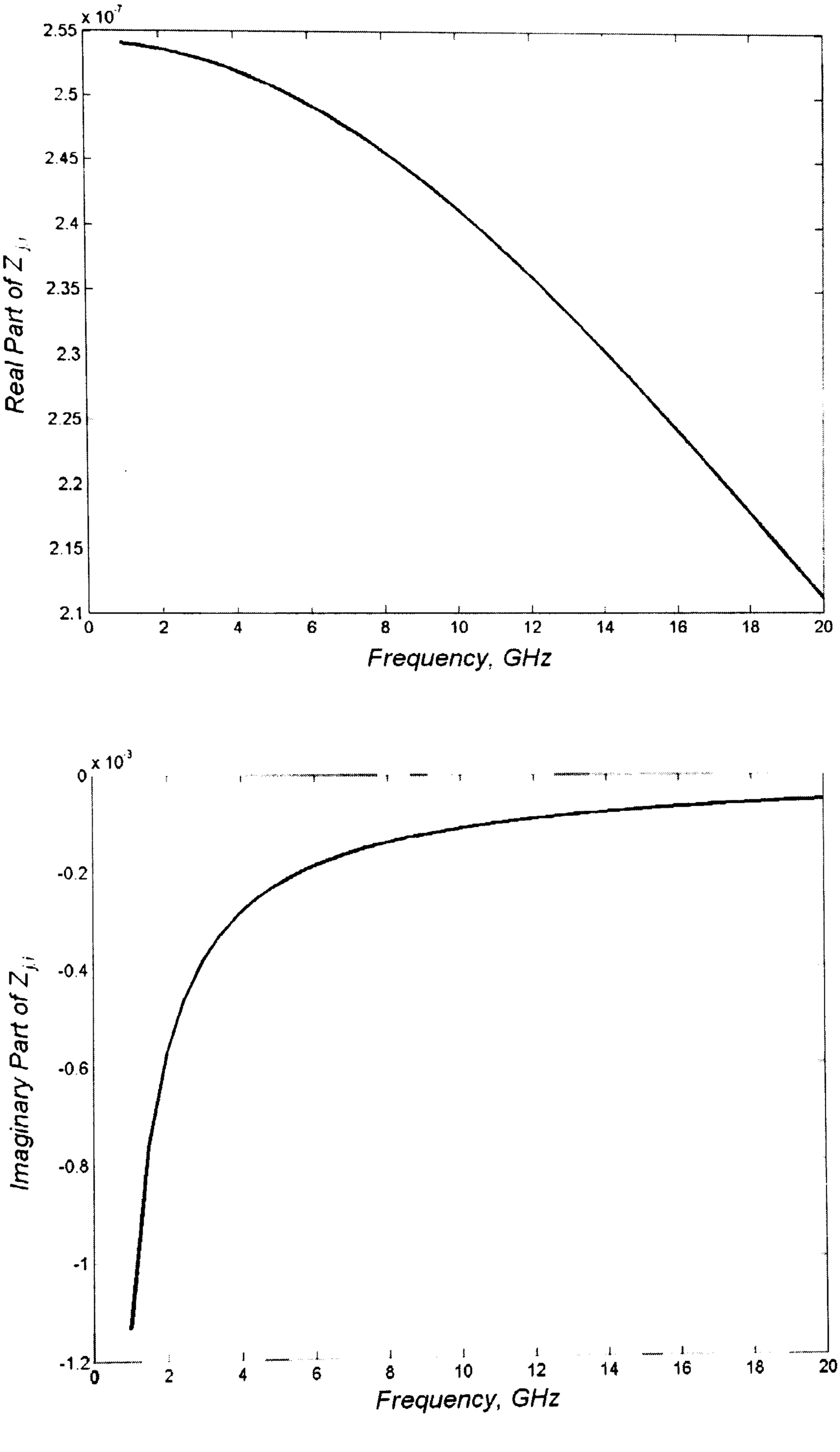

Fig. 3.3 Variation of the impedance matrix elements versus frequency.

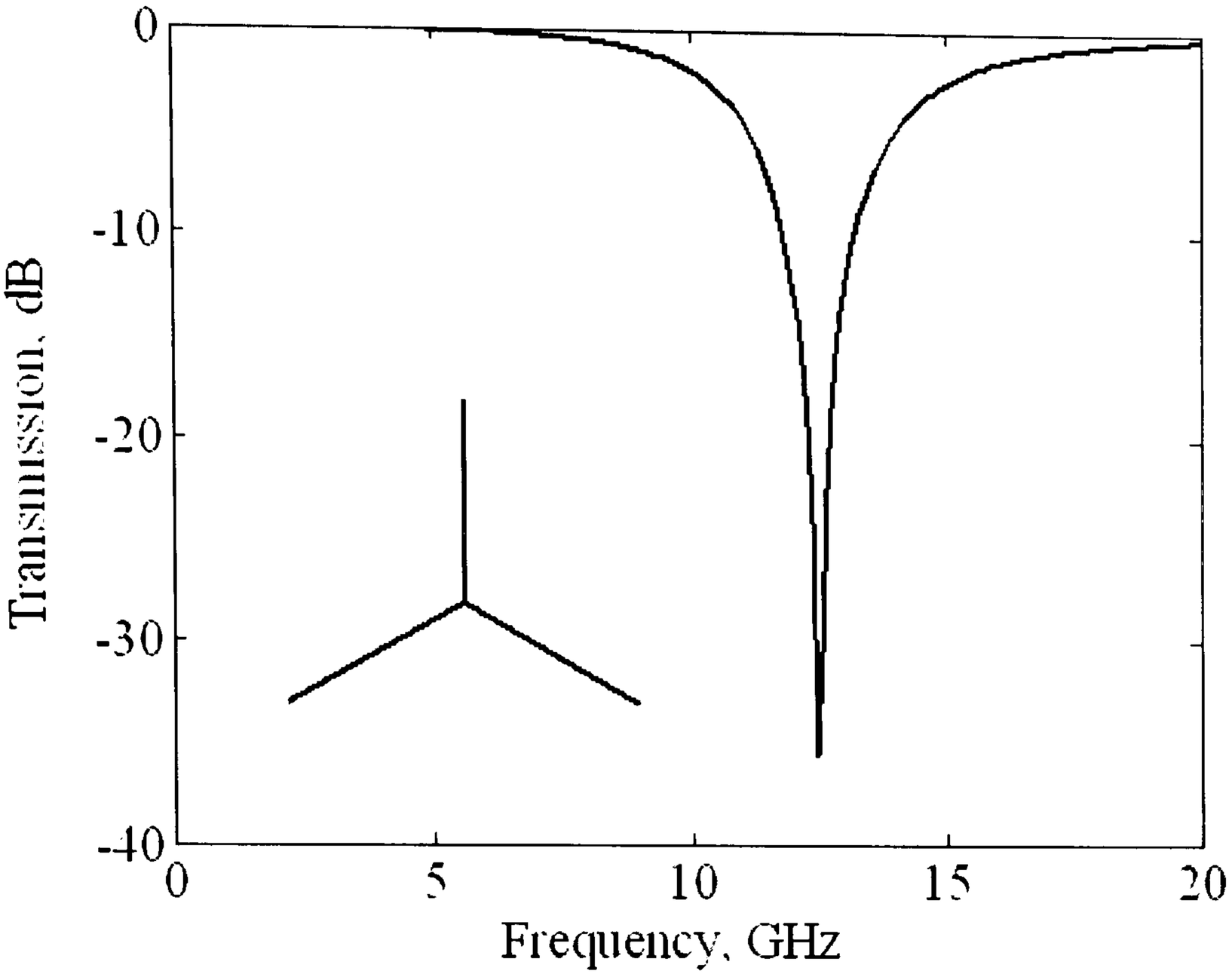

Fig. 3.4 Transmission coefficients of the original tripole array.

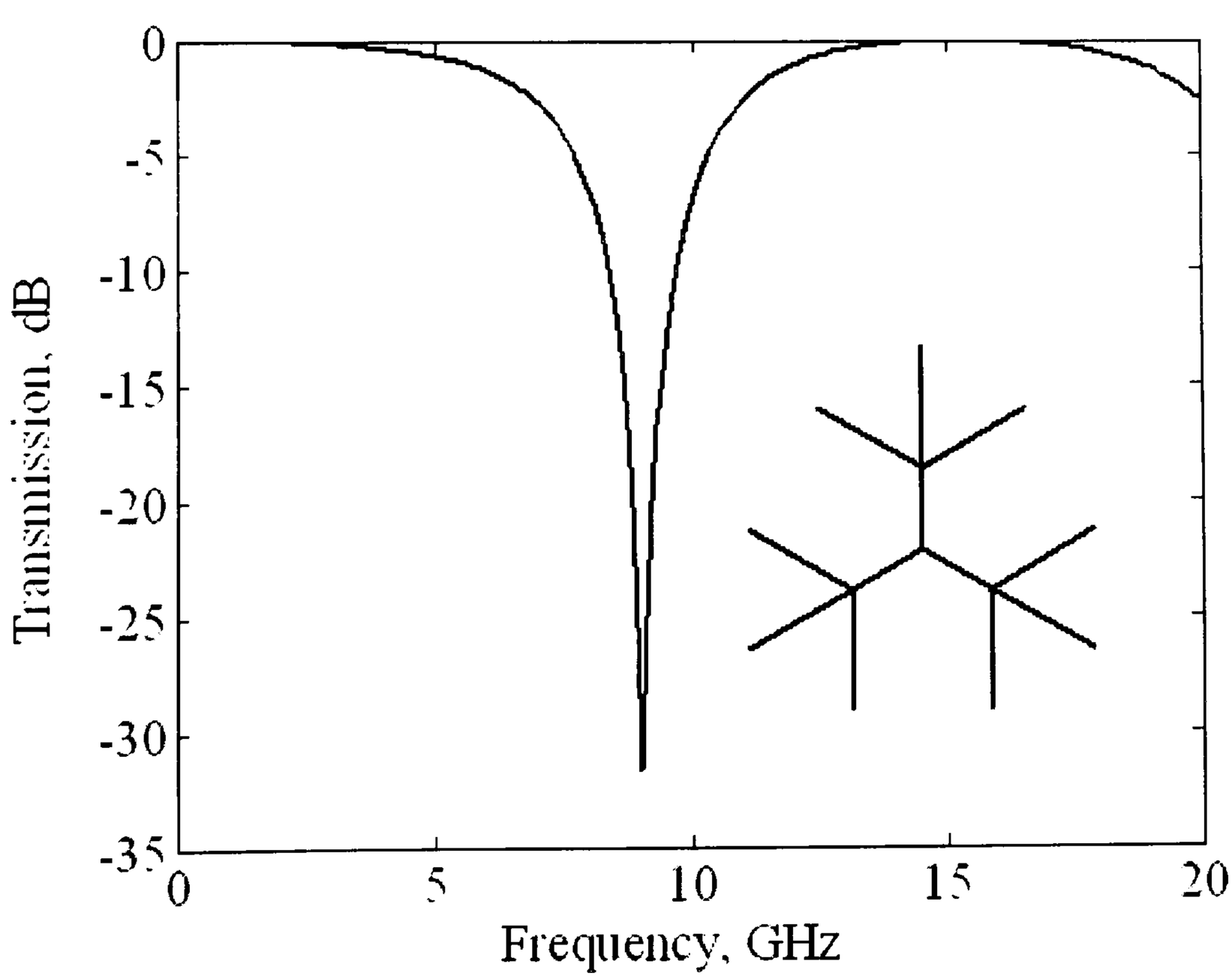

Fig. 3.5 Transmission coefficients of the one-order-fractal tripole array.

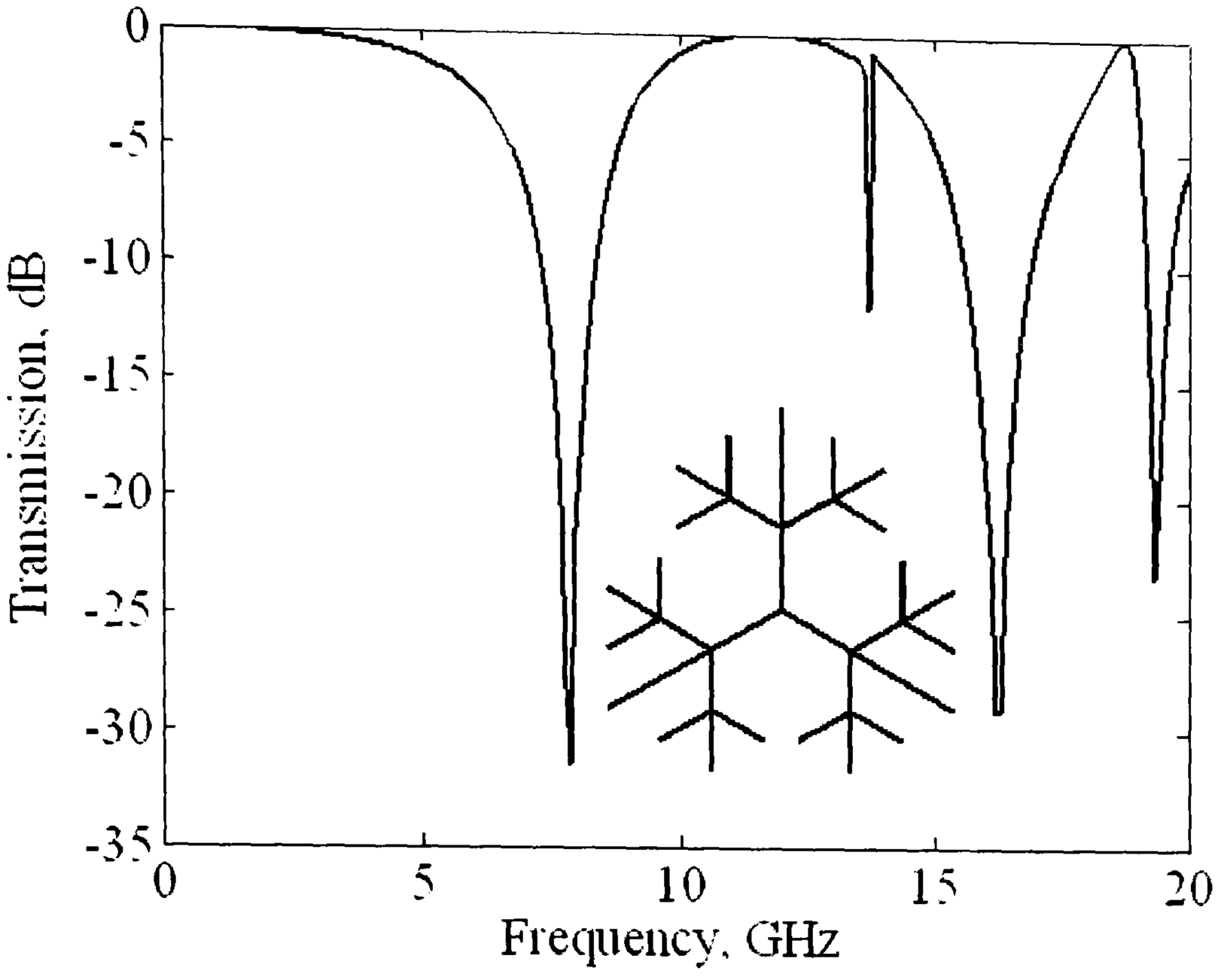

Fig. 3.6 Transmission coefficients of the two-order-fractal tripole array.

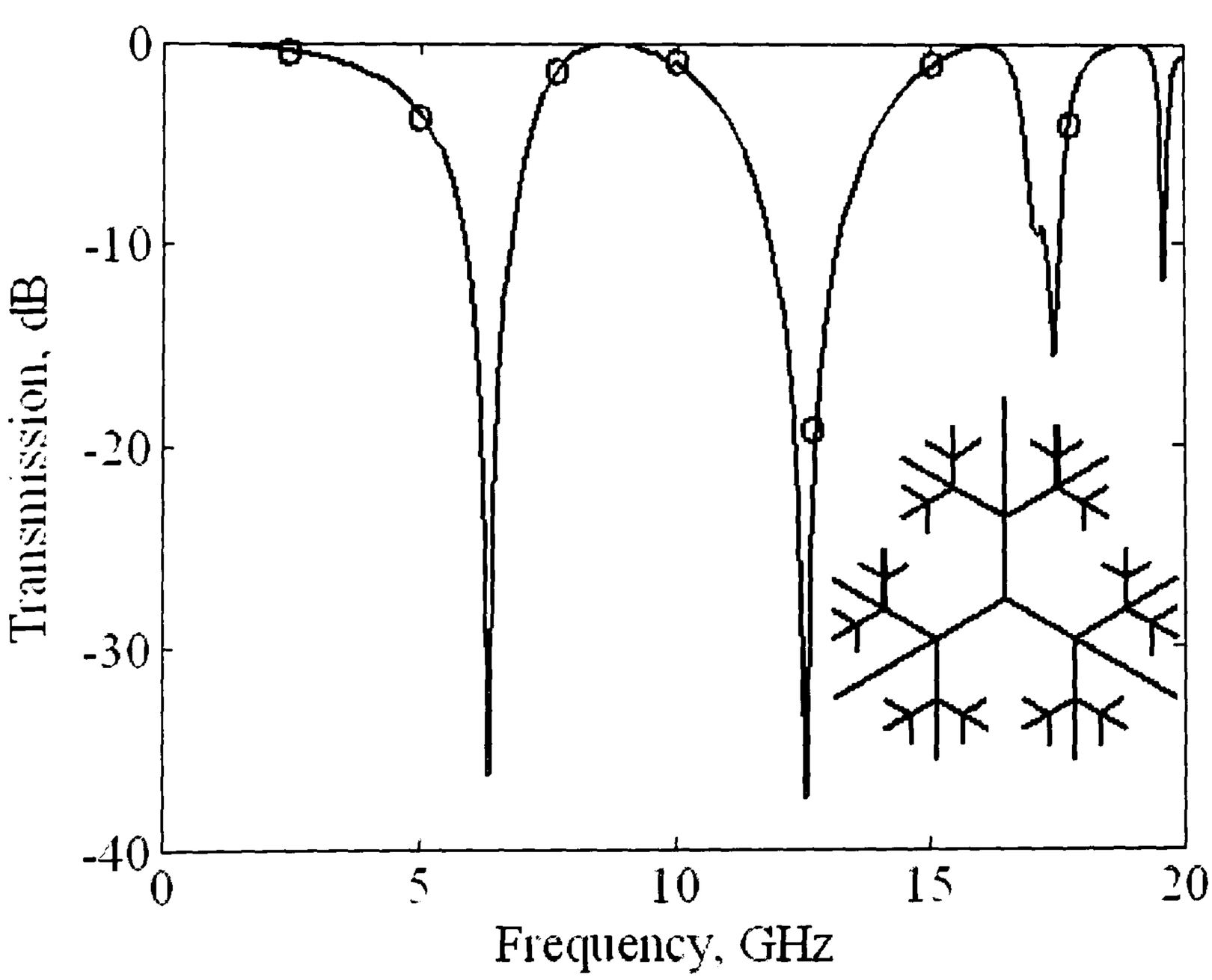

Fig. 3.7 Transmission coefficients of the three-order-fractal tripole array.

The efficient modelling technique used here allows for fast calculation and investigation of the array plane-wave responses. For example, in the analysis of the two-order-fractal array in Fig. 3.6, 84 basis functions and 41 by 41 Floquet modes are applied. To produce a smooth response and identify the resonance-stopband between 6GHz to 9GHz, 30 points are required to be calculated without impedance interpolation, which takes about 90 minutes in a Dell workstation with 2GHz CPU and 1GB memory. However, with interpolation, we need calculate only three points in 584 seconds. Therefore, the computing is accelerated by about 10 times.

The transmission coefficients of the original tripole array and the multi-order fractal arrays are presented in Fig. 3.4 – Fig. 3.7. It can be seen that when the higher-order branches are added into the tripole element, the fractal arrays exhibit a floating of the first-order resonant point from about 13GHz to the lower frequencies of 9GHz, 8GHz and 6GHz. The resonant frequency of the three-order-fractal tripole array is at approximately half the frequency of the simple tripole resonance. Moreover, with the increase of the branch orders, additional resonances are obtained at higher frequencies within the interested frequency range between 0 to 20GHz, yielding multiband responses. The small circles in Fig. 3.7 are results calculated without interpolation as a comparison.

According to the transmission coefficients in Fig. 3.4 – Fig 3.7, surface current distributions on the elements are plotted in Fig. 3.8 – Fig. 3.14 to show how the elements work at their resonant frequency points. The tripole and the one-order-fractal elements in Fig. 3.8 and Fig. 3.9 act as the half-wavelength resonators introduced in chapter 1. Because the branches increase the electrical length of the fractal element, the one-order-fractal array makes the resonant frequency point move to a lower frequency at 9GHz while the original tripole array works at 13GHz. Current

distributions on the element of the two-order-fractal array are given out in Fig. 3.10 and Fig. 3.11. It is found that the first-order resonance is mainly contributed by the main arms while the second-order resonance owes to the first-order branches. Similarly with the three-order-fractal array element in Fig. 3.12 – Fig. 3.14, the main arms, first-order branches and second-order branches generate the first- to the third-order resonances respectively.

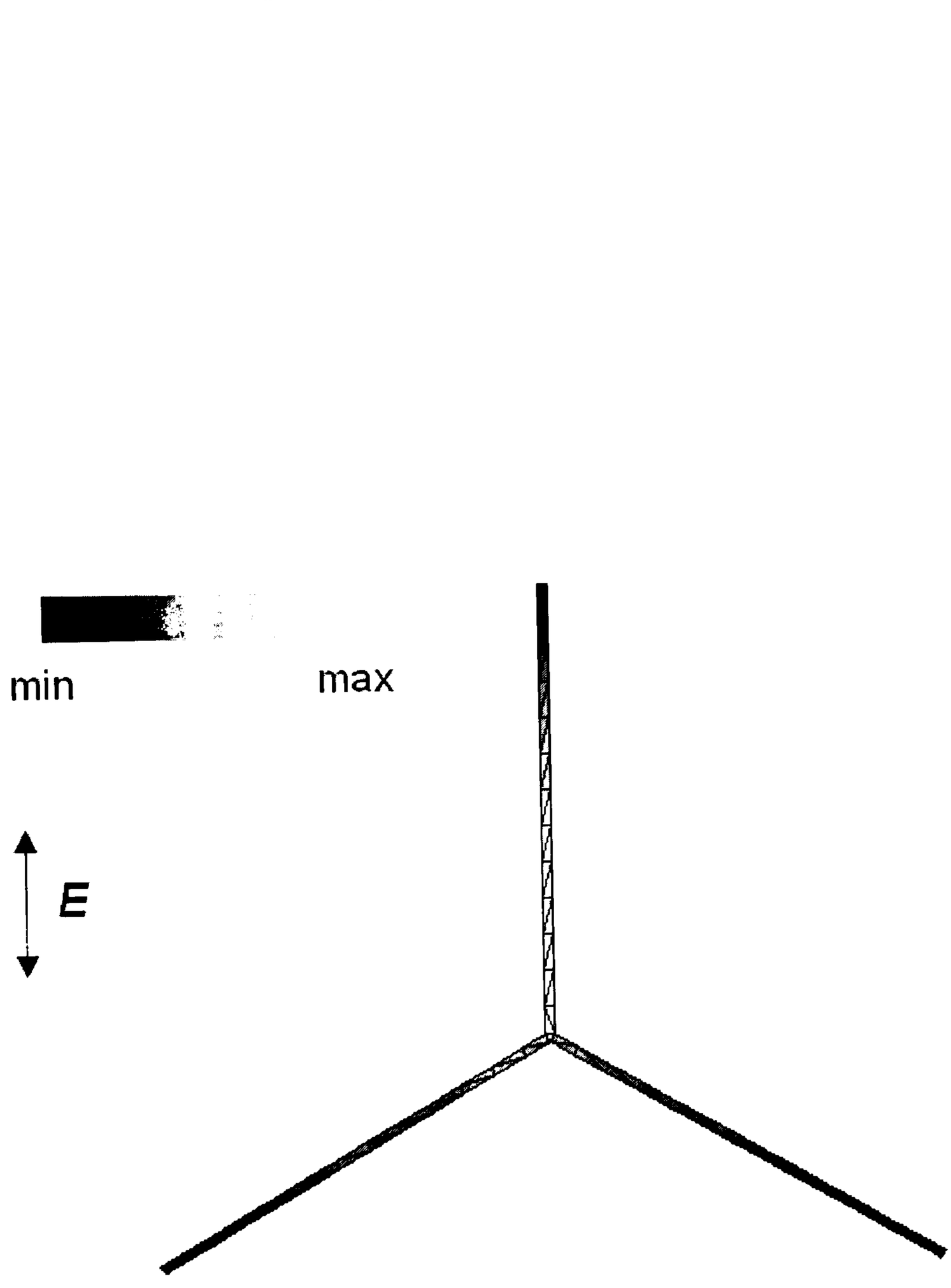

Fig. 3.8 Current distribution on the element of tripole array at 13GHz.

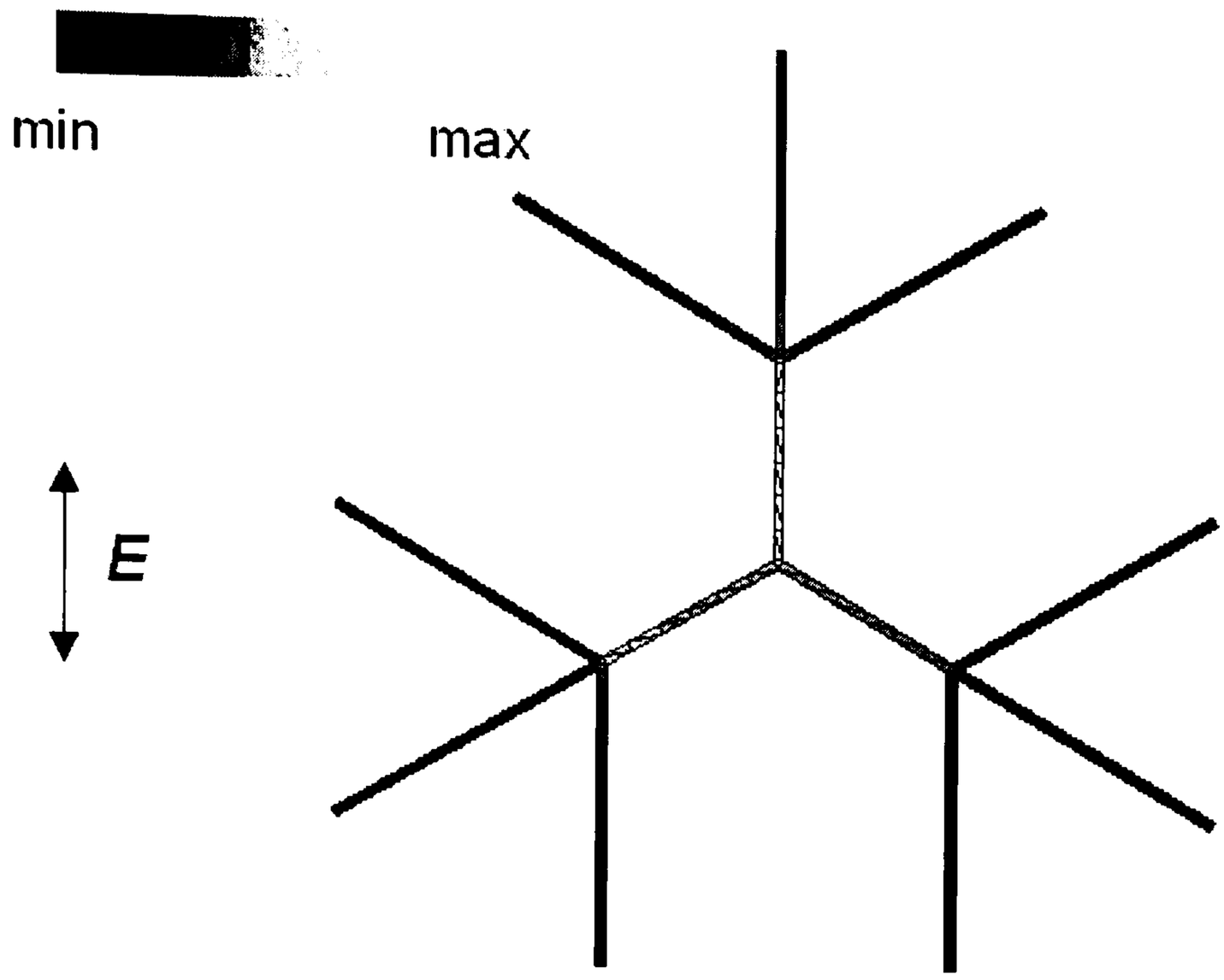

Fig. 3.9 Current distribution on the element of one-order-fractal array at 9GHz.

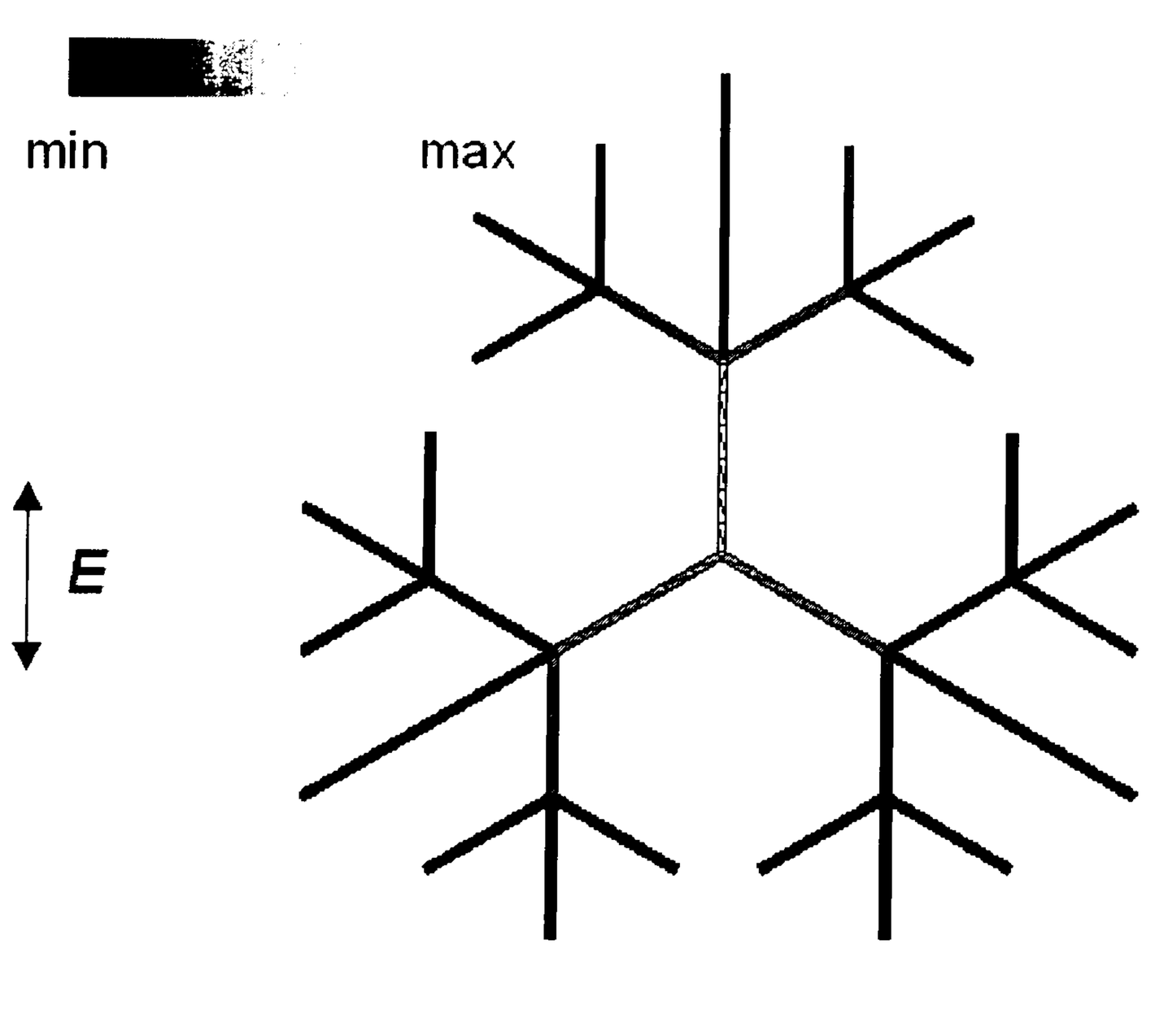

Fig. 3.10 Current distribution on the element of two-order-fractal array at 8GHz.

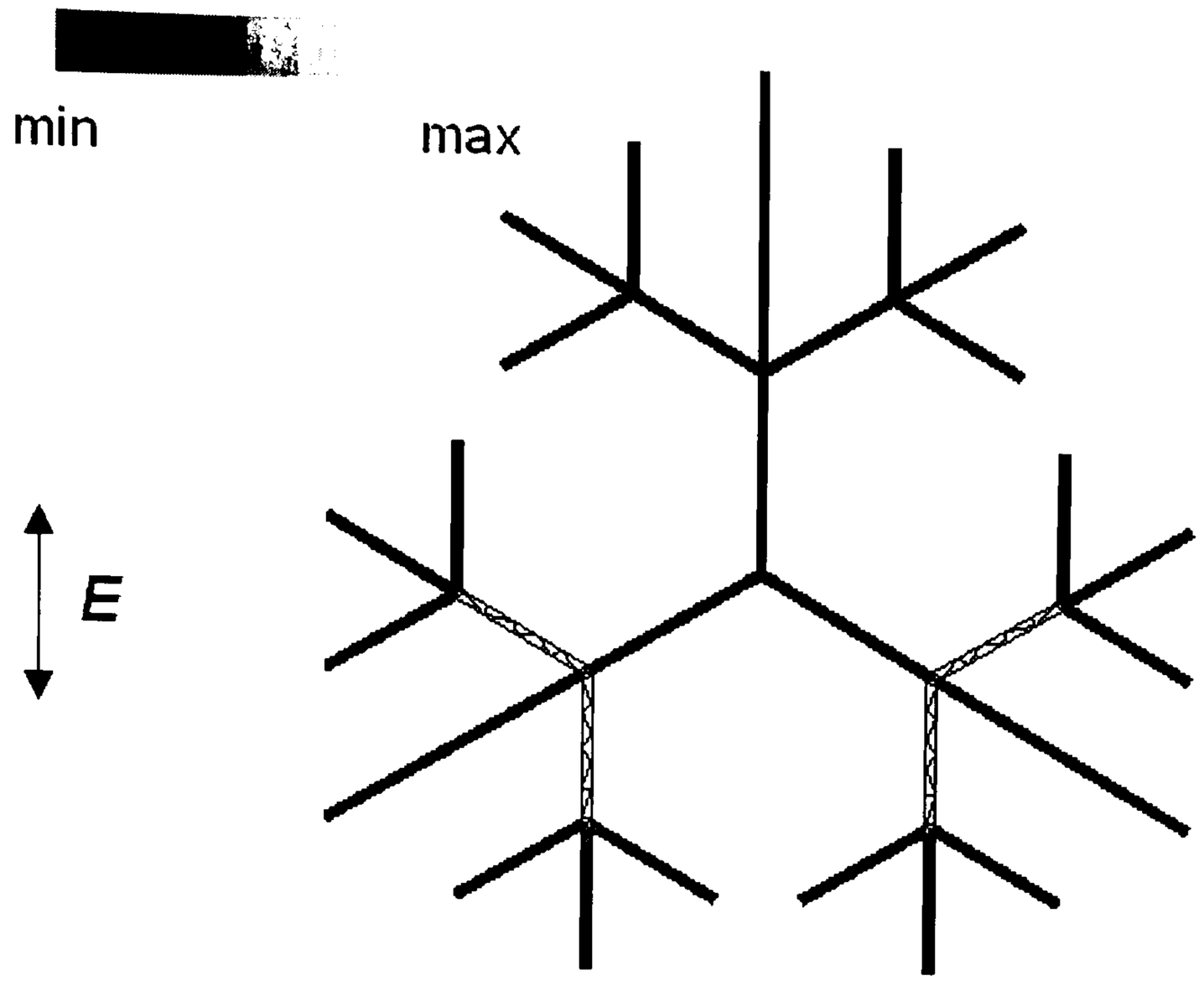

Fig. 3.11 Current distribution on the element of two-order-fractal array at 16 GHz.

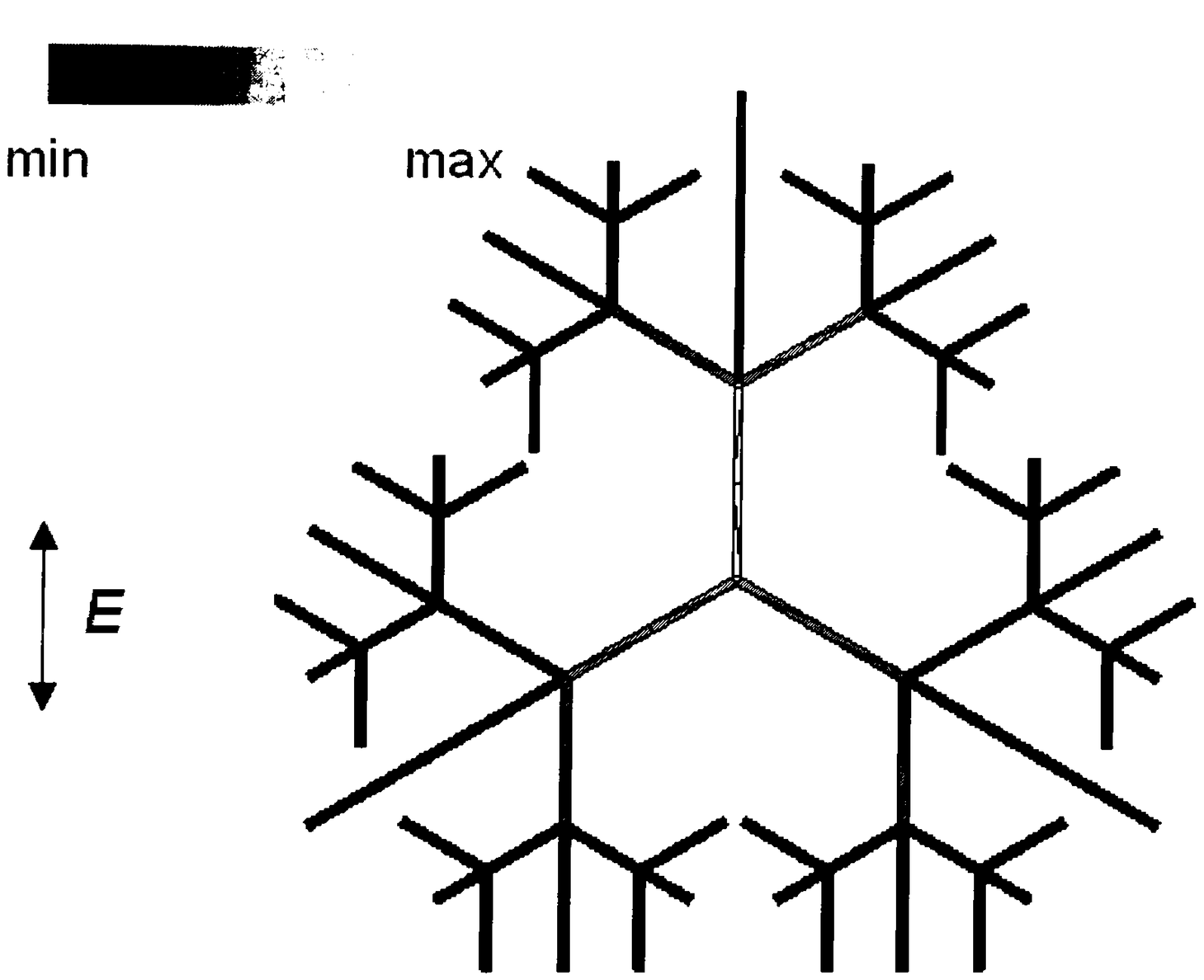

Fig. 3.12 Current distribution on the element of three-order-fractal array at 6GHz.

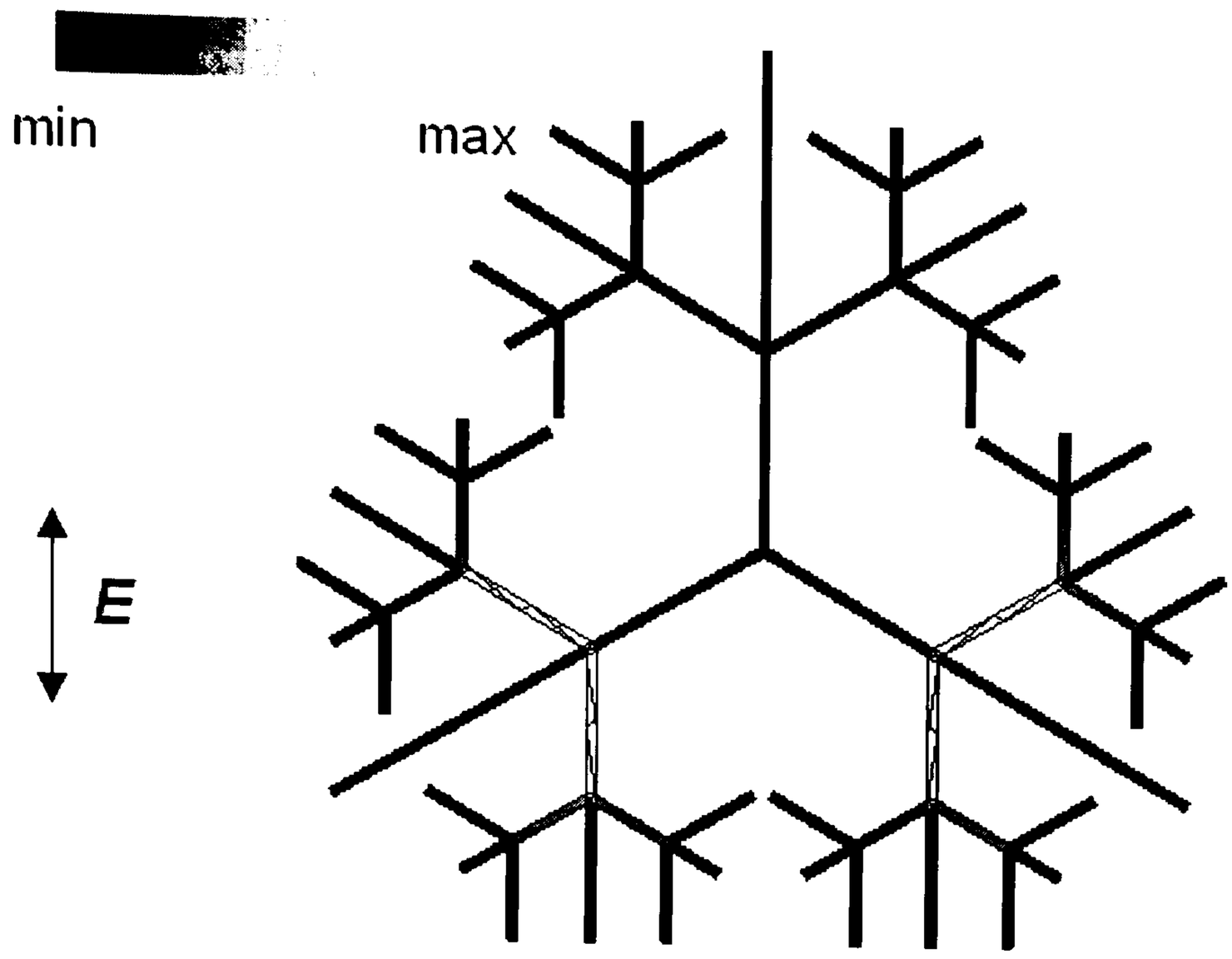

Fig. 3.13 Current distribution on the element of three-order-fractal array at 13GHz.

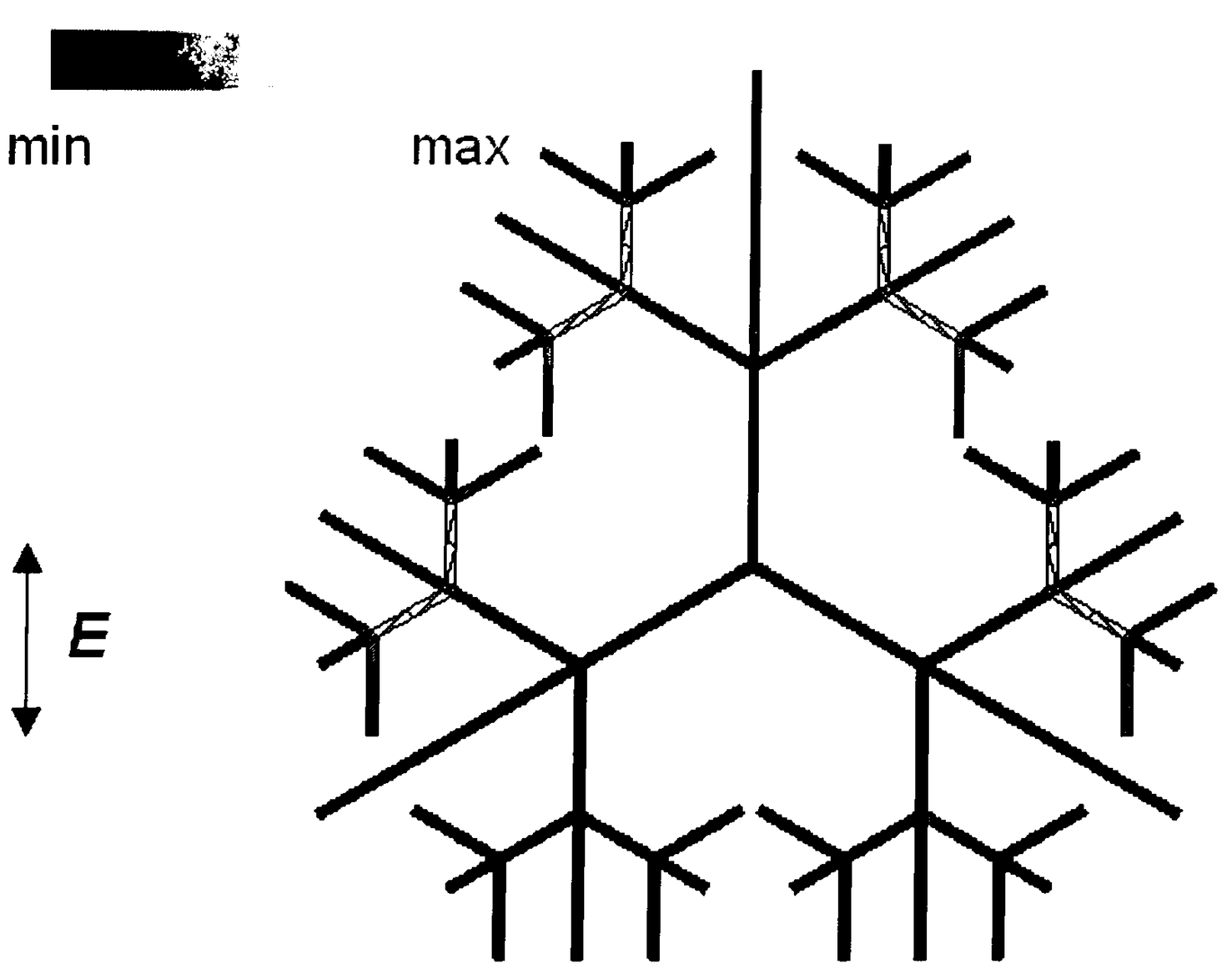

Fig. 3.14 Current distribution on the element of three-order-fractal array at 17GHz.

3.3.2 Dispersion Characteristics

To study the response of the structures to surface wave incidence, the dispersion characteristics of the three-order-fractal array in Fig. 3.1 for its two-dimensional plane of periodicity can be calculated by solving the homogeneous version of MoM equation (2.58). The excitation matrix V in (2.13) is set to zero and the values of frequency, f, and propagation constants β_x and β_y that satisfy the equation are identified. For the set of homogeneous linear equations expressed in (2.58) to have non-trivial solutions, the determinant of the impedance matrix Z must be zero. The pairs of f and β values (real) for which the determinant becomes zero correspond to propagating modes.

As mentioned in section 2.7, conventional method finds the determinant minima by scanning the range of β for each selected frequency. However, for the flat part of the dispersion curve, as is shown in Fig. 3.15, very small frequency step $(f_2 - f_1)$ has to be chosen to find the corresponding β_1 and β_2. It is very difficult to choose the proper frequency steps when the propagation modes are hard to be predicted, which makes the calculation lack of efficiency. Moreover, when the propagation bands are narrow, modes might be missed by choosing large frequency steps.

Studying the impedance matrix of the fractal array with surface-wave excitation (θ to be 90°), smooth variation of Z_{ji} versus frequency is also derived similar to that with plane-wave excitation. This makes it possible to apply the impedance interpolation in creating the dispersion diagrams as well as the plane-wave responses. As is indicated in Fig. 3.15, for a selected β_0, the homogeneous version of MoM

equation is solved at just a few frequency points. The impedance matrices are then interpolated with very small frequency steps in the frequency range.

The algorithm is presented in steps as the follows.

1. Decide the frequency range we are working with (i.e. 0-10GHz).
2. Calculate three frequency points (f_1, f_2, f_3) of Z matrix.
3. Apply the interpolation functions to these three points to derive Z(f).
4. Calculate the determinants of Z(f) to find the minima.
5. Roughly locate the modes.
6. Repeat 1-5 around each model frequency. Three new points are chosen around each model frequency.

The variation of Z_{ji} versus frequency for the fractal element is plotted in Fig. 3.16.

An interesting characteristic, different to that of the plane-wave excitation case, is that both variations of real part and imaginary part of Z_{ji} versus frequency have the inverse function form. Therefore, both parts of Z_{ji} are interpolated using the inversion functions as

$$R(f) = A^R / f + B^R f + C^R \tag{3.1}$$

$$I(f) = A^I / f + B^I f + C^I \tag{3.2}$$

where $R(f)$ and $I(f)$ are for real part and imaginary part of the impedance matrix elements respectively $\left(Z_{ji}(f) = R_{ji}(f) + j \cdot I_{ji}(f)\right)$.

$$A_{ji}^{R} = \frac{f_1 f_2 f_3 (\mathrm{Re}[Z_{ji}(f_1)](f_2 - f_3) + \mathrm{Re}[Z_{ji}(f_2)](f_3 - f_1) + \mathrm{Re}[Z_{ji}(f_3)](f_1 - f_2))}{f_1^2 (f_2 - f_3) + f_2^2 (f_3 - f_1) + f_3^2 (f_1 - f_2)} \tag{3.3}$$

$$B_{ji}^{R} = \frac{\mathrm{Re}[Z_{ji}(f_1)] - \mathrm{Re}[Z_{ji}(f_2)] - A_{ji}^{R}(1/f_1 - 1/f_2)}{f_1 - f_2} \tag{3.4}$$

$$C_{ji}^{R} = \mathrm{Re}[Z_{ji}(f_1)] - A_{ji}^{R}/f_1 - B_{ji}^{R} f_1 \tag{3.5}$$

$$A_{ji}^{I} = \frac{f_1 f_2 f_3 (\mathrm{Im}[Z_{ji}(f_1)](f_2 - f_3) + \mathrm{Im}[Z_{ji}(f_2)](f_3 - f_1) + \mathrm{Im}[Z_{ji}(f_3)](f_1 - f_2))}{f_1^2 (f_2 - f_3) + f_2^2 (f_3 - f_1) + f_3^2 (f_1 - f_2)} \tag{3.6}$$

$$B_{ji}^{I} = \frac{\mathrm{Im}[Z_{ji}(f_1)] - \mathrm{Im}[Z_{ji}(f_2)] - A_{ji}^{I}(1/f_1 - 1/f_2)}{f_1 - f_2} \tag{3.7}$$

$$C_{ji}^{I} = \mathrm{Im}[Z_{ji}(f_1)] - A_{ji}^{I}/f_1 - B_{ji}^{I} f_1 \tag{3.8}$$

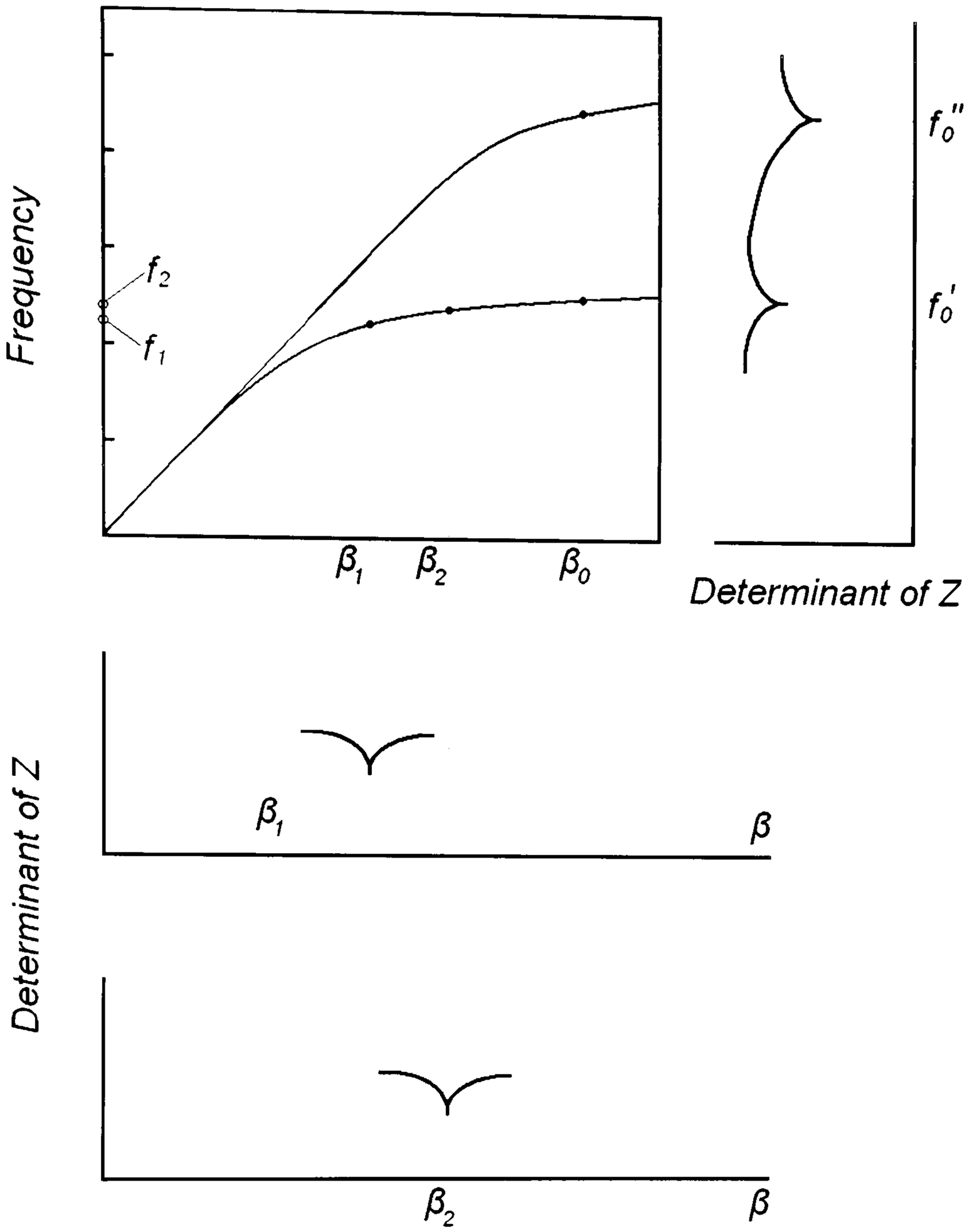

Fig. 3.15 Two different methods to find the determinant minima.

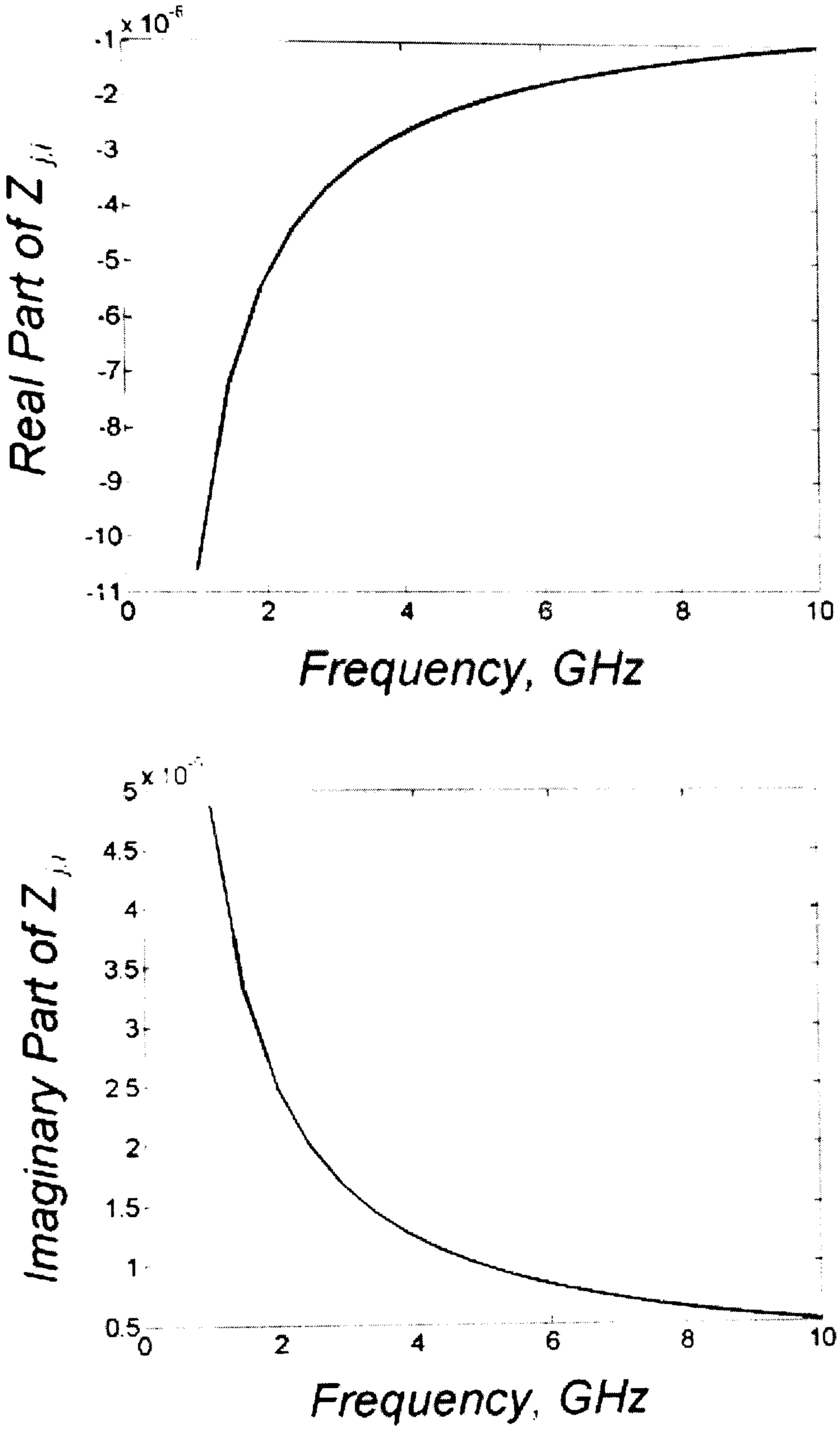

Fig. 3.16 Variation of Z_{ji} versus frequency for the fractal element.

Tripole and certain tripole-like elements, such as the fractal element studied here, exhibit symmetrical two-dimensional band gap properties when arranged on a hexagonal lattice [3]. This is because the symmetry of the elements in conjunction to the lattice yields an irreducible Brillouin zone on the reciprocal lattice (shown as inset in Fig. 3.18). The grey area has an aperture angle of $30°$. The values of β_x and β_y are changed accordingly in order to scan the Γ-X, X-M, and M-Γ directions of the Brillouin zone. The interpolation technique has been applied in order to accelerate the frequency sweeps for each pair of β_x and β_y values. Unlike the plane wave response case, large interpolation steps have not produced successful results. The plots of the determinant with frequency were smooth and it was not possible to identify any minima. However, when smaller interpolation steps were used, the minima started appearing as sharp notches, similar to the way they appear on the plots when interpolation is not used. This observation paved the way for a thorough study on the accuracy of the position of the minima as a function of the interpolation step. The full range of frequencies was broken down to smaller sections where interpolation was applied. An error value defined as the difference between the spectral positions of a minimum with and without interpolation has been calculated for different interpolation steps. Fig.3.17 shows the percentage error value in calculated roots of the determinant of the Z-matrix due to the application of the interpolation technique with different interpolation steps. When the step is 2 GHz the error varies with frequency between 2.5-6%. For an interpolation step equal to 1 GHz the error becomes substantially smaller, less than 1% which corresponds to a relatively good accuracy of the final result. Further reduction of the step to 0.5GHz improves the accuracy slightly.

It is worth noting that the frequency step applied in the dispersion analysis is much smaller than that in the plane wave analysis, because there is a larger sensitivity of the

homogeneous equation to interpolation errors. This can be explained as follows:

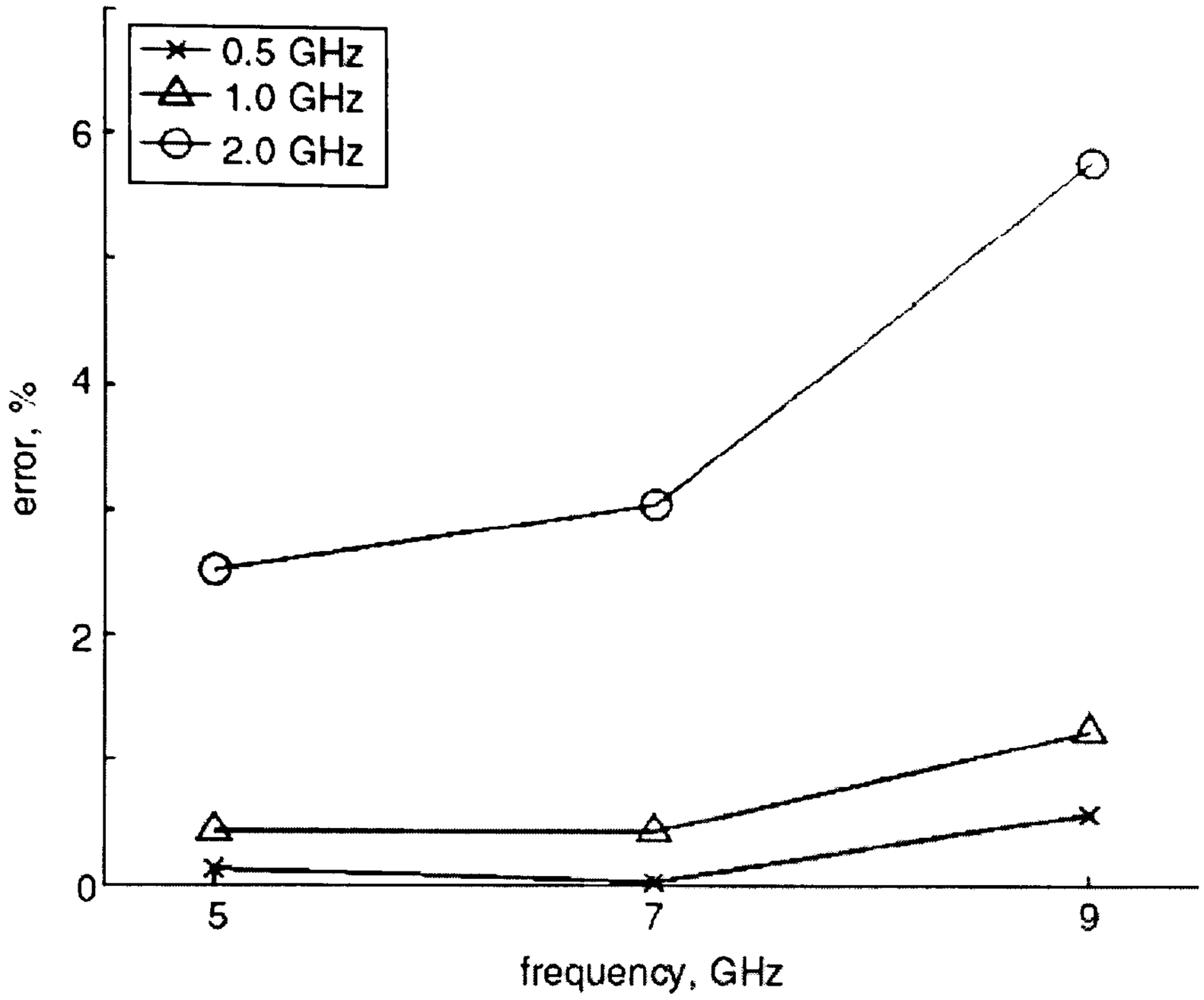

Fig. 3.17 Error in calculated roots of the determinant of the Z-matrix due to the application of the interpolation technique with different interpolation steps.

Consider that the error for each element in an *N*-by-*N* impedance matrix is

$$e(f)=\left|\frac{Z_{j,i}^{\text{int}}(f)-Z_{j,i}(f)}{Z_{j,i}(f)}\right|,\quad (0<e<<1) \tag{3.9}$$

When analysing the transmission response, we solve the matrix equation $[Z][I]=[V]$

as $[I]_N = [Z]^{-1}_{N\times N}[V]_N$. Solving the homogeneous equation $[Z][I]=[0]$ for the dispersion diagram, we calculate the determinant of the Z matrix as

$$|Z| = \sum_{i=1}^{N} Z_{j,i} C_{j,i}\,,\quad C_{j,i} = (-1)^{i+j} M_{j,i} \tag{3.11}$$

where $M_{j,i}$ is the minor of the Z matrix.

An estimate error of the determinant in this case is

$$E = N\left(1-(1-e)^{N}\right) \approx N^2 e \tag{3.12}$$

According to the analysis above, when the number of the basis function N is large, errors in the dispersion diagram will be much greater than that in the transmission response if we choose the same interpolation step.

Based on the above study an interpolation step of 1GHz has been used to produce the dispersion diagram of the fractal EBG array as shown in Fig. 3.18. The first few TE propagating modes are shown. TM modes always lie on the light line for ungrounded planar arrays. For comparison purposes, some random points derived without applying interpolation are also shown in the same graph. A very good agreement is observed between the results with and without interpolation. The fractal array exhibits multiple band gaps. Compared to the simple tripole-element array response, a significant reduction of the first band gap frequency has been achieved. This property is advantageous for the implementation of miniaturized and multiband planar EBG structures.

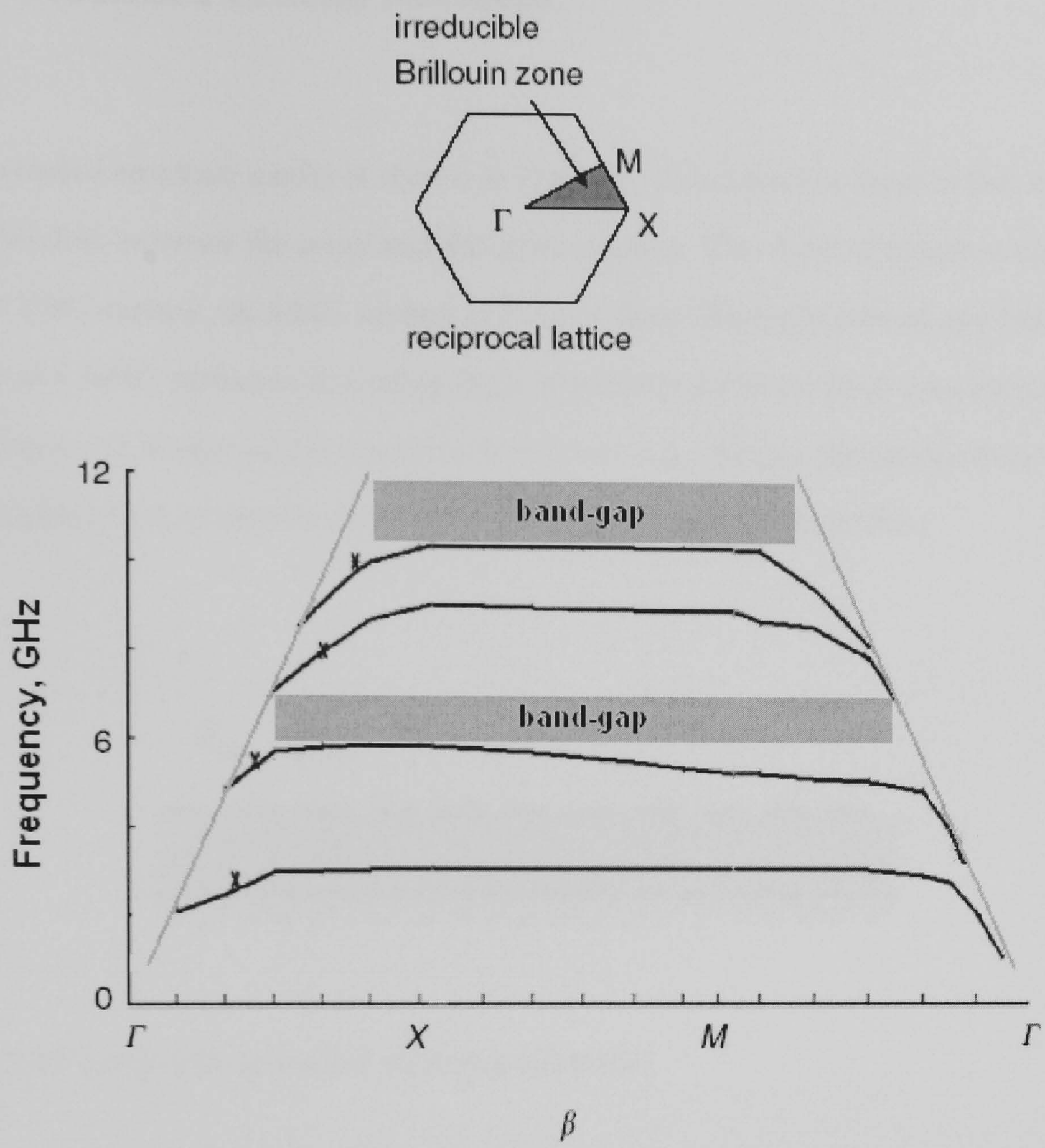

Fig. 3.18 Dispersion diagram of ungrounded fractal EBG structure.

——— TE modes with interpolation

light line

X points of TE modes without interpolation

3.4 Grounded Fractal Surfaces

A grounded structure model is shown in Fig.3.19. The dielectric layer in this model is sandwiched between the array and the ground plane. This type of structure can work as an EBG surface, an AMC surface or both of them. Recently several applications of EBG and AMC surfaces (also called high impedance surfaces) have been proposed for the improved design of microwave components (e.g. various microstrip devices). On this section both properties are studied for the grounded fractal surface.

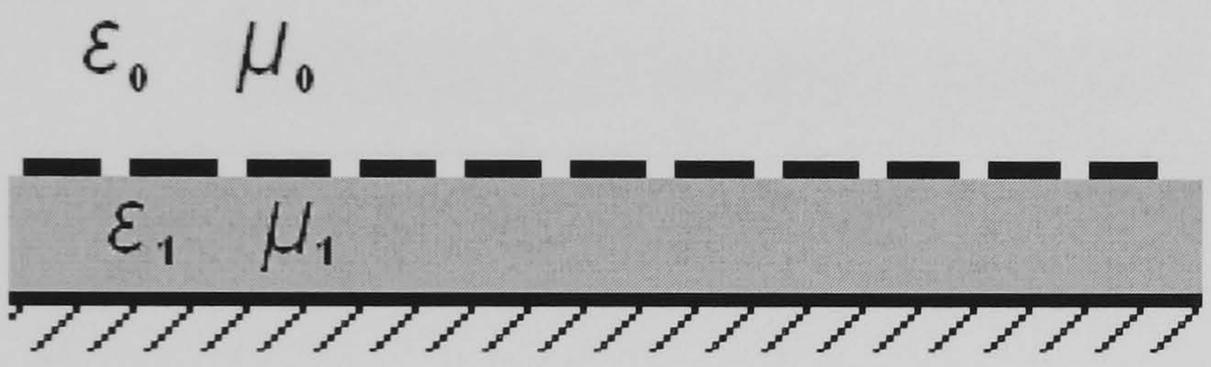

Fig. 3.19 Array with grounded dielectric substrate.

3.4.1 Grounded Fractal EBG Surfaces

Similar to the ungrounded EBG surfaces, grounded EBG surfaces can show band-gap features with respect to surface waves. The dispersion diagram of a grounded EBG surface with the array of Fig. 3.1 is presented in Fig.3.20. The dielectric constant and the thickness are the same with those of the ungrounded structures studied above. Compared with the dispersion diagram of ungrounded fractal EBG structure in Fig. 18, it can be found that that band-gaps move to higher frequencies of about 9GHz and 15GHz when the ground plane is applied.

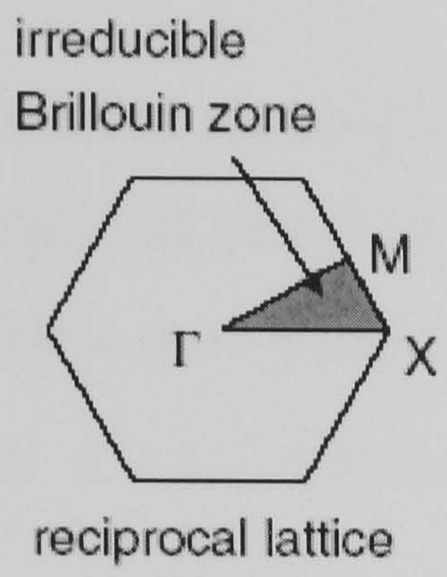

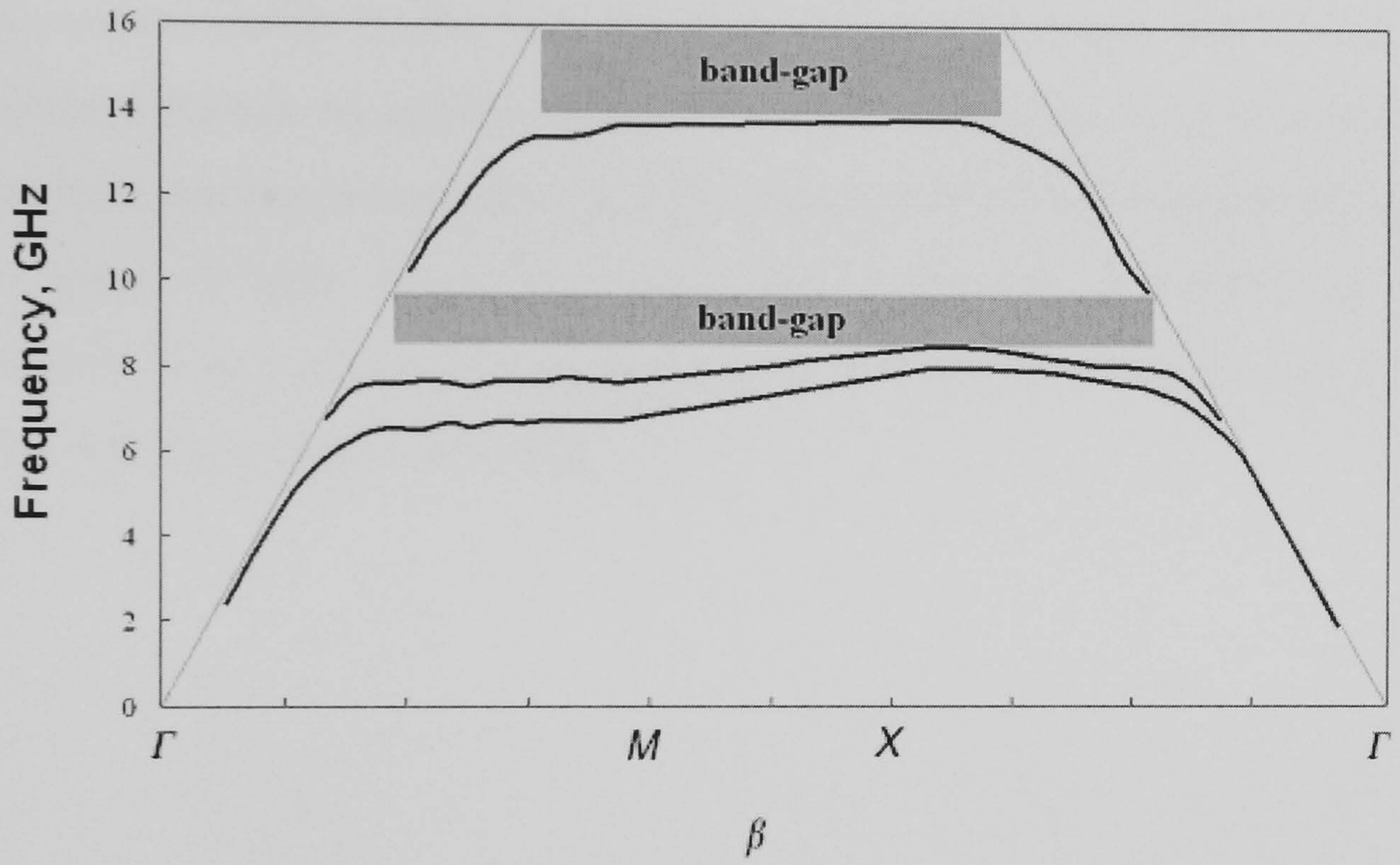

Fig. 3.20 Dispersion diagram of grounded fractal EBG structure.

3.4.2 Grounded Fractal AMC Surfaces

Recently, Artificial Magnetic Conductor Surfaces have been used in various antenna designs [12]-[14]. Fig. 3.21 – Fig. 3.24 present the AMC responses of tripole and fractal tripole arrays for normal plane wave incidence. These arrays are placed over a grounded dielectric substrate with $\varepsilon_r = 2.2$ and the thickness of 1.13 mm. Sizes and two-dimensional layouts of the arrays are the same with those of the EBG arrays in the previous section. Similar with that of the fractal EBG deigns, miniaturized and multiband features are achieved by introducing the multi-order fractal branches into the tripole elements according to Fig. 3.21 – Fig. 3.24. The AMC working bandwidths are about 1.5 GHz around the central AMC frequencies. Approximately 45% reduction of the central AMC frequency is observed comparing the three-order-fractal array with the original tripole array.

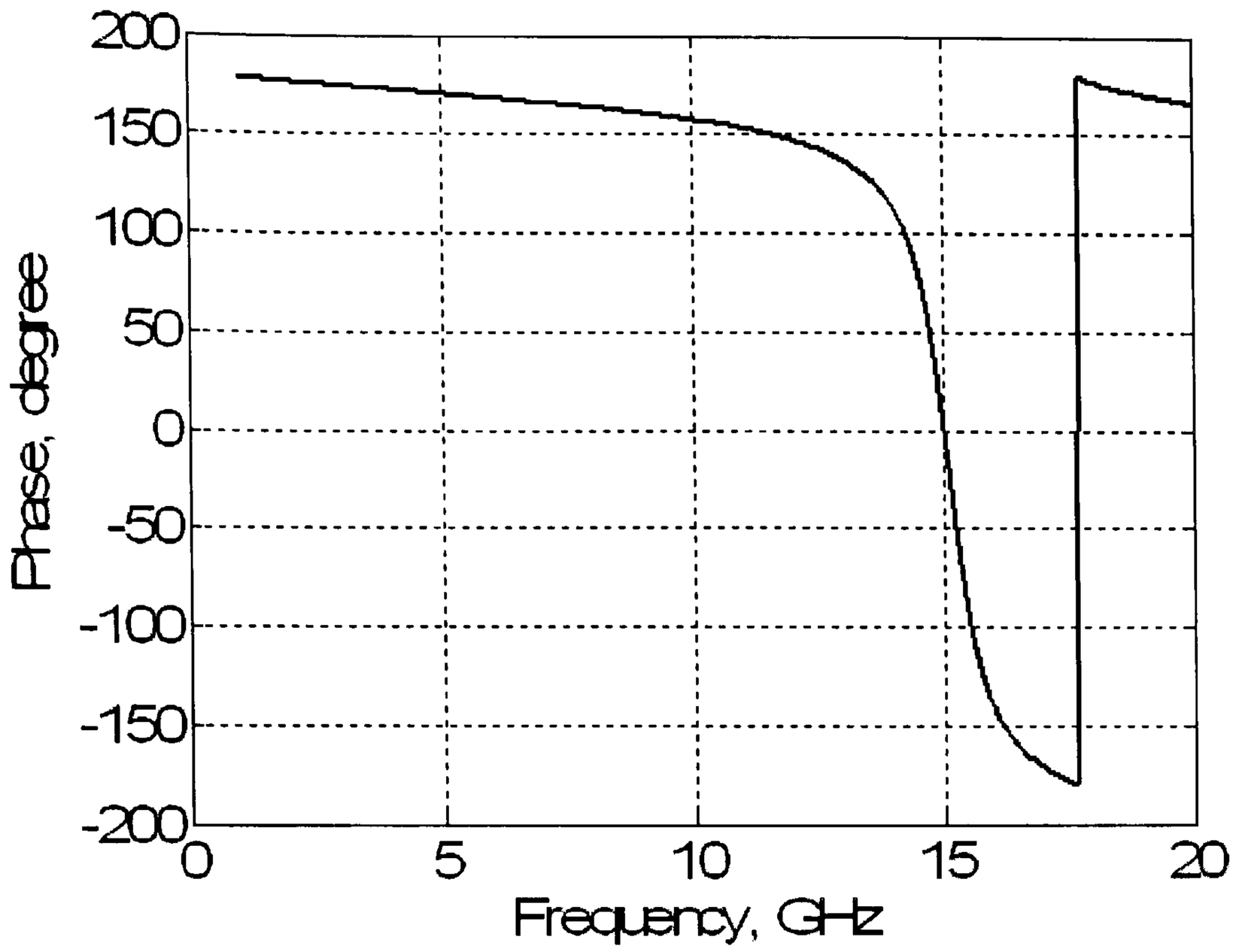

Fig. 3.21 Reflection phase of the original tripole array.

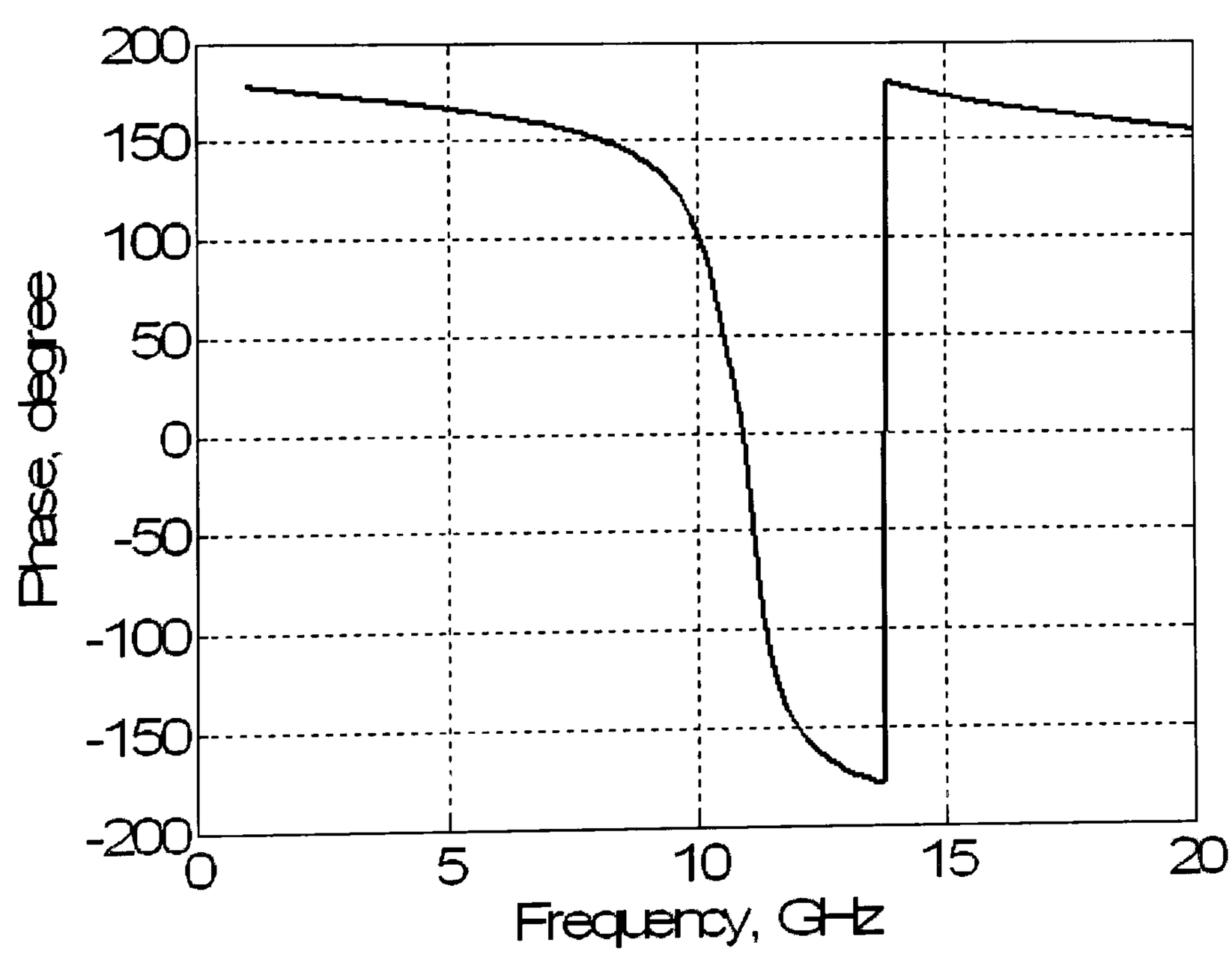

Fig. 3.22 Reflection phase of the one-order-fractal tripole array.

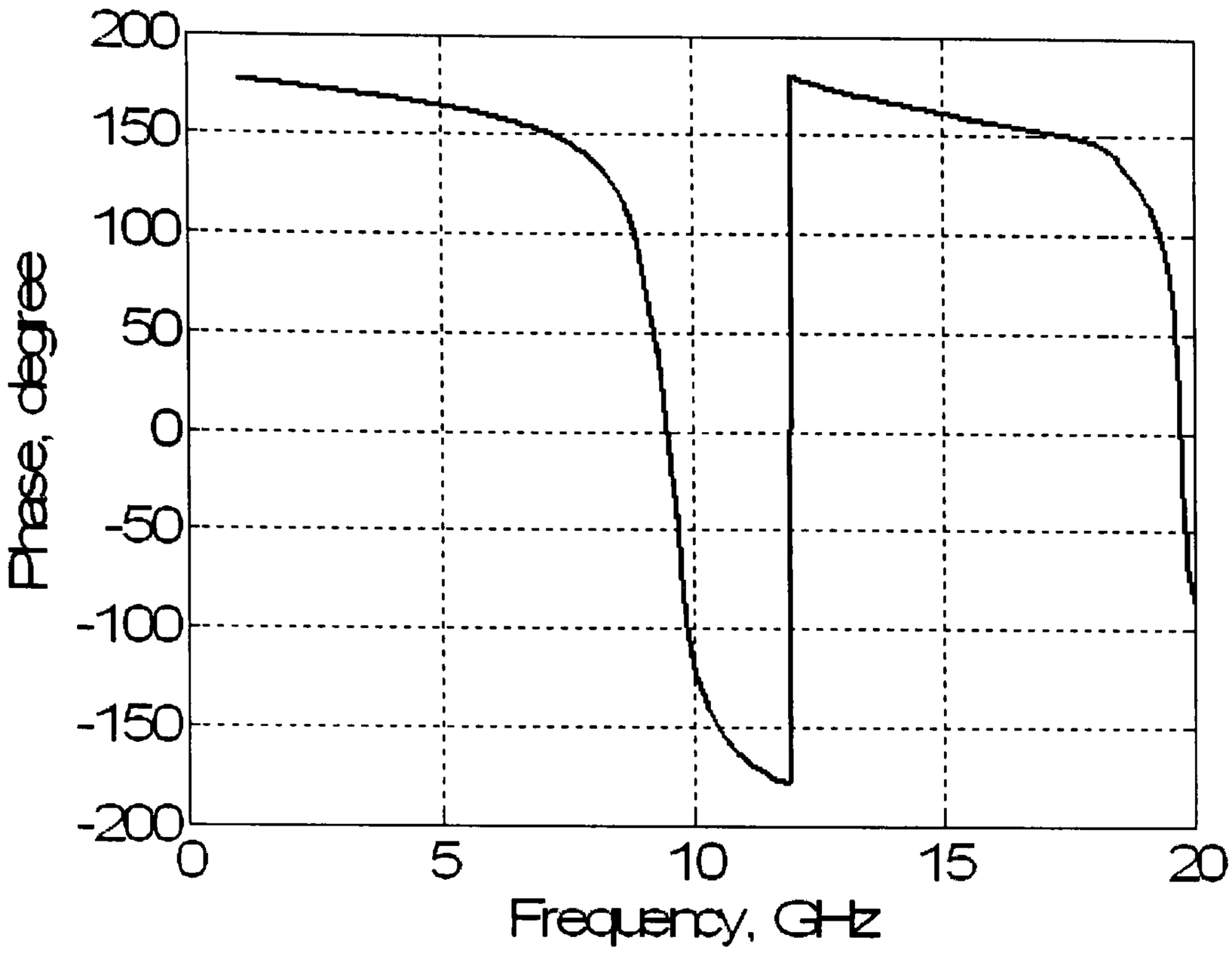

Fig. 3.23 Reflection phase of the two-order-fractal tripole array.

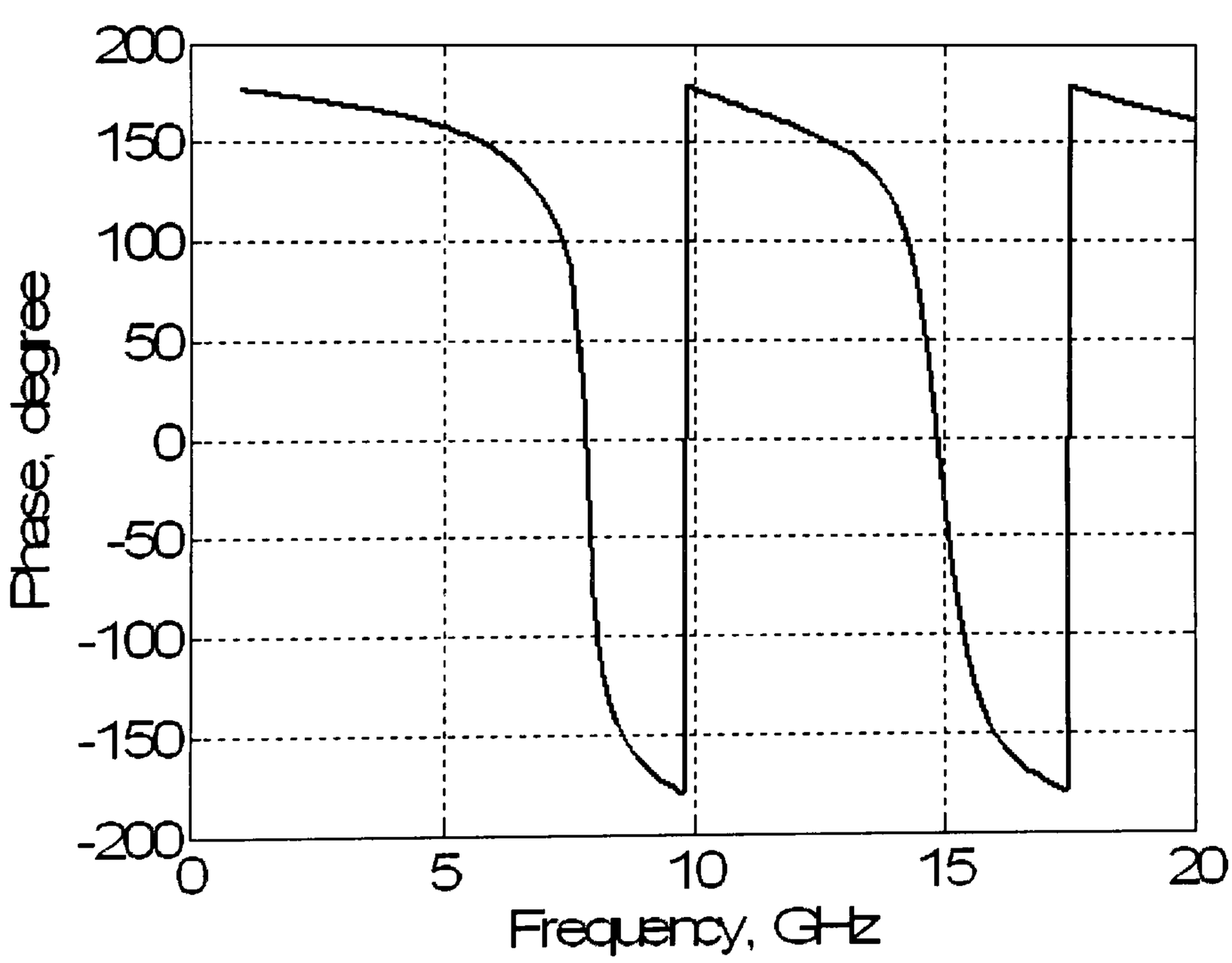

Fig. 3.24 Reflection phase of the three-order-fractal tripole array.

3.4.3 Experimental Verification

The measurements of tripole and two-order-fractal tripole arrays are made using a pair of broadband horns. The measured EBG and AMC responses for the tripole and the two-order-fractal tripole arrays are shown in Fig. 3.25 and Fig. 3.26. The accordance of the EBG locations can be observed comparing with the results in Fig. 3.4, Fig. 3.6 and Fig. 3.20. Computed AMC responses are also included in Fig. 3.26 as a comparison, which show a good agreement with those derived in the measurements.

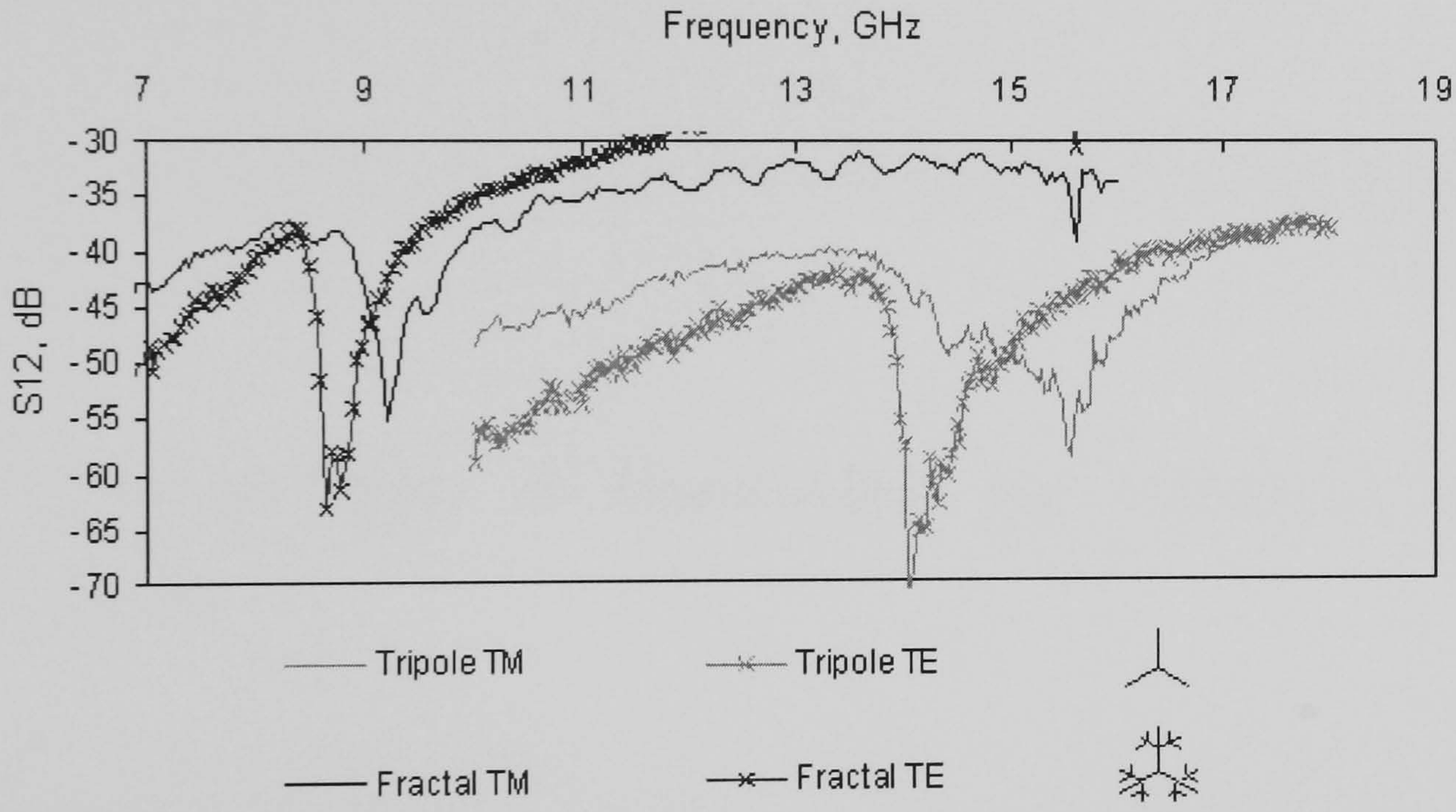

Fig. 3.25 Measured EBG performance of tripole and fractal tripole arrays (in ΓX direction).

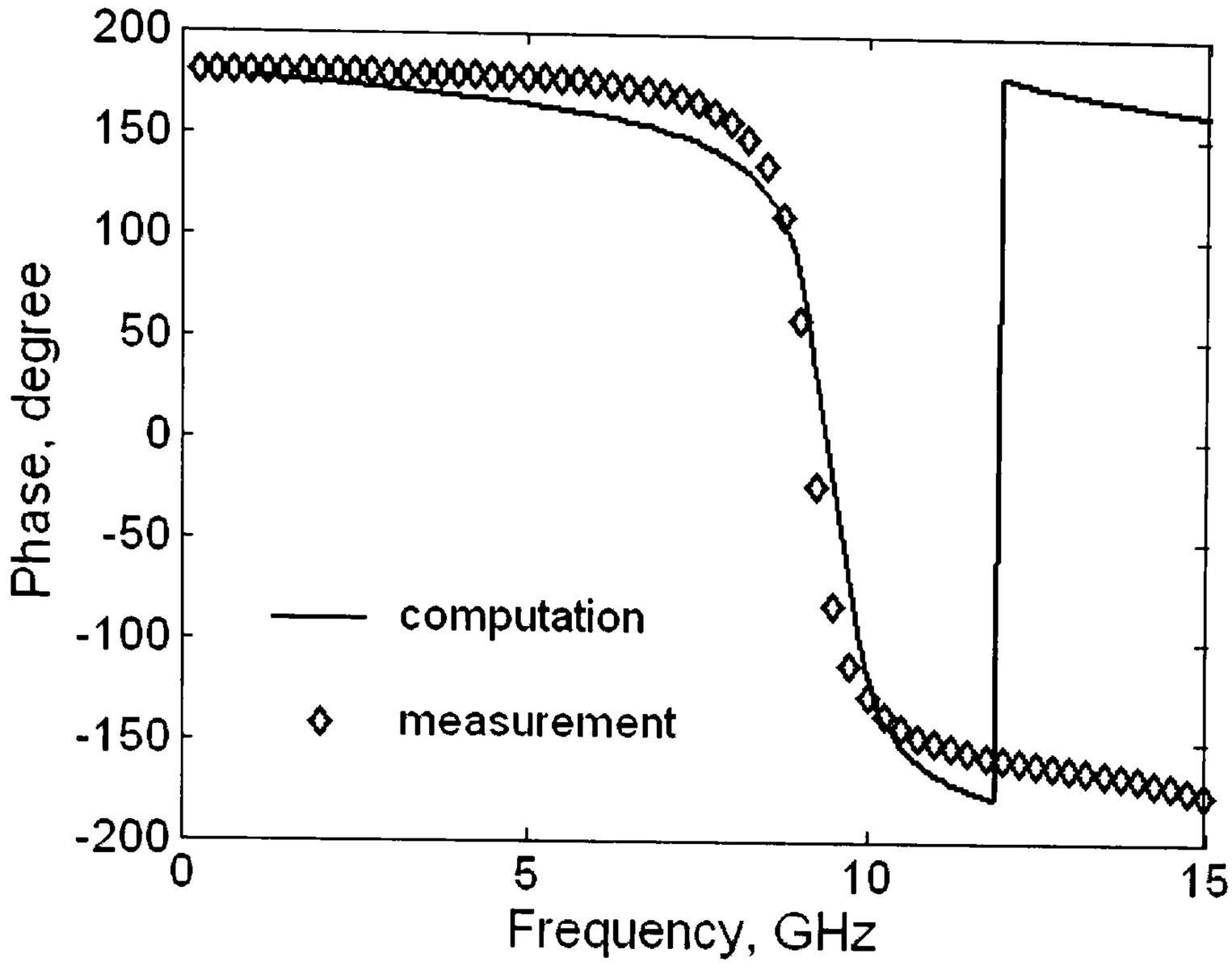

Fig. 3.26 Computed and measured AMC responses for two-order-fractal tripole arrays.

3.5 Other Types of Miniaturised and Multiband EBG Surfaces

As shown in Fig. 3.27, two extra mechanisms for the miniaturisation of the resonant elements are considered, namely periodic-loaded tripoles and convoluted tripoles. They are arranged on triangular unit cells of the same size as above. The transmission responses of these arrays are presented in Fig. 3.28 and Fig. 3.29. First order resonant frequencies of these designs are found to be lower than that of the tripole array. This indicates that these arrays will have smaller size unit cells if they are working on the frequency point where the tripole array works. Moreover, the multiband resonances of these arrays are also observed.

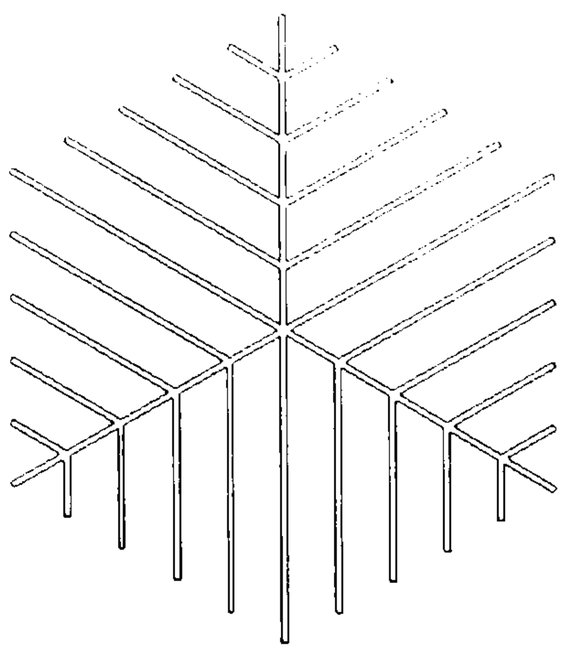

Periodic Loaded Tripole

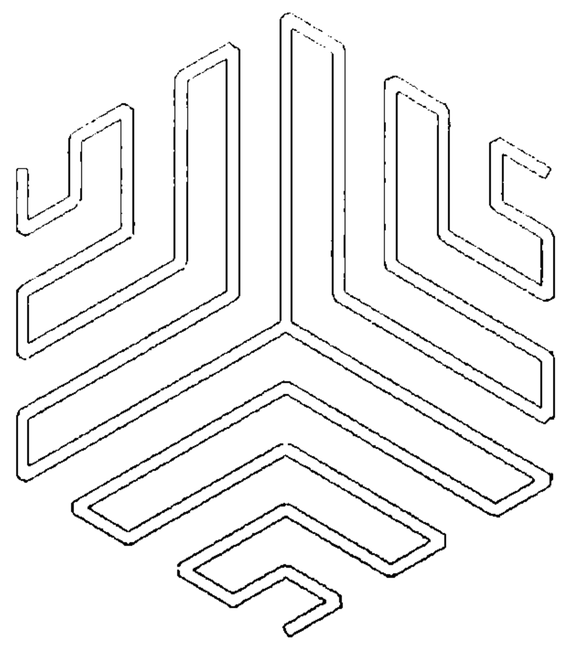

Convoluted Tripole

Fig. 3.27 Geometries of miniaturised elements.

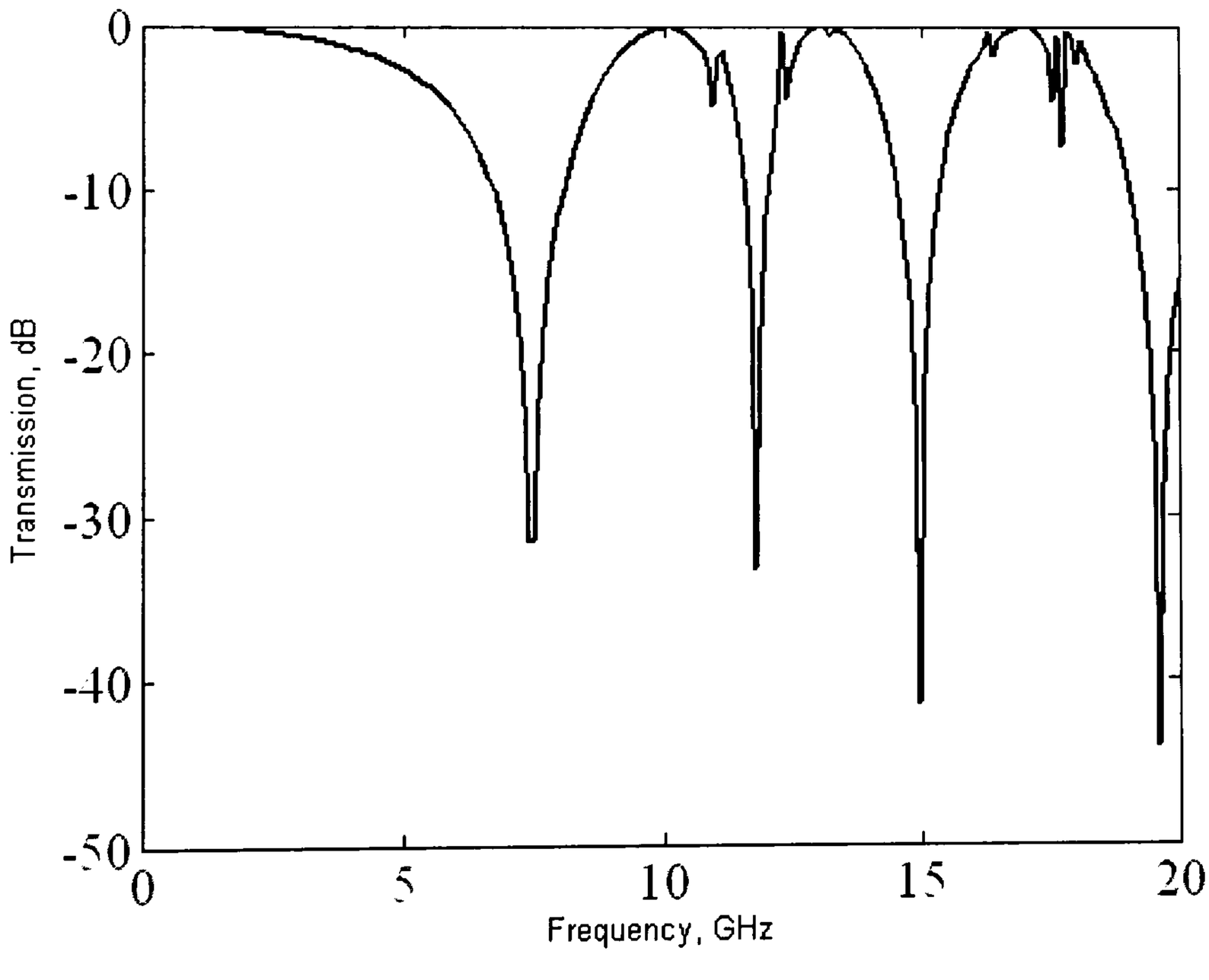

Fig. 3.28 Transmission coefficient of the periodic-loaded tripole array.

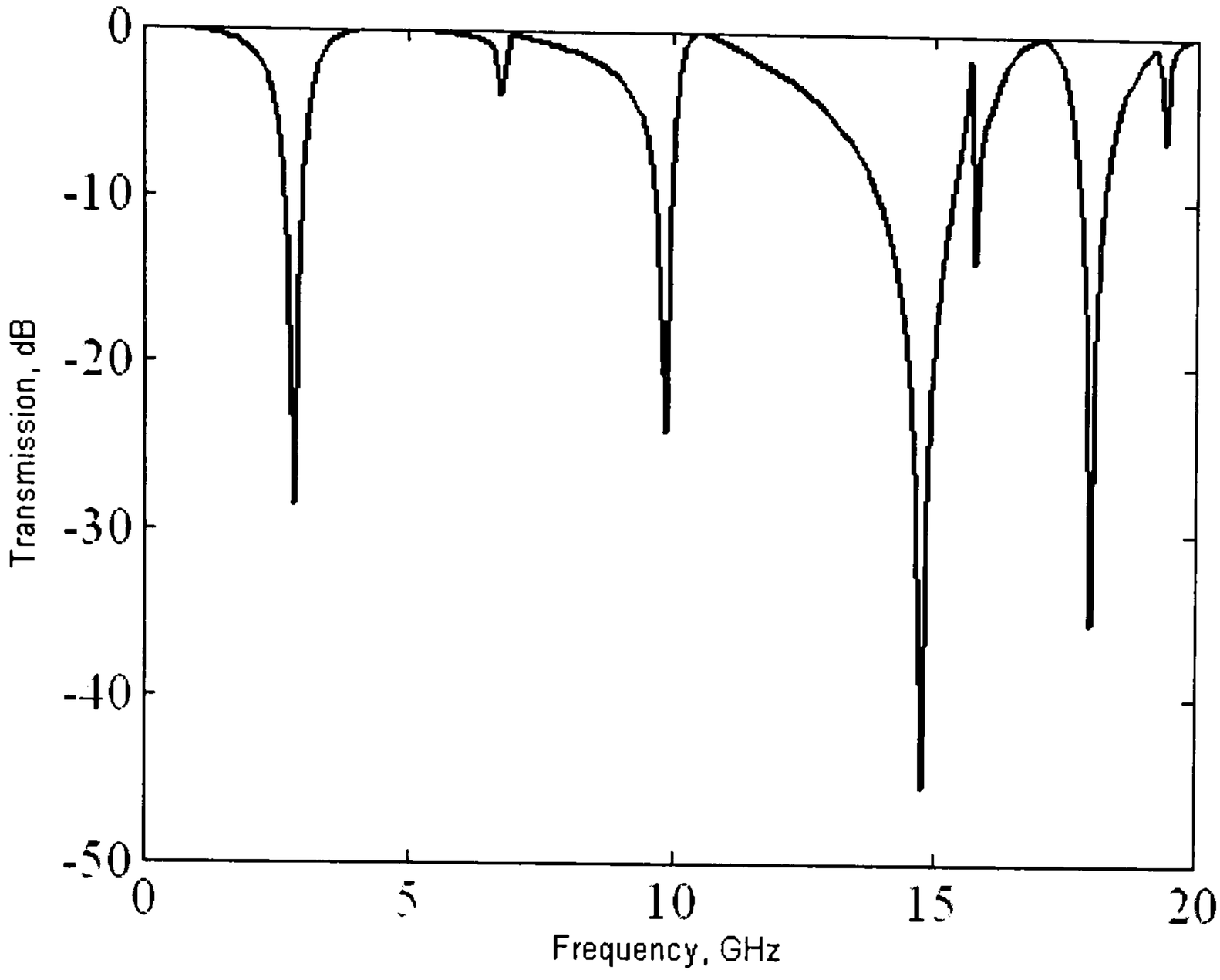

Fig. 3.29 Transmission coefficient of the convoluted tripole array.

3.6 Conclusions

The modelling technique discussed in chapter 2 has been applied in this chapter for the fast and accurate design of miniaturised and multiband EBG and AMC surfaces. Three tripole-based examples namely periodic-loaded tripole, fractal tripole and convoluted tripole arrays are introduced to meet the requirement of miniaturisation and multi-resonance. Fractal tripole arrays have been studied in detail and the accuracy of the numerical technique is investigated with regards to plane wave as well as surface wave dispersion characterisation. A faster and more effective algorithm to derive the dispersion diagram has been proposed in this chapter, which locates the determinant minima by scanning the frequency range instead of scanning the propagation constant (β) range. It has been found that smaller interpolation steps are

required for the accurate calculation of the dispersion diagrams than those required in the plane wave responses. Furthermore, surface currents have been presented and an explanation was given to how miniaturisation can be achieved and how the higher order resonances are generated by adding higher order fractal branches into the original tripole array. Plane-wave responses, surface currents and dispersion diagrams are presented and the computational predictions are verified by comparing with experimental results.

References

[1] P. de Maagt, R. Gonzalo, J. C. Vardaxoglou, and J. M. Baracco, "Electromagnetic Bandgap Antennas and Components For Microwave and (Sub)Millimeter Wave Applications", *Special issue on Metamaterials, IEEE Trans. Antennas Propag.*, Vol. 51, no. 10, pp. 2667-2677, 2003

[2] Y. L. R. Lee, A. Chauraya, D. S. Lockyer, and J. C. Vardaxoglou, "Dipole and Tripole Metallodielectric Photonic Band Gap (MPBG) Structures for Microwave Filter and Antenna Applications", *IEE Proc. Optoelectron.*, Vol. 147, no. 6, pp. 395-400, 2000

[3] A. P. Feresidis, G. Apostolopoulos, N. Serfas, and J. C. Vardaxoglou,, "Closely Coupled Metallodielectric Electromagnetic Band-Gap Structures Formed by Double-Layer Dipole and Tripole Arrays", *IEEE Trans. Antennas Propag.*, Vol. 52, no. 5, pp. 1149-1158, 2004

[4] Y. Rahmat-Samii, and H. Mosallaei, "Electromagnetic Band-gap Structures: Classification, Characterization, and Applications", *Eleventh International Conference on Antennas and Propagation, IEE Conf. Publ.* no. 480, Vol. 1, pp. 560-564, 2001

[5] A. P. Feresidis, and J. C. Vardaxoglou, "High gain planar antenna using optimised partially reflective surfaces", *IEE Proc. Microw. Antennas Propag.* Vol. 148, no. 6, pp. 345-350, 2001

[6] F. Yang, and Y. Rahmat-Samii, "A Low Profile Circularly Polarized Curl Antenna over Electromagnetic Band Gap (EBG) Surface", *Microw. Opt. Technol. Lett.*, Vol. 31, no. 4, pp. 264-267, 2001

[7] F. Yang, and Y. Rahmat-Samii, "Microstrip Antennas Integrated with Electromagnetic Band-Gap (EBG) Structures: A Low Mutual Coupling Design for Array Applications", *IEEE Trans. Antennas Propag.*, Vol. 51, no. 10, pp. 2936-2946, 2003

[8] R. Gonzalo, P. Maaget, and M. Sorolla, "Enhanced Patch Antenna Performance by Suppressing Surface Waves Using Photonic Bandgap Substrates", *IEEE Trans. Microwave Theory Tech.*, Vol. 47, no. 11, pp. 2131-2138, 1999

[9] H. Hsu, M. J. Hill, J. Papapolymerou, and R. W. Ziolkowski, "A Planar X-Band Electromagnetic Band-Gap (EBG) 3-Pole Filter", *IEEE Microwave and Wireless Components Letters*, Vol. 12, no. 7, pp. 255-257, 2002

[10] F. Elek, R. Abhari, and G. V. Eleftheriades, "A Uni-Directional Ring-Slot Antenna Achieved by Using an Electromagnetic Band-Gap Surface", *IEEE Trans. Antennas Propag.*, Vol. 53, no. 1, pp. 181-190, 2005

[11] D. Sievenpiper, L. Zhang, R. F. J. Broas, N. G. Alexopolous, and E. Yablonovitch, "High-Impedance Electromagnetic Surfaces with a Forbidden Frequency Band", *IEEE Trans. Microwave Theory Tech.*, Vol. 47, no. 11, pp. 2059-2074, 1999

[12] S. Wang, A. P. Feresidis, G. Goussetis, and J. C. Vardaxoglou, "Low-Profile Resonant Cavity Antenna with Artificial Magnetic Conductor Ground Plane", *Electron. Lett.*, Vol. 40, no. 7, pp. 405-406, 2004

[13] A. P. Feresidis, G. Goussetis, S. Wang, and J. C. Vardaxoglou, "Artificial Magnetic Conductor Surfaces and Their Application to Low-Profile High-Gain Planar

Antennas", *IEEE Trans. Antennas Propag.*, Vol. 53, no. 1, pp. 209-215, 2005

[14] A. Erentok, P. L. Luljak, and R. W. Ziolkowski, "Characterization of a Volumetric Metamaterial Realization of an Artificial Magnetic Conductor for Antenna Applications", *IEEE Trans. Antennas Propag.*, Vol. 53, no. 1, pp. 160-172, 2005

[15] A. P. Feresidis, G. Apostolopoulos, N. Serfas, and J. C. Vardaxoglou, "Closely Coupled Metallodielectric Electromagnetic Band-Gap Structures Formed By Double-Layer Dipole and Tripole Arrays", *IEEE Trans. Antennas Propag.*, Vol. 52, no. 5, pp. 1149-1158, 2004

[16] J. C. Vardaxoglou, *Frequency Selective Surfaces: Analysis and Design*, Research Studies Press Ltd., Taunton, 1997

4. Analysis and Design of Left-Handed Materials

4.1 Introduction

There has been increased interest in the past few years on composite media (metamaterials) that support left-handed (LH) propagation. They were first theorized by Veselago as double negative (DNG) materials for their simultaneously negative permittivity (ε) and permeability (μ) [1]. The term "left-handed" describes the fact that the vectors **E**, **H** and **k** form a left-handed triplet, instead of a right-handed triplet, as is the case in conventional right-handed (RH) media (Fig. 4.1). Thus, in LH media the Poynting vector $\mathbf{E}\times\mathbf{H}$ (that points at the direction of energy propagation and the group velocity) is anti-parallel to the wave vector **k** (that points at the direction of phase velocity).

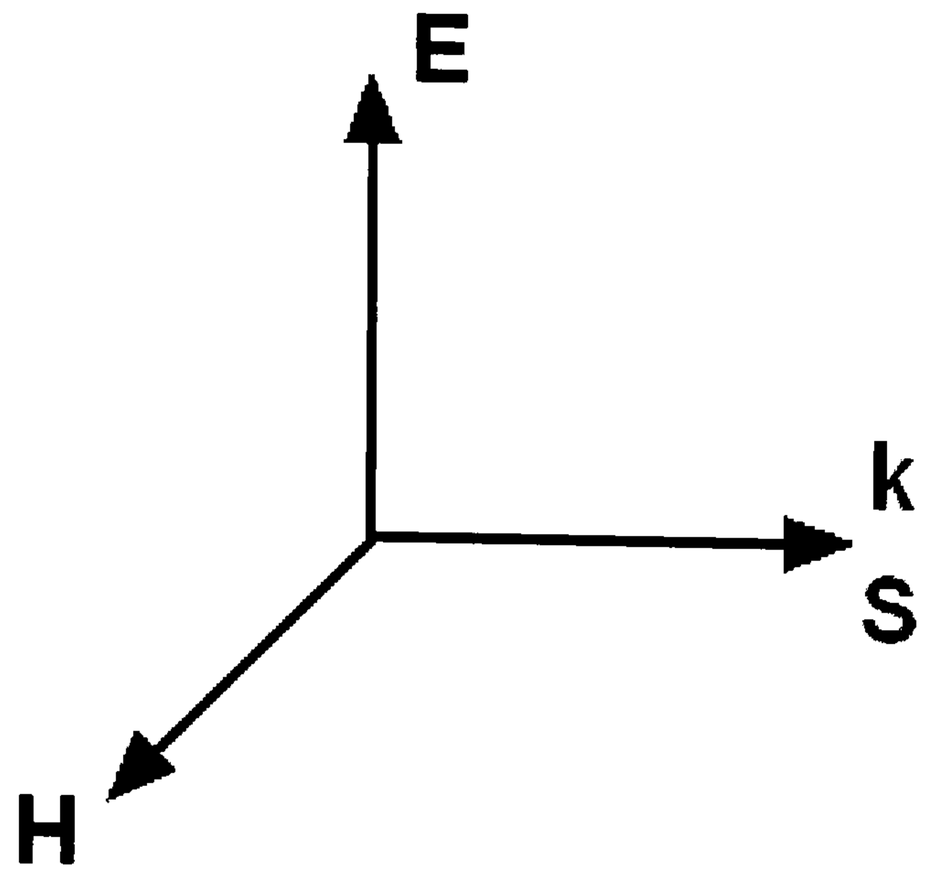

(a)

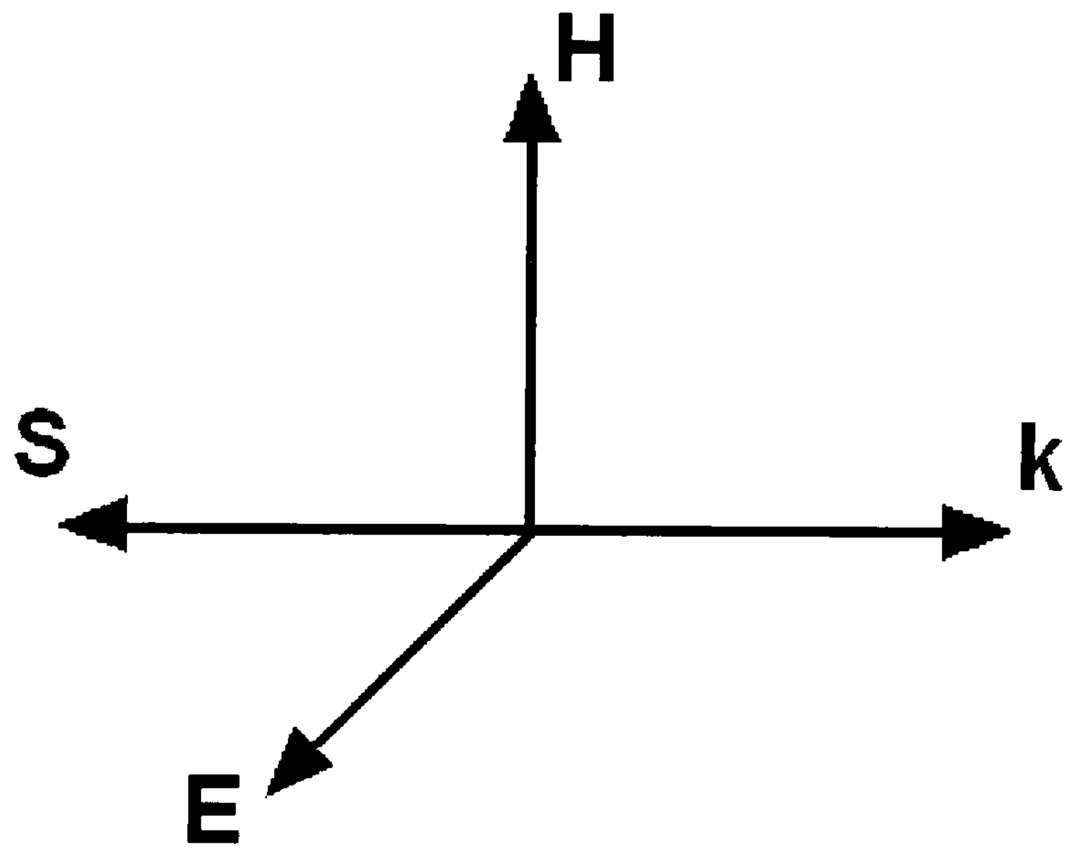

(b)

Fig. 4.1 Wave properties. (a) Right-handed media. (b) Left-handed media.

As a result, unique electromagnetic properties, such as the reversal of Snell's Law and the Doppler Effect, are anticipated with the left-handed materials. The negative refraction and the sub-wavelength focusing phenomenon can be observed inside this type of material as shown in Fig. 4.2 and Fig. 4.3. The lines indicate the directions along which the waves propagate.

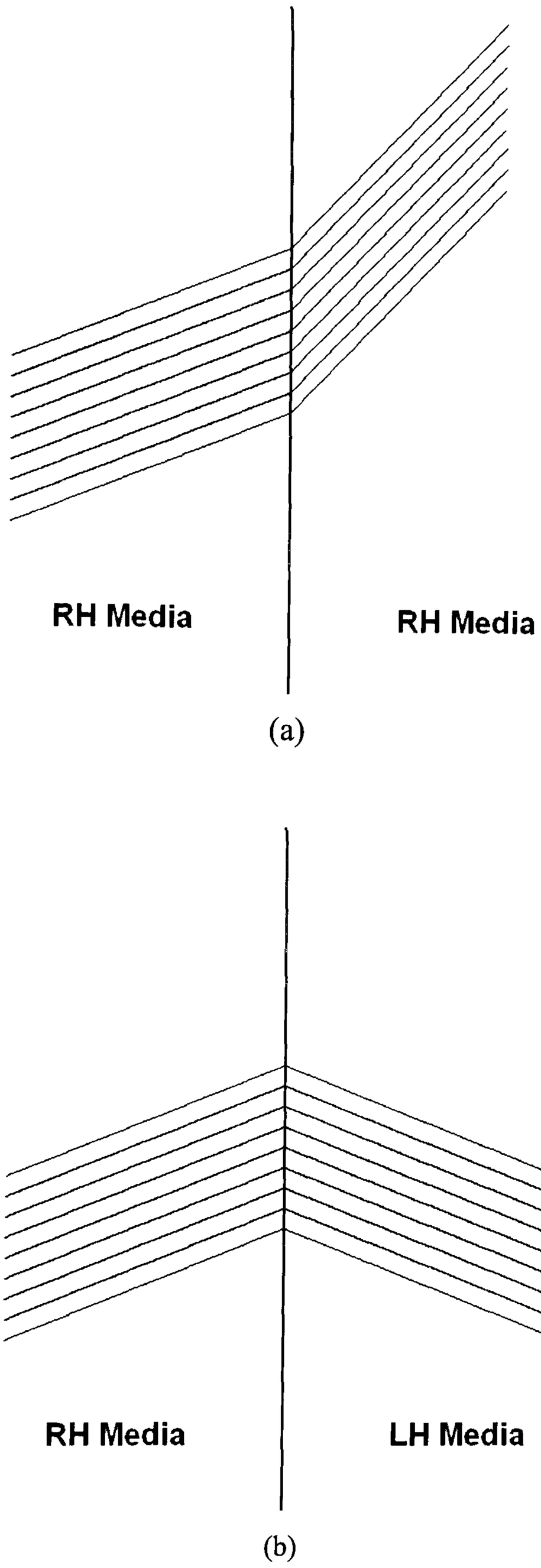

Fig. 4.2 Wave refraction. (a) Right-handed media. (b) Left-handed media.

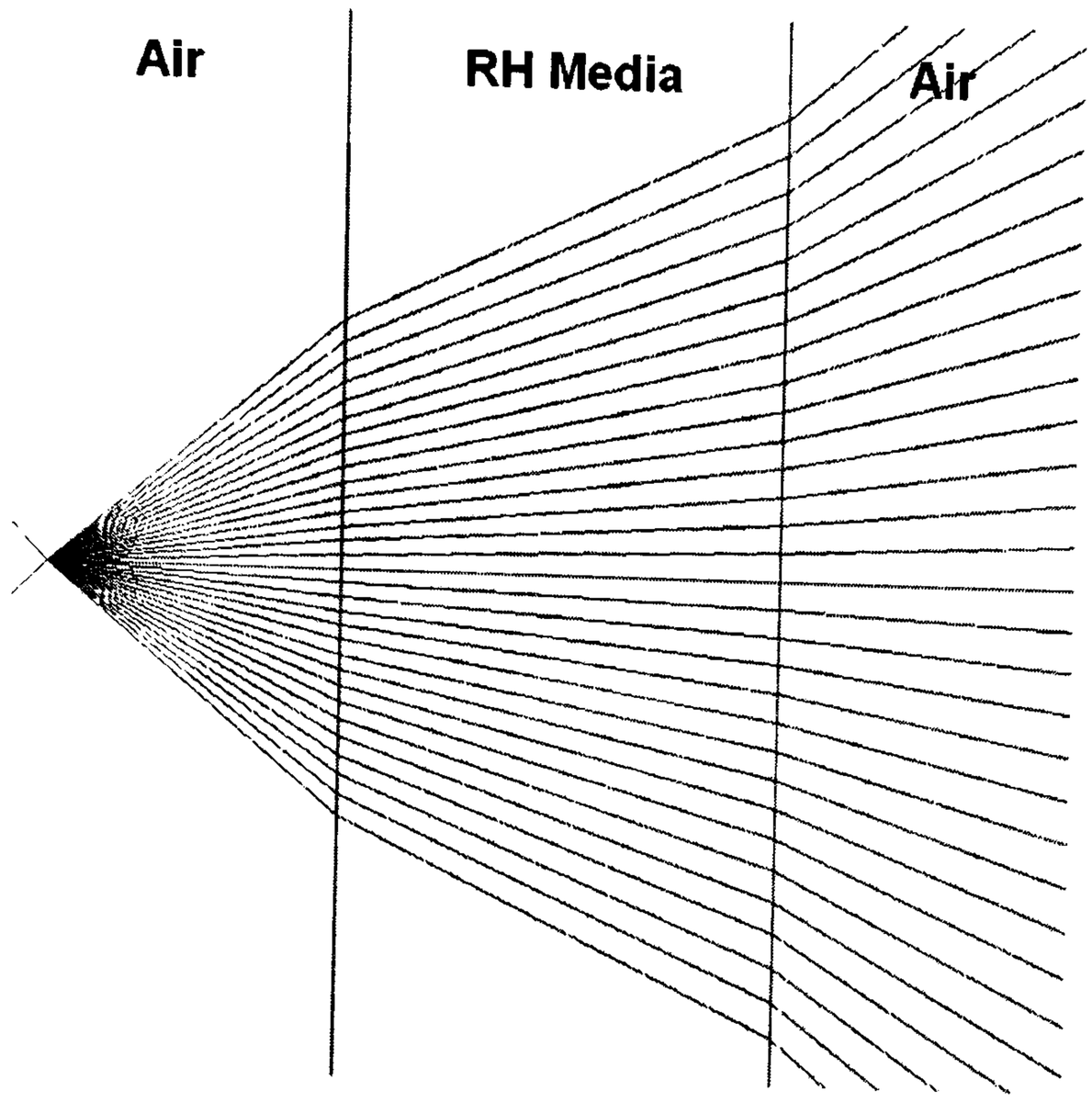

(a)

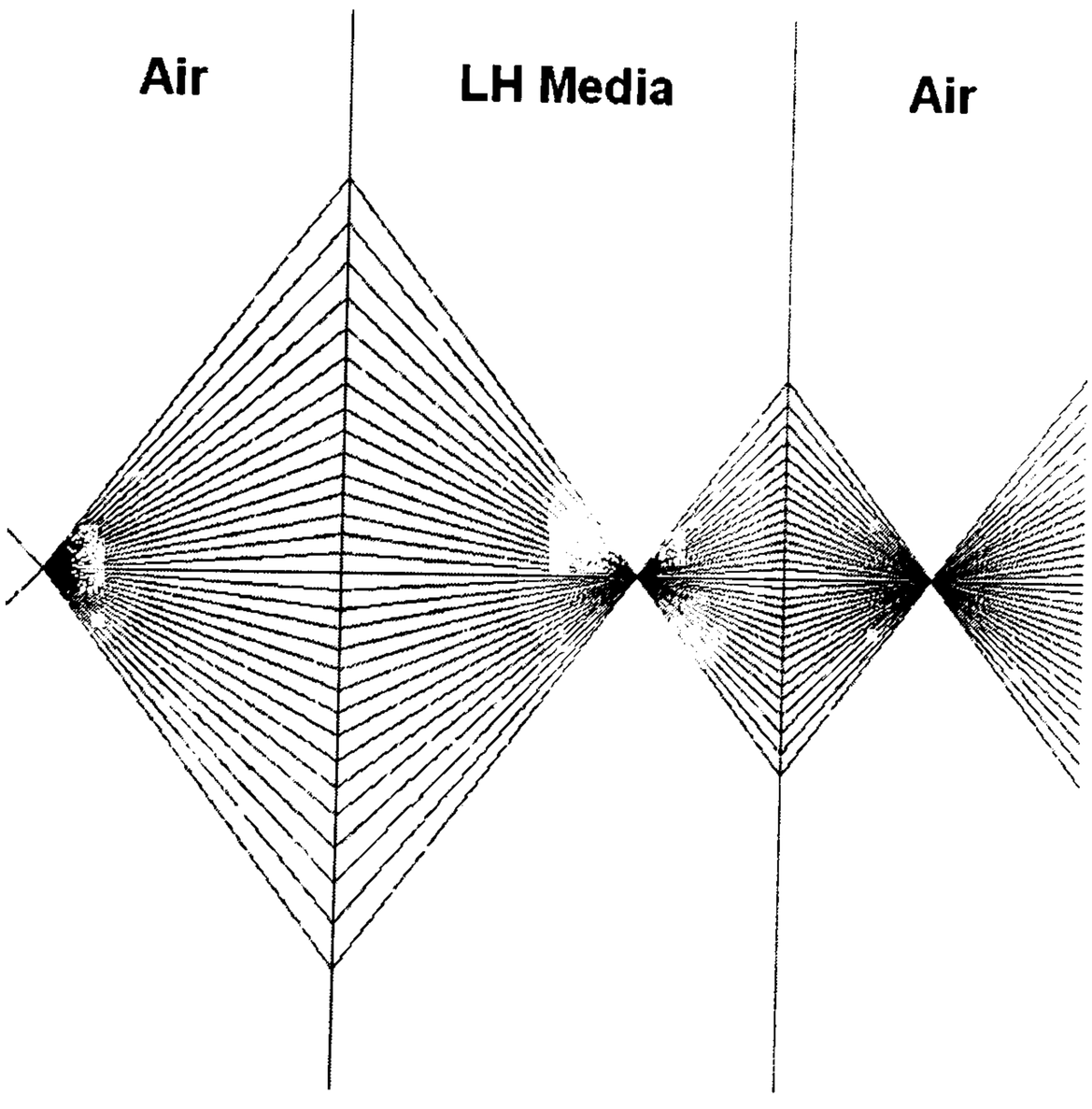

(b)

Fig. 4.3 Sub-wavelength focusing of waves. (a) Right-handed media. (b) Left-handed media.

Recently, artificial LH media have been synthesized and their unusual properties of negative refraction and sub-wavelength focusing have been experimentally demonstrated [2]-[14]. These LH materials possess a negative effective refractive index n (NRI) related to the phase velocity according to

$$v_p = \frac{\omega}{\beta} = \frac{c}{n} \tag{4.1}$$

where v_p is the phase velocity, ω is the frequency and β is the propagation constant. For NRI metamaterials, the dispersion relation of the first order mode has negative gradient. This indicates that the phase velocity $\left(v_p = \omega/\beta\right)$ and the group velocity $\left(v_g = \partial\omega/\partial\beta\right)$ are anti-parallel.

4.2 Transmission Line Concept

A brief outline of the dual transmission line (TL) concept for LH media is given here in order to explain its relation to the modal **E** and **H** fields that are studied in chapter 4.3. As has been shown recently, a periodic structure with a unit cell that can be described by the equivalent circuit of Fig. 4.4(c) exhibits LH properties, i.e. antiparallel group and phase velocities, and negative index of refraction [4]-[6]. The LH nature is provided by the series capacitors and the shunt inductor, as opposed to the series inductors and the shunt capacitor of the conventional RH-TL in Fig. 4.4(b).

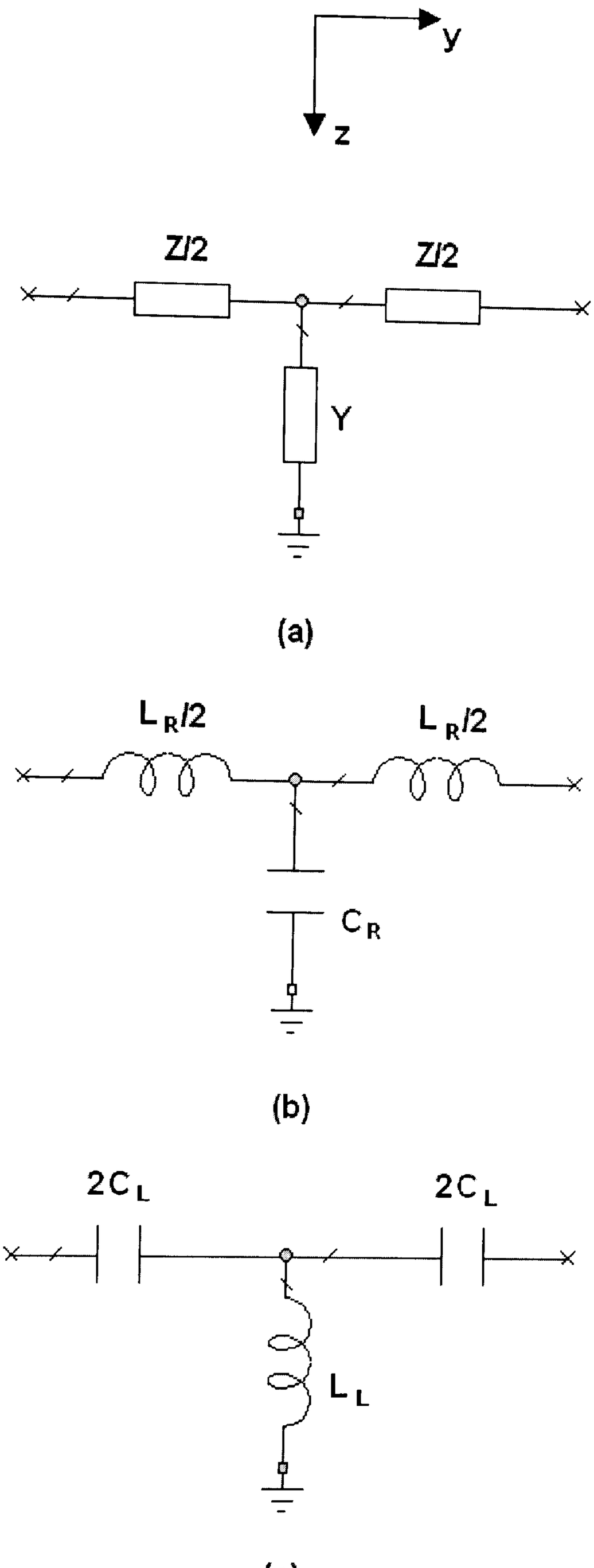

Fig. 4.4 Equivalent modal circuits. (a) General TL. (b) RH-TL. (c) LH-TL.

The propagation constant of a general TL in Fig. 4.4(a) is given by

$$\gamma = \alpha + j\beta = \sqrt{ZY} \tag{4.2}$$

where Z and Y are the impedance and admittance per unit cell. In the RH-TL case of Fig. 4.4(b)

$$Z = j\omega L_R \tag{4.3}$$

$$Y = j\omega C_R \tag{4.4}$$

and in the LH-TL case of Fig. 4.4(c)

$$Z = -\frac{1}{j\omega C_L} \tag{4.5}$$

$$Y = -\frac{1}{j\omega L_L} \tag{4.6}$$

In the frequency range where β is purely real, propagation occurs since $\gamma = j\beta$. Therefore, the dispersion relation for a homogeneous TL is

$$\beta = \begin{cases} \sqrt{-ZY} = \omega\sqrt{L_R C_R}, & \text{RH-TL} \\ -\sqrt{-ZY} = -\dfrac{1}{\omega\sqrt{L_L C_L}}, & \text{LH-TL} \end{cases} \tag{4.7}$$

$$v_p = \frac{\omega}{\beta} = \begin{cases} \dfrac{1}{\sqrt{L_R C_R}}, & \text{RH-TL} \\ -\omega^2 \sqrt{L_L C_L}, & \text{LH-TL} \end{cases} \tag{4.8}$$

and

$$n = \frac{c}{v_p} = \begin{cases} \dfrac{\sqrt{L_R C_R}}{\sqrt{\mu_0 \varepsilon_0}}, & \text{RH-TL} \\ -\dfrac{1}{\omega^2 \sqrt{L_L C_L}\sqrt{\mu_0 \varepsilon_0}}, & \text{LH-TL} \end{cases} \tag{4.9}$$

Based on this approach, it is instructive to study the distribution of the electric and magnetic field in the unit cell taking into account the requirement for shunt inductance and series capacitance. Shunt inductance is related to the magnetic field that would be produced by an ideal shunt inductor, i.e. the z-component of the magnetic field (H_z). Similarly, a series capacitor would produce electric field along the y-axis (assuming that E-field is parallel to the y-axis and therefore "voltage is applied" along y). The y-component of the electric field (E_y) is therefore a measure of the equivalent series capacitance. The distributions of H_z and E_y for the first resonant mode of the proposed arrays are presented and discussed in the following section.

4.3 Planar Left-Handed Materials

Planar distributed LH structures, which are compatible with photolithographic techniques, have been presented in [4]-[6]. The distributed planar NRI structures proposed thus far require either grounding vias or elements embedded vertically in a planar grounded dielectric substrate, which can be applied in microwave circuit and antenna designs [15]-[26]. In this section, novel planar left-handed metamaterials are proposed. Variations of the split rectangular loop element printed on grounded dielectric substrate are demonstrated to exhibit left-handed propagation properties. In order to explain their performance, the modal field distribution of the unit cell is studied in conjunction with the emerging dispersion relation. In conducting this study, emphasis is given to the distributions of the **E** and **H** fields and how they satisfy the requirement of LH media for shunt inductance and series capacitance. The proposed structures are simple to fabricate and are scalable to higher frequencies [27]. Similar element geometry for LH metamaterials has been introduced by Erentok et. al. [28]. However, the proposed structure in [28] is stratified volumetric arrays for plane-wave applications, and our structures given here are planar structures working with surface waves.

The techniques described in chapter 2 are evaluated and applied in order to model the dispersion characteristics and modal fields of planar left-handed metamaterials. An initial investigation has shown that moving from the square split loop element to the rectangular split loop the first resonant mode changes from right-handed to left-handed. Therefore the study is focused on a rectangular unit cell with an edge ratio of 2:1. The investigation presented here includes a closed rectangular loop, a split rectangular loop and two variations of the split loop that increase magnetic and electric effects according to the dual transmission line concept for left-handed media.

The arrays are placed on grounded dielectric substrate. The dispersion properties of all four planar arrays are presented. The dispersion results presented have been verified with commercial software Ansoft HFSS [29] throughout this section. Finally, an isotropic design is also presented.

4.3.1 Dispersion Characteristics

The unit cells of the arrays discussed hereafter are shown in Fig. 4.5. Fig. 4.5 shows the unit element of (b) a split rectangular loop, (c) a capacitive-loaded split rectangular loop and (d) a spiral-loaded rectangular loop arrays. For completeness, the closed rectangular loop (Fig. 4.5(a)) is also discussed. The unit cell is kept constant throughout (3mm× 6mm). All metallic line widths are 0.2mm and the gaps in the split loop variations are s=0.2mm, t=0.4mm, in order to be compatible with conventional photolithographic techniques. The element dimensions are L=5.8mm and W=2.8mm. The grounded dielectric substrate has a dielectric constant of 2.2 and thickness 1.13mm.

In order to validate the application of the interpolation technique, the elements of the Z matrix have been calculated for a range of frequency points and element geometries. As an example the values of a random Z_{ji} element are shown in Fig. 4.6 for the array with unit element depicted in Fig. 4.5(d). It is evident that the Z matrix element values, both real and imaginary, vary smoothly and regularly with frequency. This allows for the implementation of the interpolation technique described in chapter 2. Similar with what has been discussed in chapter 3, both variations of real part and imaginary part of Z_{ji} versus frequency have the inversion function form. Therefore, both parts of Z_{ji} are interpolated using the inversion functions as

$$R(f) = A^R / f + B^R f + C^R \tag{4.10}$$

$$I(f) = A^I / f + B^I f + C^I . \tag{4.11}$$

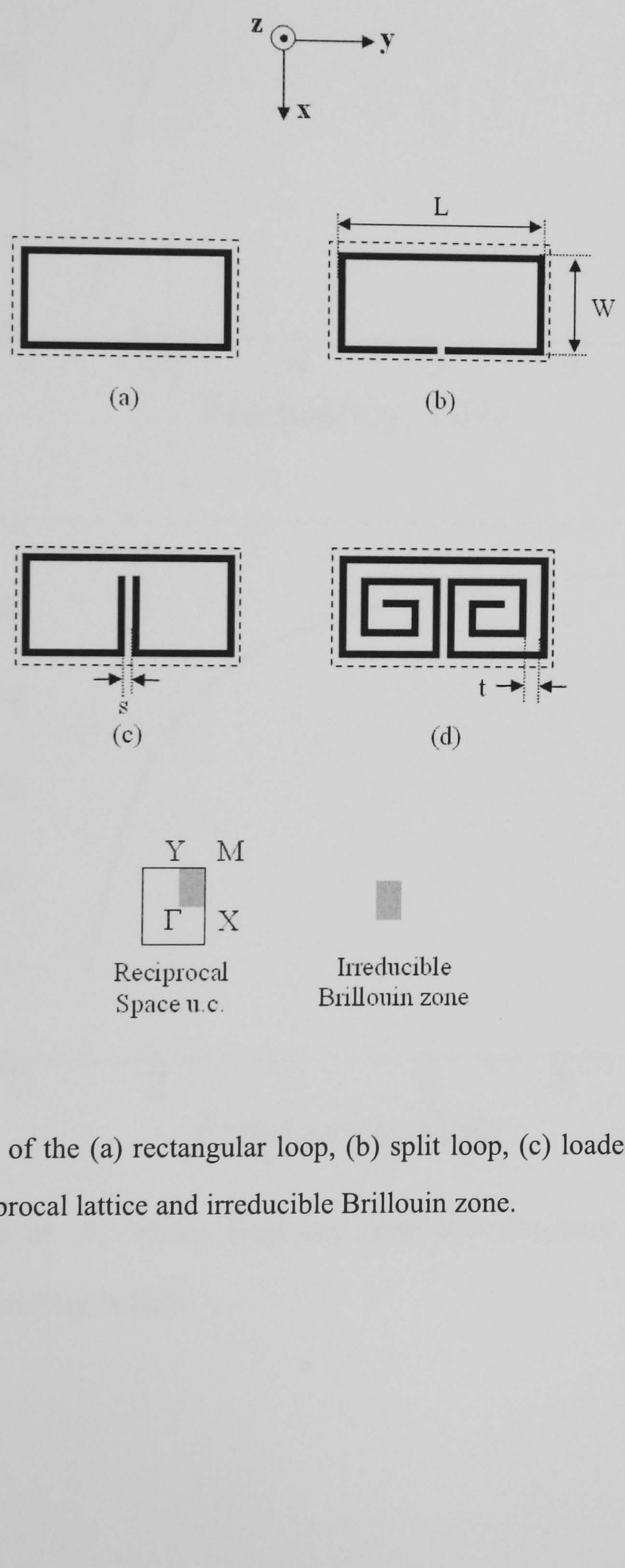

Fig. 4.5 Unit cells of the (a) rectangular loop, (b) split loop, (c) loaded loop and (d) spiral loop (e) reciprocal lattice and irreducible Brillouin zone.

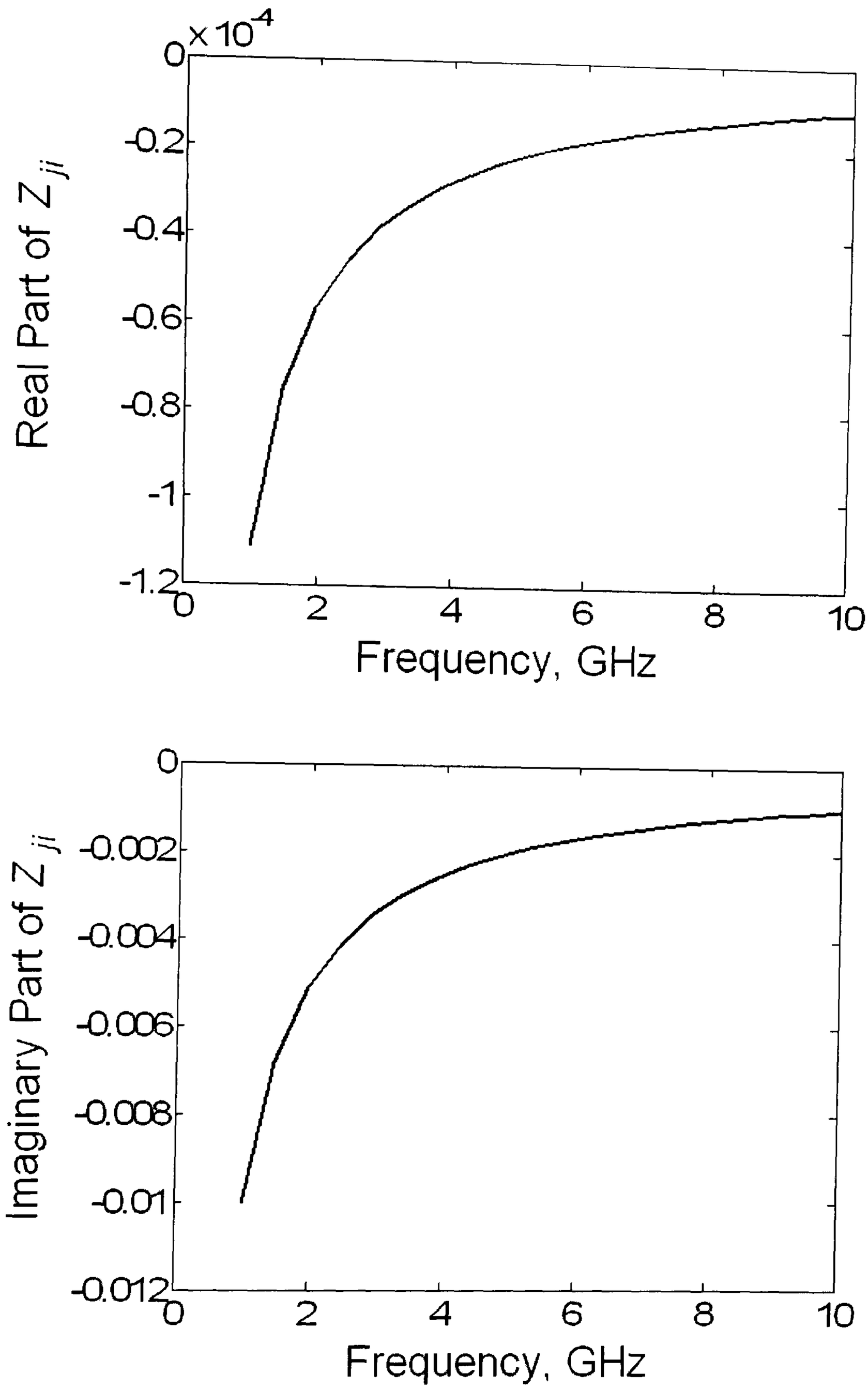

Fig. 4.6 Variation of Z_{ji} versus frequency (real and imaginary part) for the spiral-loaded element (Fig. 4.5(d)).

The simulations showed that large interpolation steps have not produced successful results for the dispersion characterisation of metallodielectric arrays. We, thus, performed a detailed study of the effect of the interpolation step on the accuracy of the dispersion results. The range of frequencies was broken down to smaller sections where interpolation was applied. An error value defined as the difference between the spectral positions of a minimum of Z with and without interpolation has been calculated for different interpolation steps. Initially we have used the quadratic (2.78) and inverse (2.79) functions for the real and imaginary parts of the Z-matrix elements respectively (referred to as Qd). Subsequently, we used (4.10) and (4.11) as the interpolation function for both real and imaginary parts (referred to as Inv). Fig. 4.7 shows the percentage error of the phase constant for different frequencies and interpolation steps for the element depicted in Fig. 4.5(d). It is evident that the inverse function approximates better both real and imaginary parts. For an interpolation step equal to 1 GHz the error becomes substantially small, well below 1%, which corresponds to a relatively good accuracy of the final result. Based on this study, an interpolation step of 1GHz and only the inverse interpolation function has been used to produce the dispersion diagrams. For higher values of dielectric constant, corresponding to typical commercially available PCB substrates, similar accuracy can be achieved with the same interpolation step.

In order to demonstrate the acceleration achieved by the proposed technique for band-gap characterisation, Fig. 4.8 shows a typical variation of the determinant of the impedance matrix with frequency. The zero of the determinant, which is the solution that we want to identify, corresponds to the sharp minimum at 4.31GHz. As shown in the inset graph, in order to have 1% accuracy in determining this value, the step for producing a graph such as the one shown in Fig. 4.8 would require about 100 frequency points in the range of 4.2GHz to 4.4GHz. Employing the interpolation

technique, we can produce the same number of points with the computational cost of only 3 frequency points. The time required for each matrix generation using interpolation together with the calculation of the determinant is negligible compared to the time required to generate the matrix without interpolation. Hence the interpolation technique accelerates the computations by about 30 times.

Following the evaluation of the interpolation scheme, the dispersion characteristics of the elements depicted in Fig. 4.5 can now be calculated by locating the zeros of the impedance matrix Z in the β-f space, as discussed in the previous section. By varying β_x and β_y along the boundary of the irreducible Brillouin zone, a number of frequency sweeps are carried out. All the corresponding determinants of Z are calculated and plotted versus frequency for different values of β_x and β_y. From the determinant plots, zeros are identified as sharp minima. The dispersion relation of the first resonant mode of these arrays is shown in Fig. 4.9, where the light line is also shown.

From the dispersion relation, we can readily calculate the equivalent refractive index n according to

$$n = c \cdot \frac{\beta}{\omega} \tag{4.12}$$

where c is the speed of light and ω/β the phase velocity of the mode. Fig. 4.10 shows the refractive index for the loaded split-loop and the spiral split-loop as calculated from the dispersion relation of Fig. 4.9.

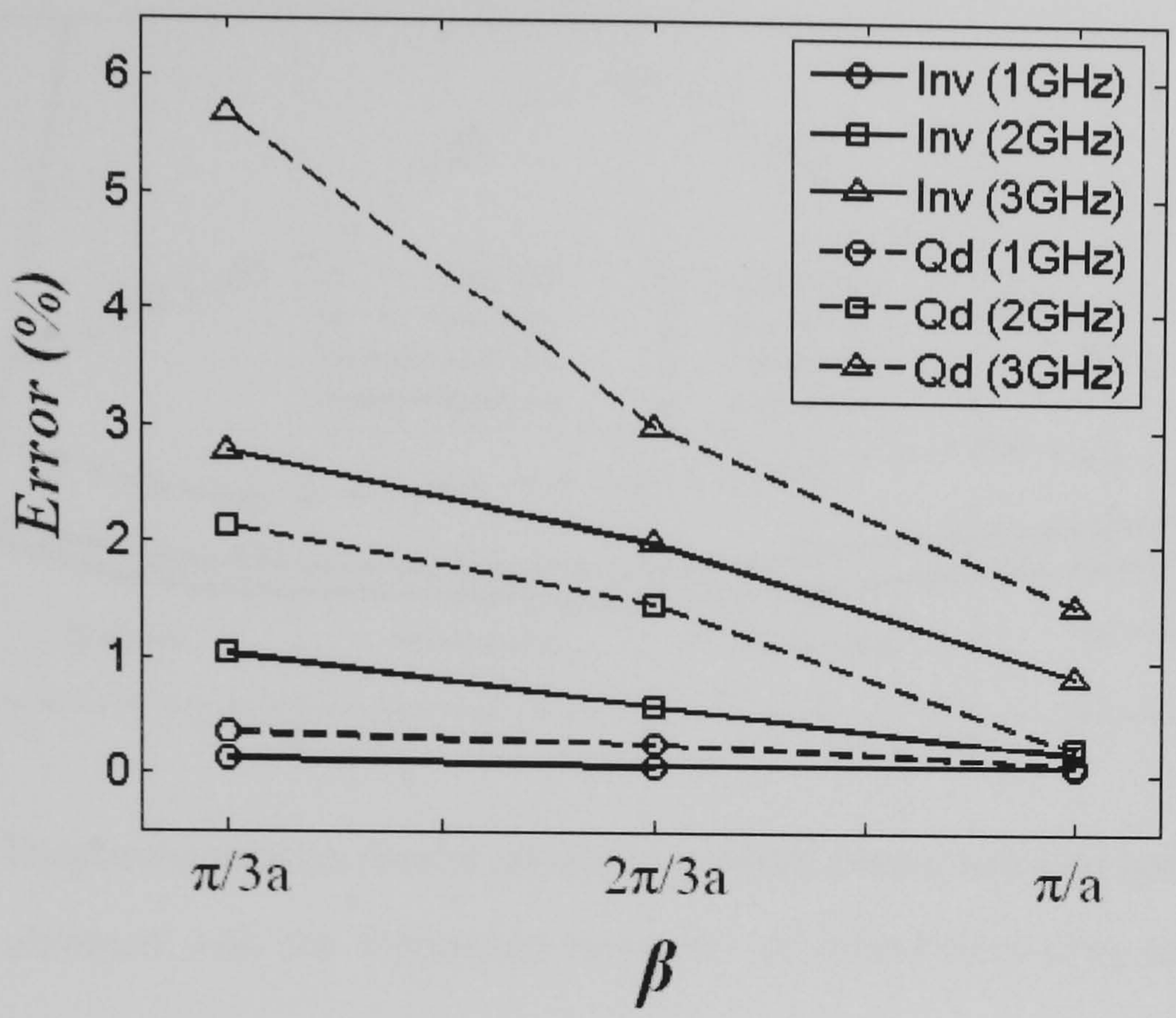

Fig. 4.7 Error (%) in calculated roots of the determinant of *Z* matrix due to the application of the interpolation technique with different interpolation steps and interpolation functions.

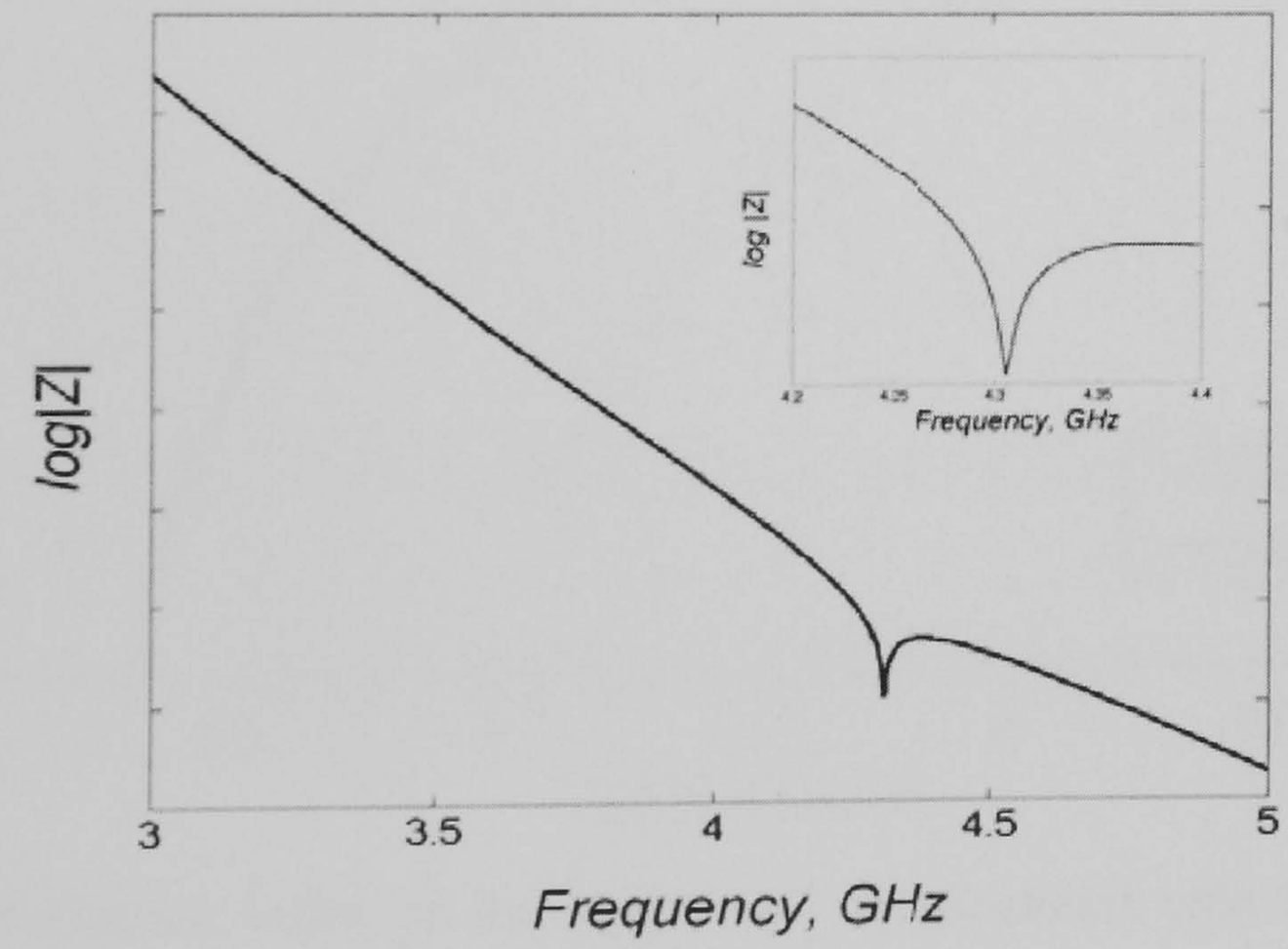

Fig. 4.8 Determinant of impedance matrix with frequency; a close-up of the root (sharp minimum) is shown as inset.

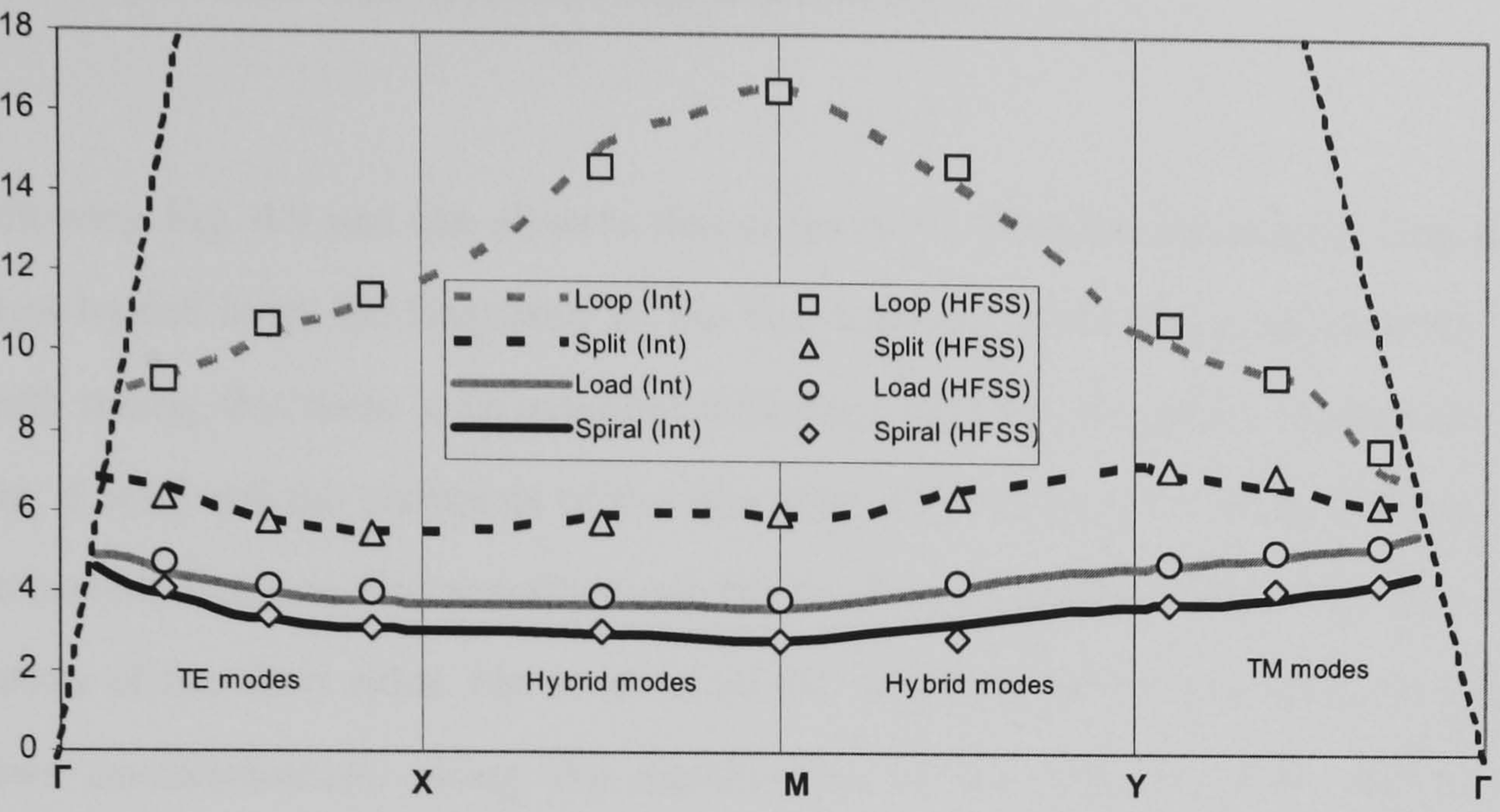

Fig. 4.9 Dispersion relation for the grounded periodic arrays with elements in Fig. 4.5. Results obtained with the theoretical technique presented here (Int) and also with HFSS.

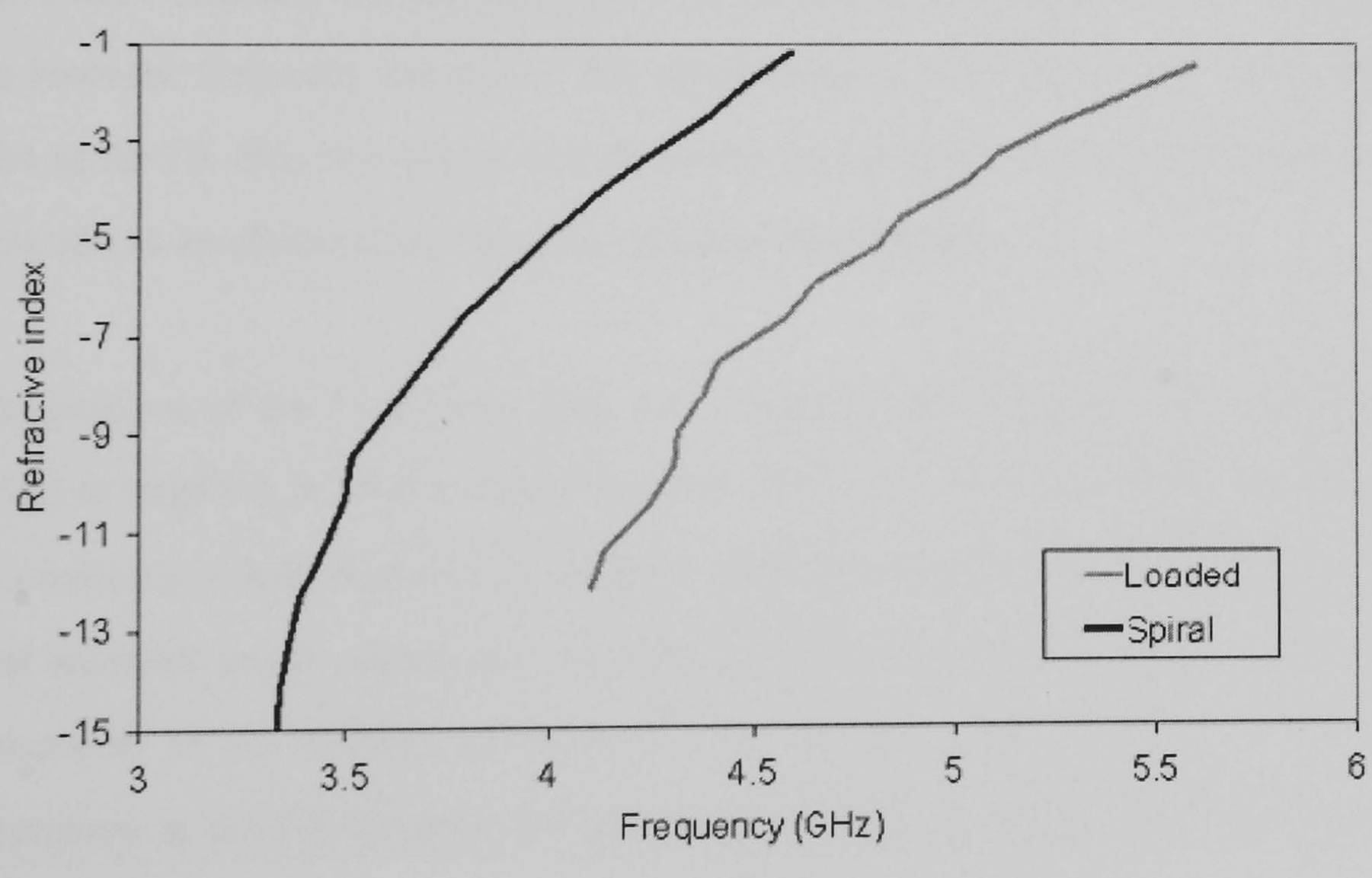

Fig. 4.10 Refractive index of the loaded and spiral-loaded split loop structures calculated from the dispersion diagram.

4.3.2 Dispersion Properties and Field Distributions

Following Fig. 4.9 one can observe that as we move from the rectangular loop to the spiral-loaded loop, the frequency of the first resonant mode drops significantly. It is worth noting that there is an essential difference between the closed rectangular loop (Fig. 4.5(a)) and the variations of the split loop (Fig 4.5(b), (c), (d)). In the first case, the current flows co-directionally along the two longer parallel sides, with zeros at the centres of the short sides. However in all the variations of the split loop, the current flows co-directionally along the metalisation of the elements from end to end, resulting in longer electrical length. This in turn results in lower frequency of the first resonant mode. Among the elements of Fig 4.5(b) – (d), we can attribute the reduction of the resonant frequency to the increase of the resonant length of the element. Alternatively, in an equivalent circuit model of the structure, the capacitance between end-loaded elements and the inductance (in the case of the spiral) increase and hence the resonant frequency decreases. The spiral element array has a unit cell of about $\lambda/24$ in the ΓX direction, where λ is the centre wavelength of the first resonant mode. This allows an effective medium description of the structure.

The gradient of the f - β curve (Fig. 4.9) changes from positive in the case of Fig. 4.5(a) to negative in all the remaining cases of Fig. 4.5. As discussed in section 4.1, this indicates a left-handed (LH) medium when homogeneousness is permitted . The first resonant mode corresponds to electric field polarisation parallel to the larger dimension of the element and aligned with the gap in the split loop variations. Therefore, in the ΓX direction the first resonant mode is a predominantly TE and in the ΓY direction the first mode is predominantly TM. In the XM and MY sections of the Brillouin contour the modes are hybrid. The bandwidth of the LH mode can be determined from the dispersion diagram. It is worth noting however that as we move

away from the light line towards increasing propagation constant and decreasing frequency, the effective refractive index increases significantly. This makes it harder to couple energy in the negative mode from free space (or a RH medium with small value of n).

Following the dual transmission line concept for LH media, it is instructive to study the distribution of the electric and magnetic field in the unit cell taking into account the requirement for shunt inductance and series capacitance. Shunt inductance is related to the magnetic field that would be produced by an ideal shunt inductor, i.e. the z-component of the magnetic field (H_z). Similarly, a series capacitor would produce electric field along the y-axis (E-field is parallel to the y-axis and therefore "voltage is applied" along y). The y-component of the electric field (E_y) is therefore a measure of the equivalent series capacitance. The distributions of H_z and E_y for the first resonant mode of the arrays studied in this section are shown in Fig. 4.11.

As mentioned earlier, the current in the closed rectangular loop flow in parallel on the two long edges with a zero at the middle of each shorter edge. Therefore opposite charges accumulate on closely spaced short sides of successive elements, resulting in an equivalent capacitance between the edges of successive elements (Fig. 4.11(a)). The currents on the two long edges create magnetic field components along the z axis, which corresponds to shunt inductance (Fig. 4.11(e)). However, both series capacitance and shunt inductance are weak and the structure supports a RH mode.

The situation is different in the case of the split loop and its variations. Additional capacitance emerges in the gap, where opposite charges gather on either side (Fig. 4.11(b)). Furthermore, the current now circulates along the open loop resulting in stronger magnetic fields that also appear along the short edges (Fig. 4.11(f)). The

structure at the first resonant mode is therefore LH for the TE mode propagating in the ΓX direction. However, it is still positive for the TM modes that propagate in the ΓY. This is attributed to the fact that the polarisation of the electric and magnetic field components of TM modes result in a weaker excitation of currents on the loops, as has been readily observed in corresponding field plots obtained from our simulations.

Further enhancement of the series capacitance is obtained for the loaded split loop (Fig. 4.5(c)). In this topology we have introduced larger re-entrant faces where opposite charges accumulate and the capacitance values are increased. This is indeed confirmed by the field distribution of Fig. 4.11(c). Furthermore, current now also flows along the re-entering loads, with results in further increase of H_z (Fig. 4.11(g)). The structure is more miniature and supports LH propagation in both directions.

In order to further enhance the LH effect, we extend the capacitive loads to spirals. The flow of current on the spirals acts as a planar inductor and thus increases the magnetic field H_z. This is indeed confirmed in Fig. 4.11(h). In addition, stronger electric fields in the gap and hence higher series capacitance are also obtained (Fig. 4.11(d)). The structure supports LH propagation throughout the Brillouin zone, and the bandwidth of the LH mode is now wider as compared to the previous geometries.

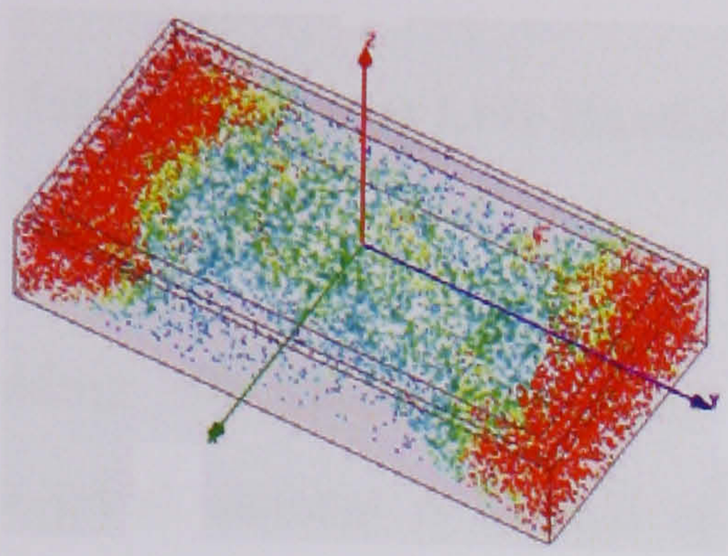

(a)

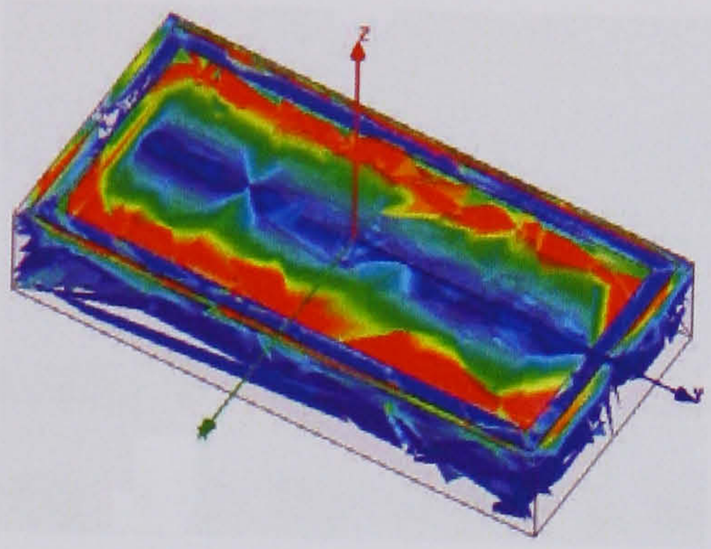

(e)

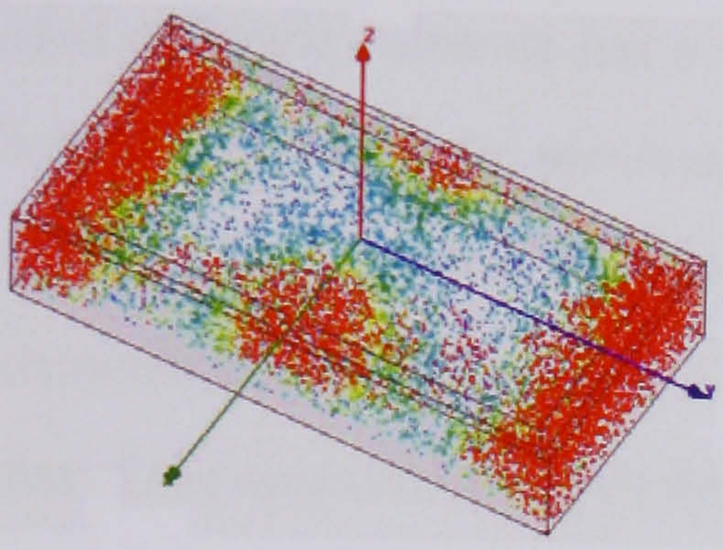

(b)

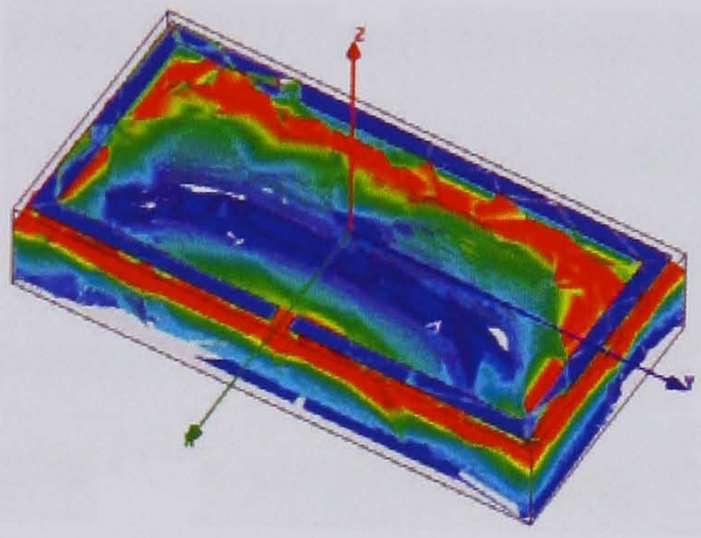

(f)

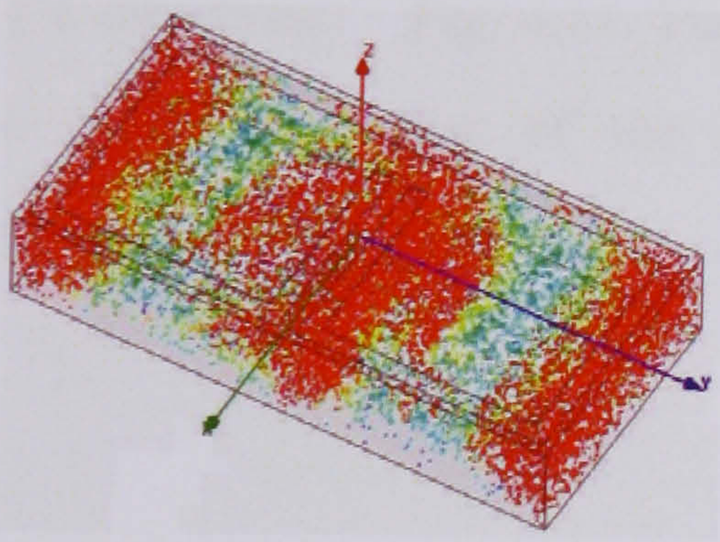

(c)

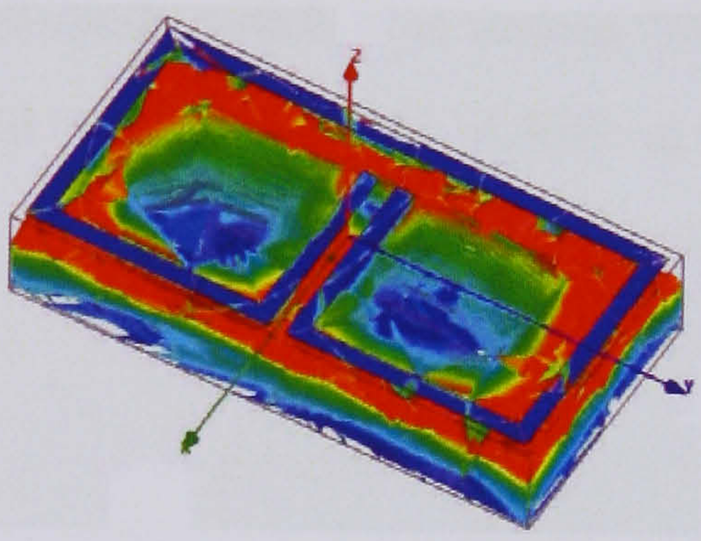

(g)

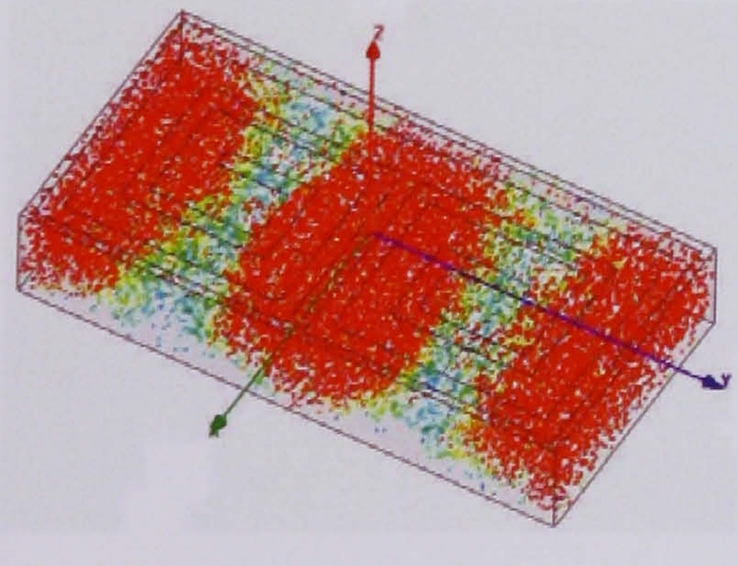

(d)

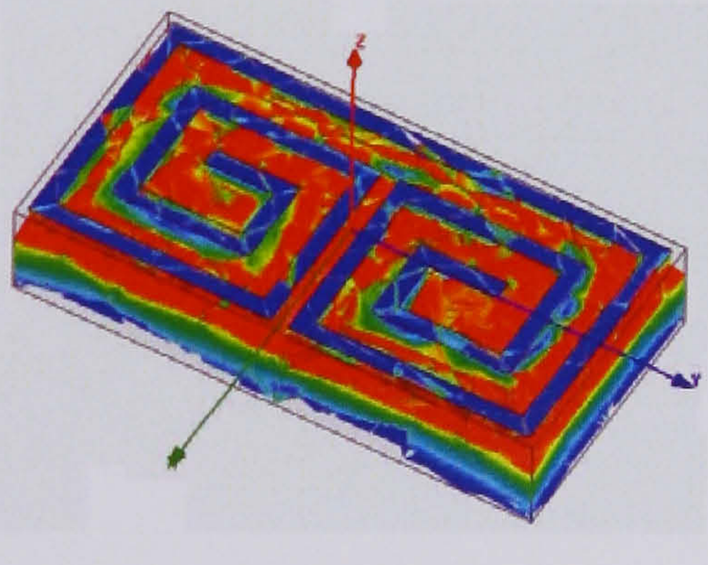

(h)

Fig. 4.11 Normalized values of the E_y component (a-d) and the H_z component (e-f)

of the loop, split-loop, loaded split-loop, spiral split-loop element arrays at the first resonant mode in the ΓX.

4.3.3 Isotropic Planar Left-Handed Materials

Extending the element geometry in Fig. 4.5(d), a more isotropic design of single-spiral element is studied as shown in Fig. 4.12. The element is laid in a 2.2mm× 2.2mm square unit cell. All metallic line widths and gaps are 0.2mm. The grounded dielectric substrate has a dielectric constant of 2.2 and thickness 1.13mm, which is the same with the previous designs. According to the LH-TL model in Fig. 4.4(b), the series capacitors correspond here to the gaps between two adjacent lines and elements instead of the gaps inside the elements of Fig. 4.5(d). The dispersion diagram of the structure and the effective refractive index are plotted in Fig. 4.13 and Fig. 4.14. The isotropy is demonstrated by comparing the refractive indices along ΓX and ΓY directions in Fig. 4.14. The left-handed mode which is at around 10GHz is much higher than that of the double-spiral design in Fig. 4.5(d) at 4GHz approximately.

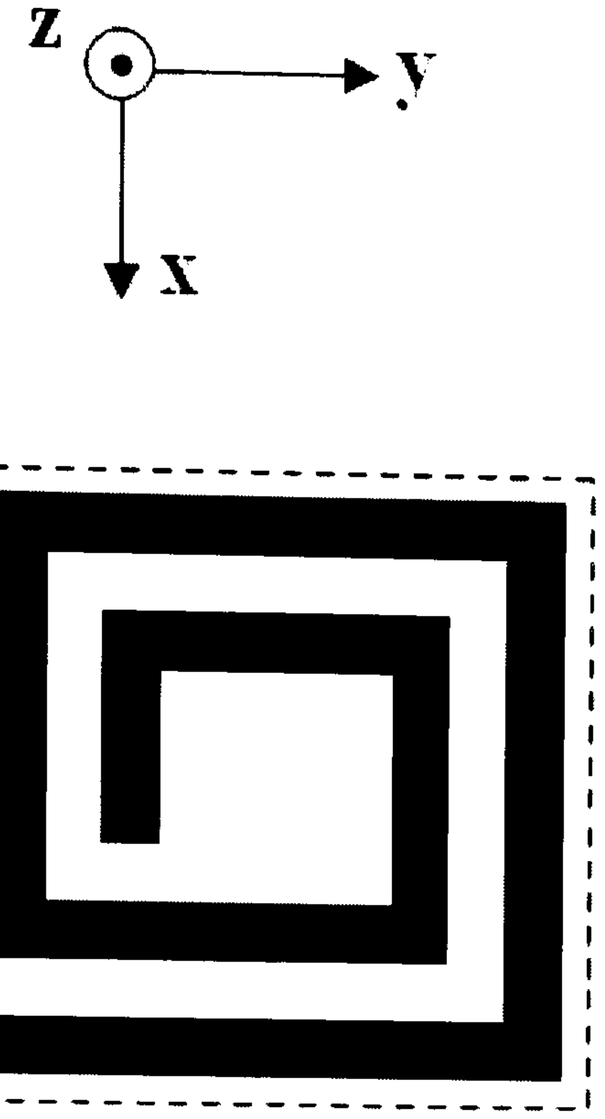

Fig. 4.12 Unit cell of isotropic spiral element.

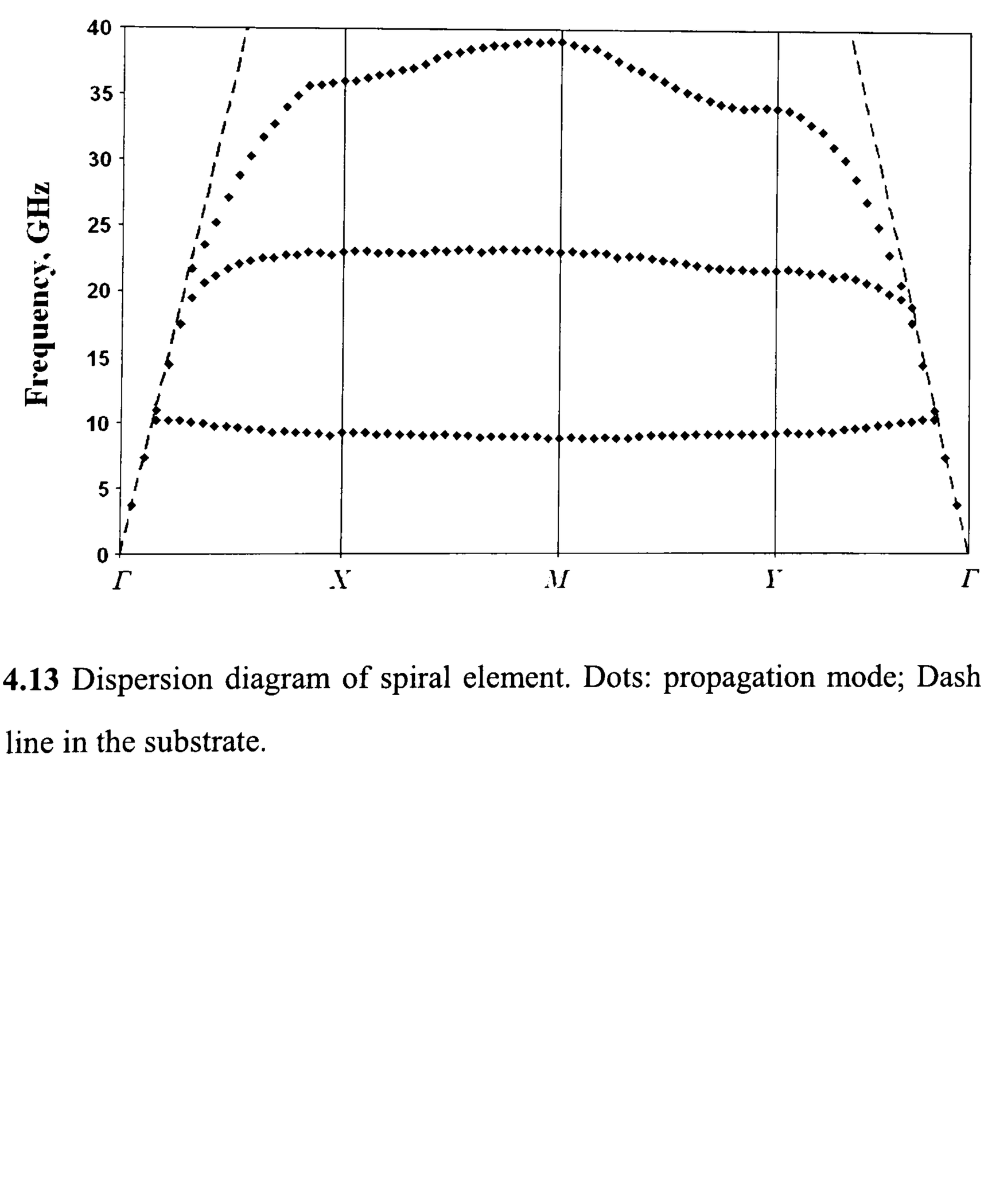

Fig. 4.13 Dispersion diagram of spiral element. Dots: propagation mode; Dash line: light line in the substrate.

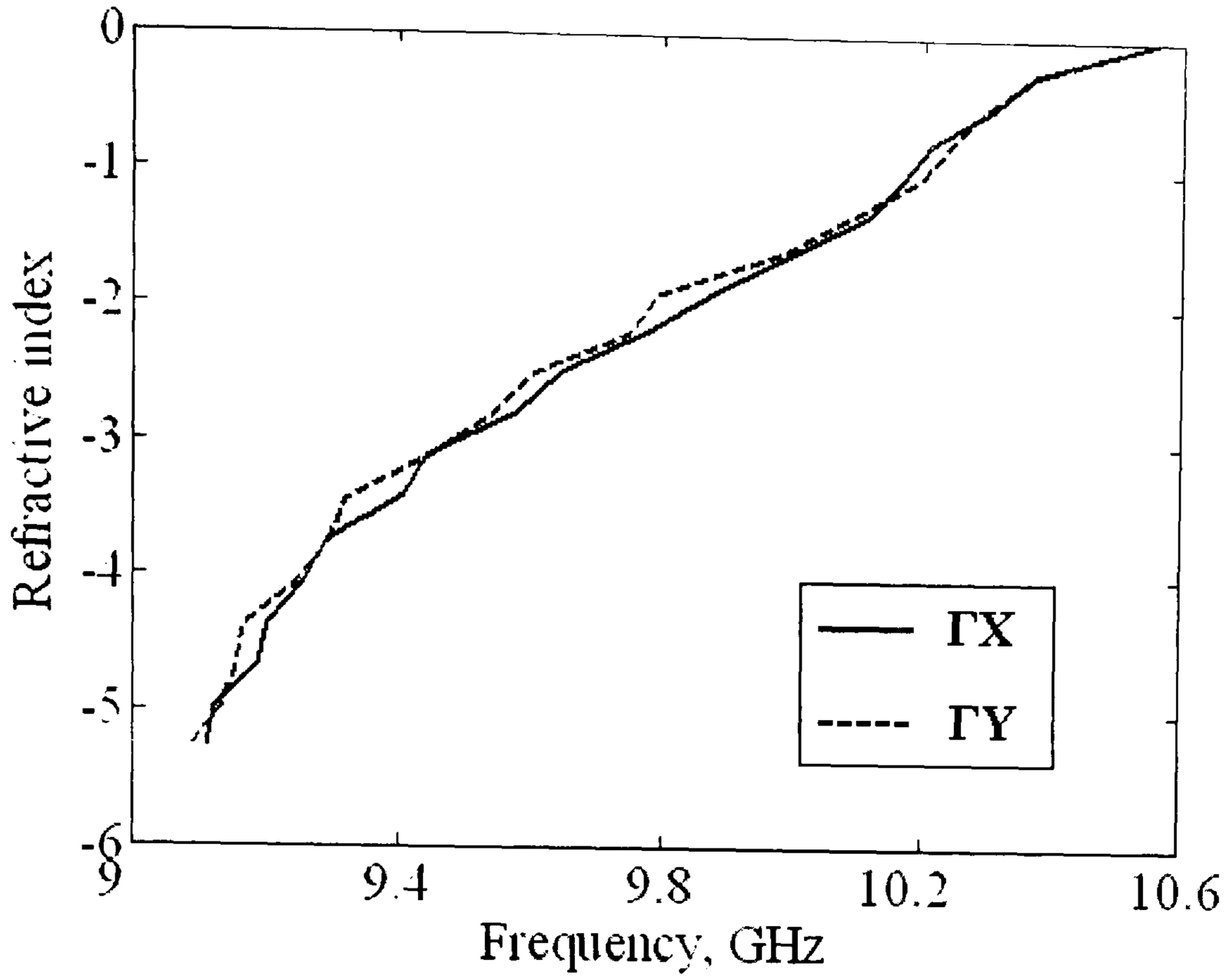

Fig. 4.14 Refractive index of the spiral element in Fig. 4.12.

4.4 Validation of Planar LH Propagation

4.4.1 Finite Structure of Left-Handed Materials

In order to validate LH propagation in the proposed structure we carried out full wave FEM simulations (HFSS) of finite structures. To ease of the computational effort required, the simulations were made for the loaded split loop rather than the spiral split-loop. One-dimensional arrays with 4, 5 and 6 elements have been simulated respectively. As shown in Fig. 4.15, the elements are aligned in a single column along the ΓX direction, where LH propagation occurs for the first TE mode. Perfect electric conductor (PEC) boundary condition has been imposed on either side in order to

ensure that TE polarization is maintained. The structure is fed with a waveguide mode of the same polarisation and the transmission coefficients (magnitude and phase) are obtained for the three arrays. The electric field distribution on the ports is shown in Fig. 4.16.

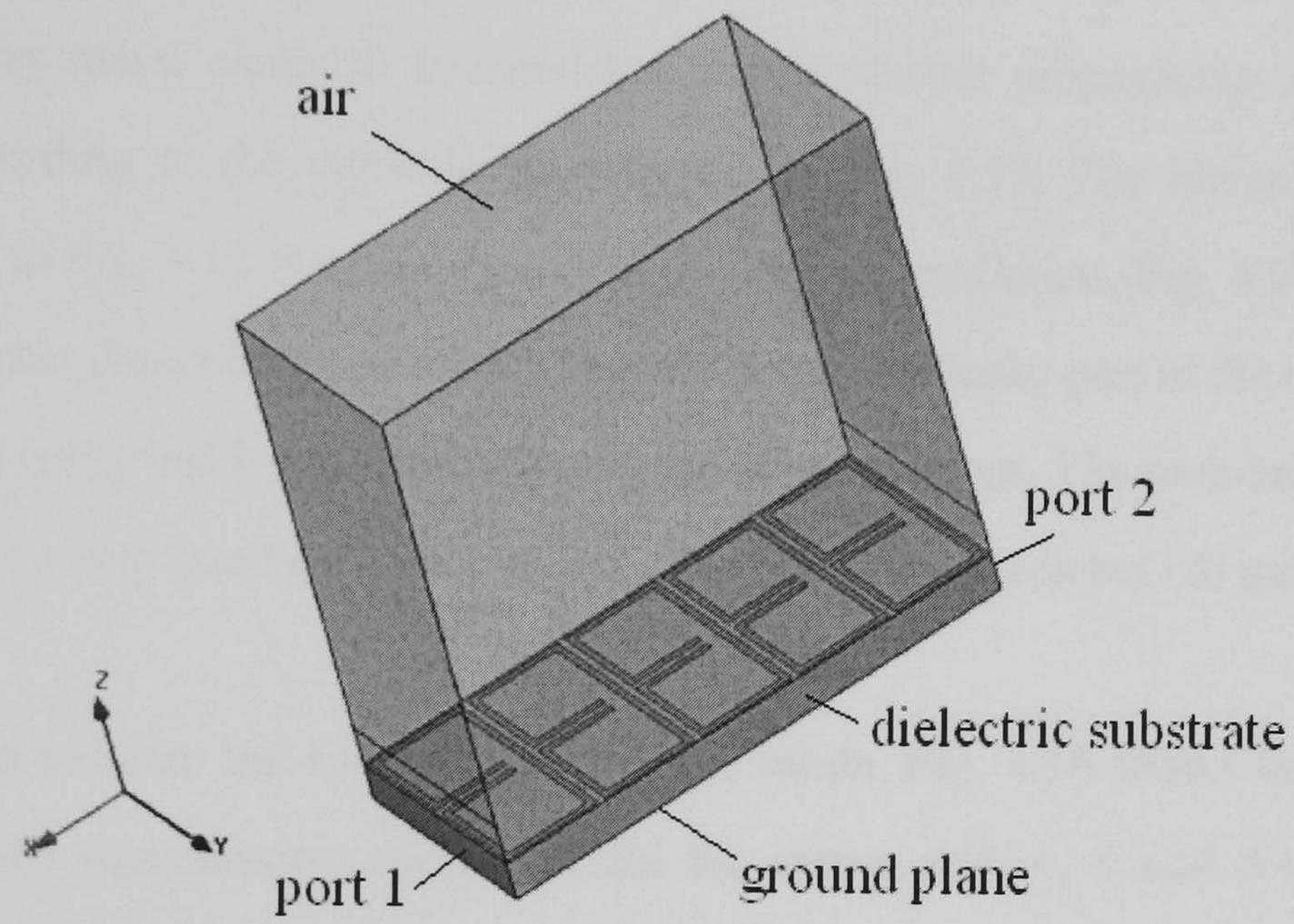

Fig. 4.15 Finite structure model in HFSS.

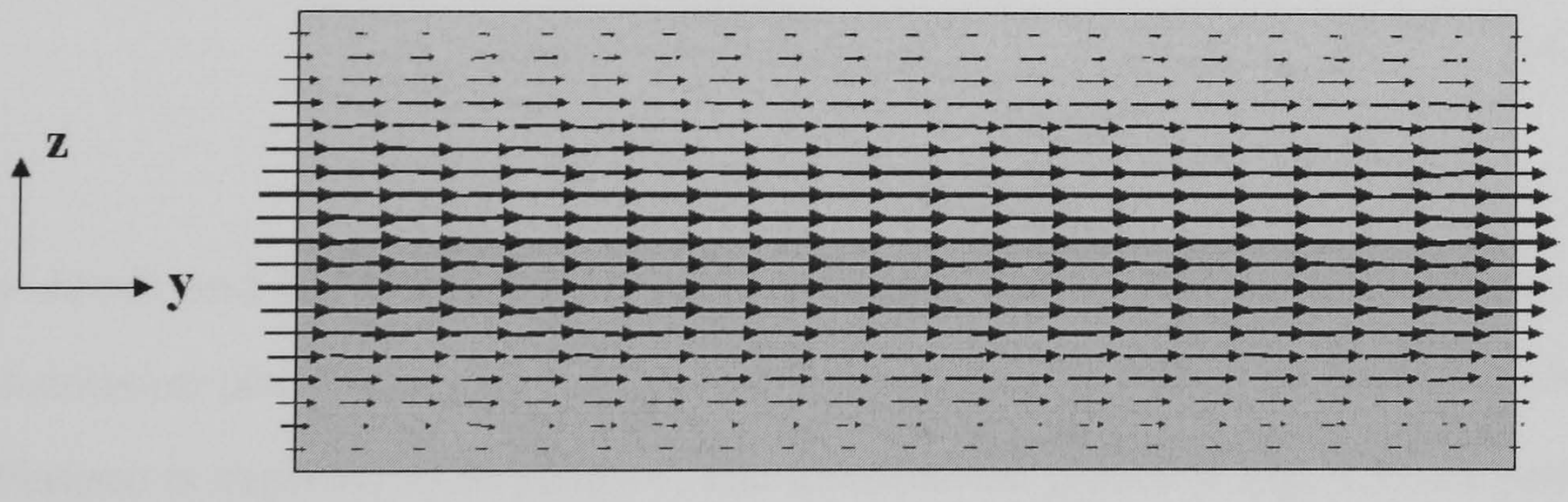

Fig. 4.16 E field distribution on the ports.

4.4.2 Software Simulation

Fig. 4.18 shows the magnitude of the transmission coefficient for the three arrays. The pass-band is identified as the LH mode and extends between 4.2GHz to 5.8GHz. To ensure the propagation modes are contributed by the arrays, the model in Fig. 4.15 but without any metal elements is simulated. No supported propagation wave can be found according to the transmission response in Fig. 4.17. The lower edge of the pass-band in Fig. 4.18 is in good agreement with our prediction (Fig. 4.9). The upper edge is higher than what presented in Fig. 4.9 due to the leaky part of the mode, which can carry energy but is not shown in the dispersion diagram. The pass-band shown in Fig. 4.18 is a very good indication of the existence of the predicted LH mode.

In order to validate the LH properties of the mode, Fig. 4.19 shows the calculated phase of the transmission coefficient for the arrays with 4, 5 and 6 elements. In general, the difference of the transmission phase between two transmission lines of lengths d1 and d2 is [30]

$$\Delta\varphi = -\frac{\omega \cdot n(\omega)}{c}(d_2 - d_1) \tag{4.13}$$

For d2>d1 and RH media with positive refractive index (n>0) the difference in the transmission phase is negative. However in the case of LH medium (n<0) the phase difference is expected to be positive. The transmission phases in Fig. 4.19 are plotted with every complete cycle added to the total phase shift, so that an actual comparison of the phase is possible. In agreement to the predicted LH nature of the mode, it is observed that within the bandwidth of the LH mode the transmission phase of the 6-element array is higher than that of the 5-element, which in turn is higher than that

of the 4-element. In the band-gap between the modes, where a standing wave is formed, these phases are all equal to zero. Then at higher frequencies the transmission phases interchange, corresponding to a positive second order mode that exists for this array. Note that the transmission phase of the finite structure is in very good agreement to the phase predicted from the refractive index (Fig. 4.10) using equation (4.13).

$$n(\omega) = -\frac{c \cdot \Delta\phi}{\omega(d_2 - d_1)} \tag{4.14}$$

The comparison of the refractive index calculated from the dispersion diagram and the transmission phase is shown in Fig. 20. Fig. 4.18 and Fig. 4.19 are therefore a good verification of the LH nature of the first order mode of the presented arrays.

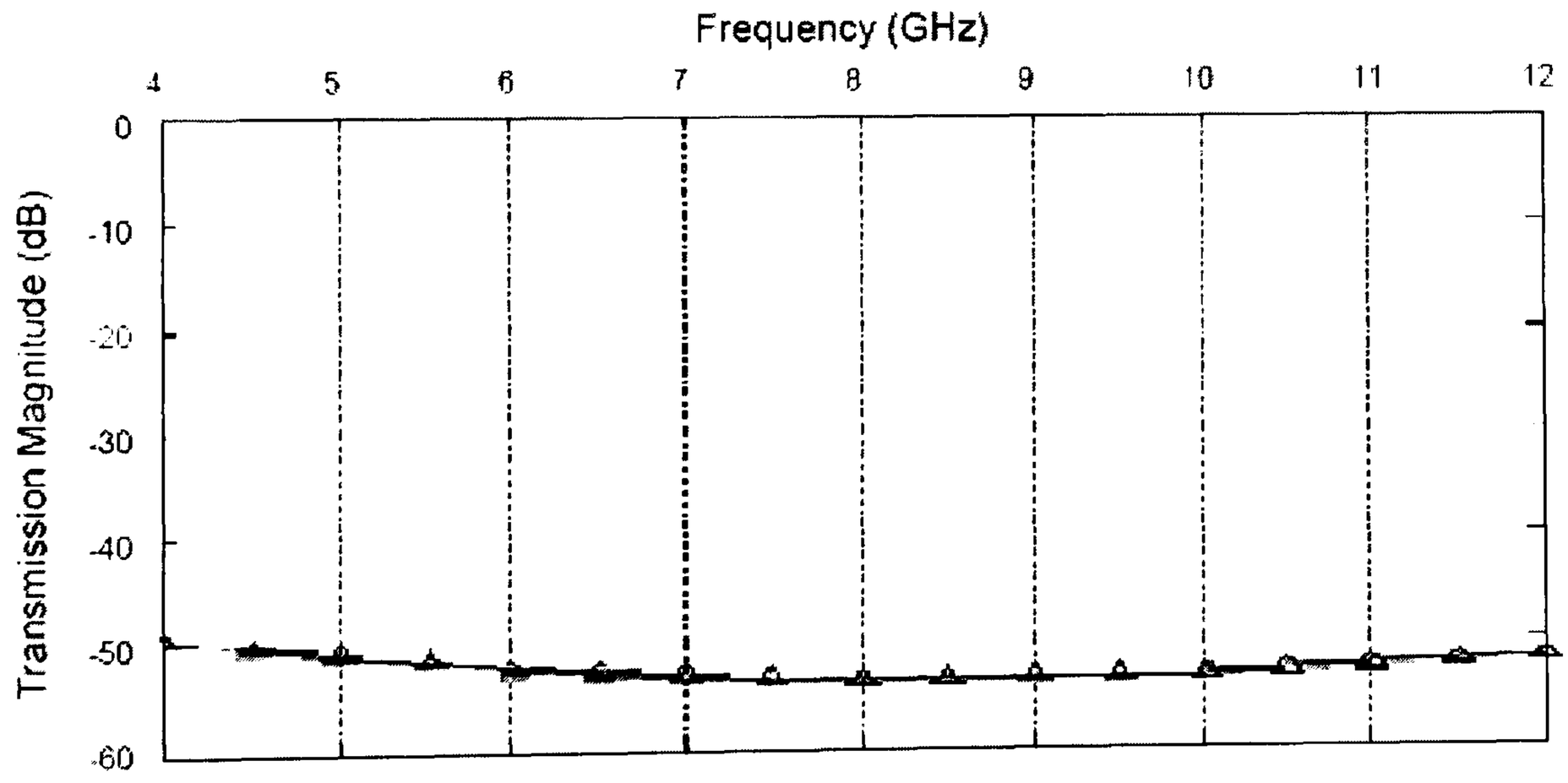

Fig. 4.17 HFSS simulation of the transmission magnitude of Fig. 4.15 without any array element.

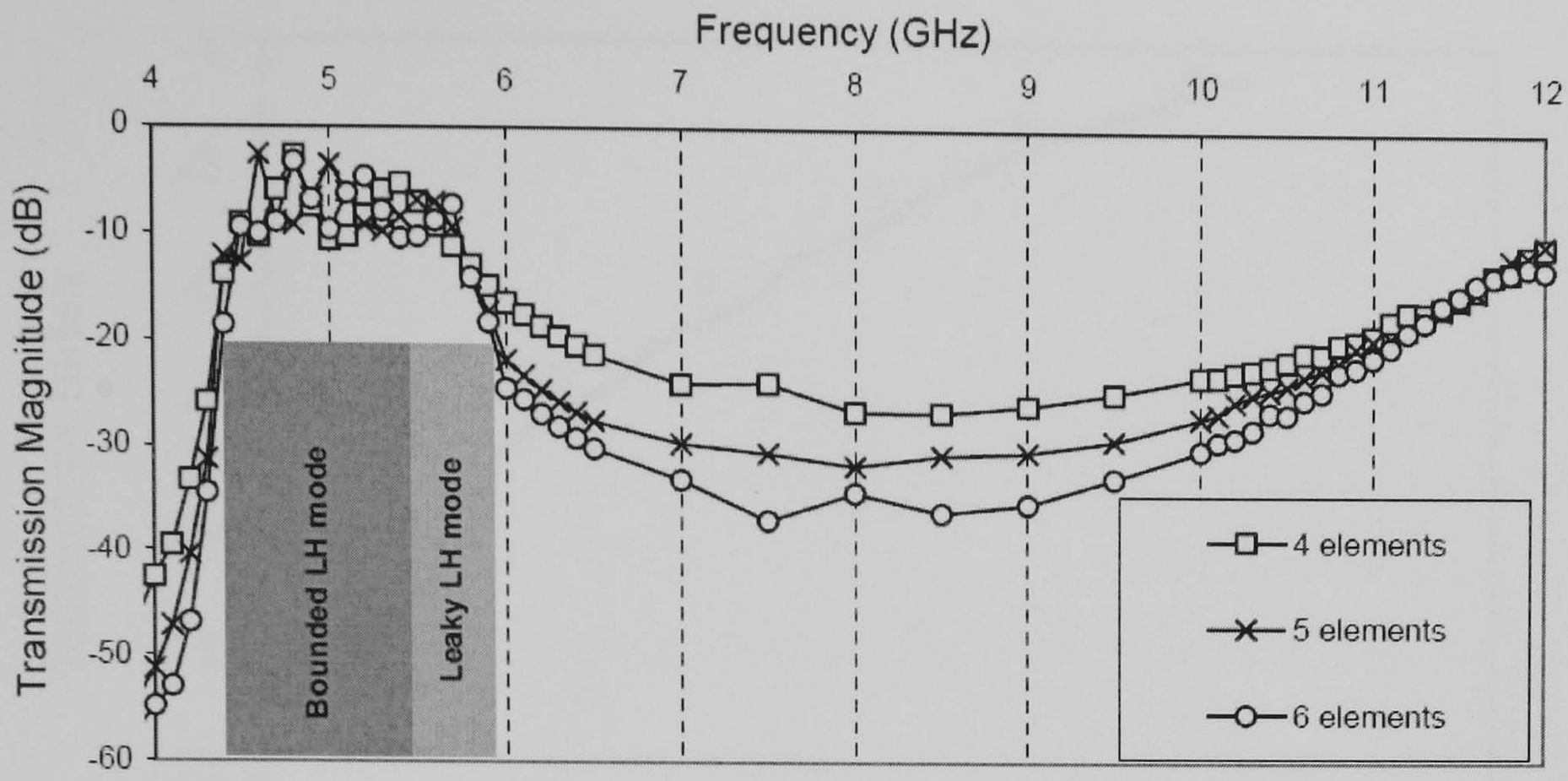

Fig. 4.18 HFSS simulation of the transmission magnitude for arrays of loaded split-loop elements with 4, 5 and 6 elements.

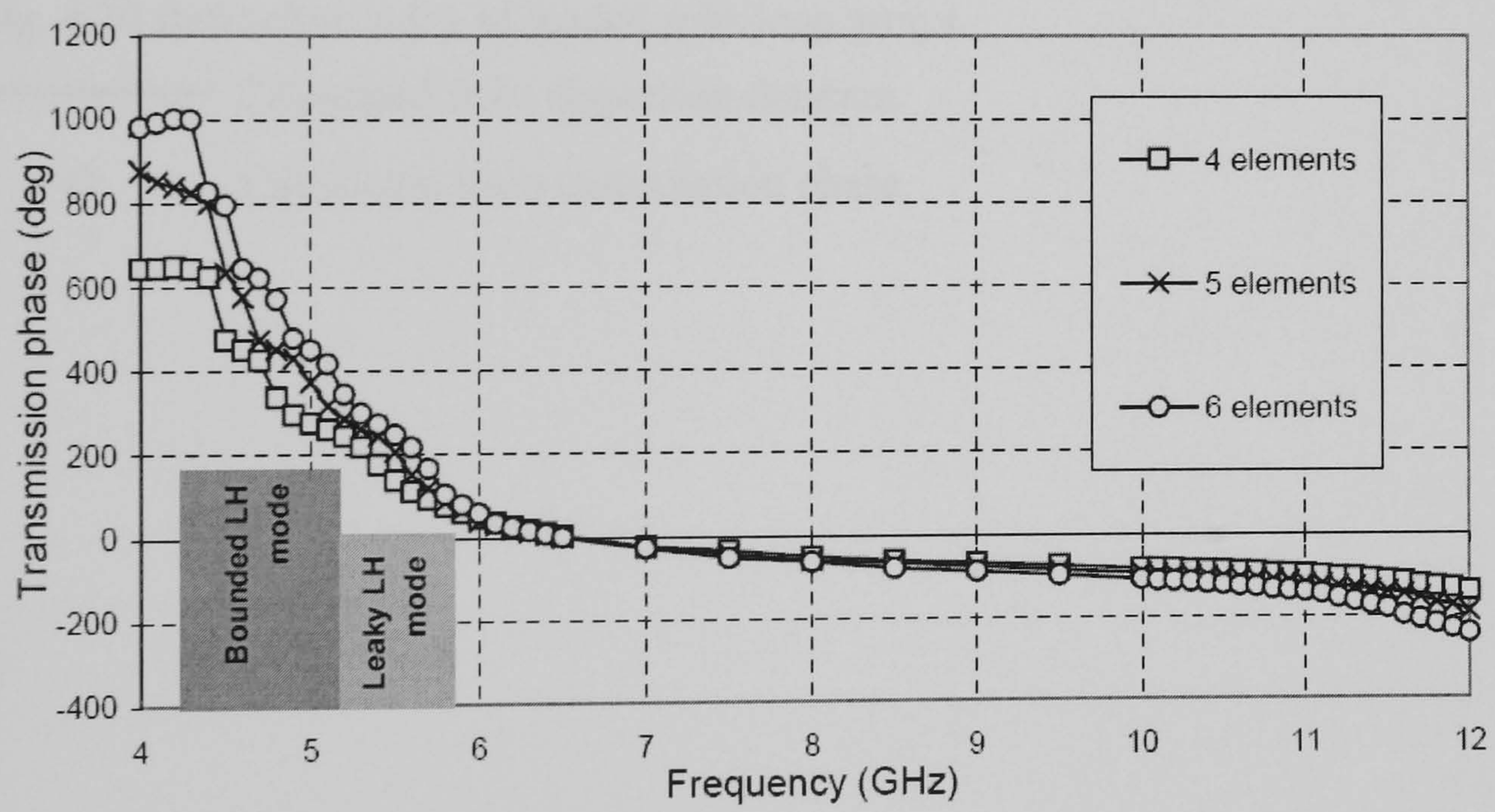

Fig. 4.19 HFSS simulation of the transmission phase for arrays of loaded split-loop elements with 4, 5 and 6 elements.

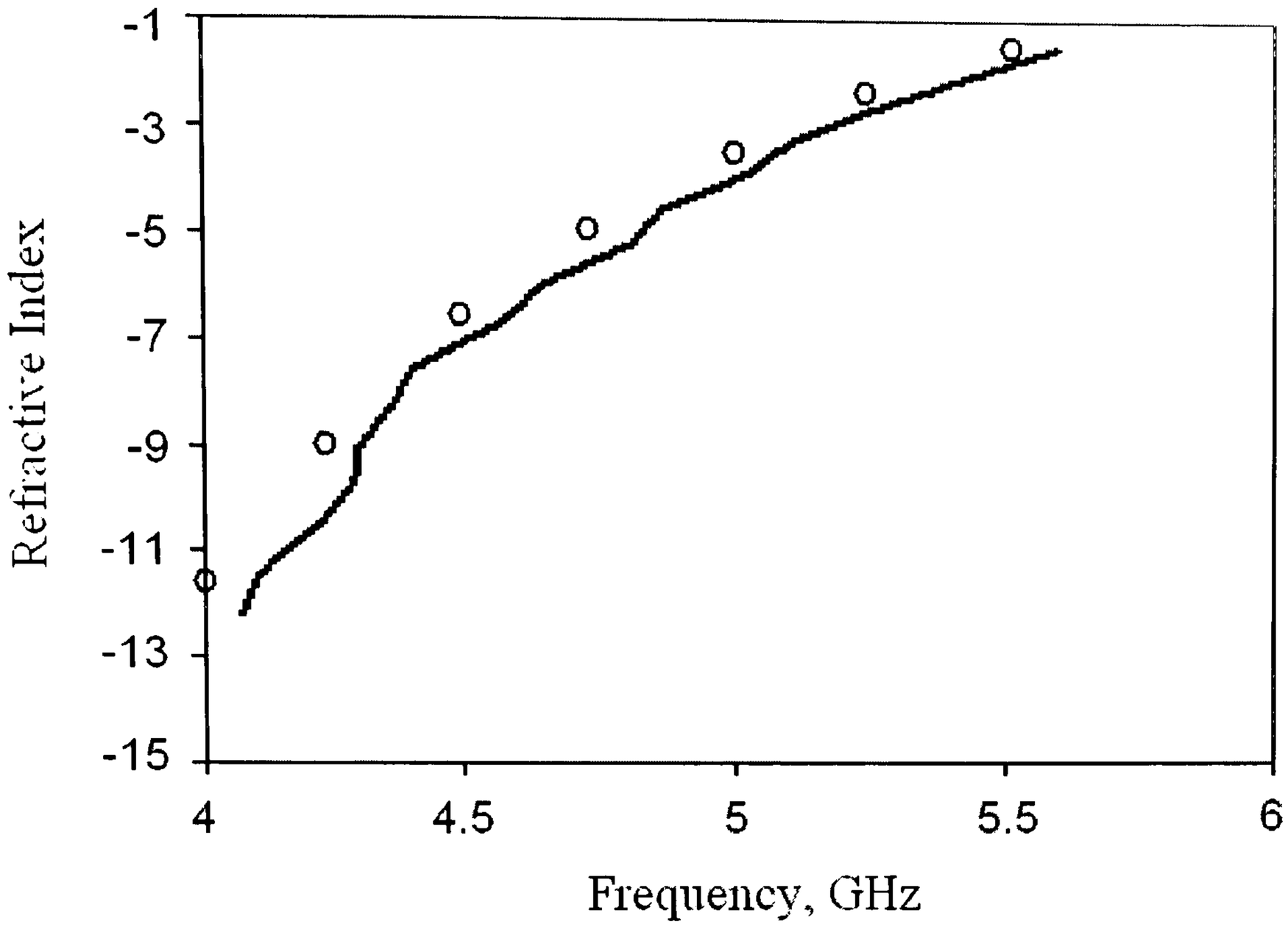

Fig. 4.20 Refractive index of loaded split-loop arrays.

——— Calculated from dispersion diagram.

O Calculated from transmission phase.

4.5 Conclusions

Based on the method presented in chapter 2, novel planar LH metamaterials have been designed. A study was carried out with regards to the effect of the interpolation step on the accuracy of the results. The dispersion diagrams of the proposed structures have been produced with an interpolation step of 1GHz which resulted in a good accuracy. The method was validated by comparison with commercial software (HFSS). The refraction index of the structures has been derived. Pretty high values of refractive index can be obtained. A thorough investigation of the modal field distribution provided a detailed explanation of the LH properties of the structures based on the dual transmission line concept. A full-wave based validation of the left-handedness has been presented. The unit cell is as small as $\lambda/24$ which allows for an equivalent effective medium model. The structures are simple, compatible with low-cost fabrication techniques and scalable to higher frequencies. Compared with the previous LHM designs by other researchers, these structures can support horizon polarized TE waves other than TM waves in microstrip LHM and take the advantages of coplanar transmission lines in microwave integrated circuit designs.

References

[1] V. G. Veselago, "The Electrodynamics of Substances with Simultaneously Negative Values of ε and μ", *Sov. Phys. Usp.*, Vol. 10, no. 4, pp. 509-514, 1968

[2] J. B. Pendry, A. J. Holden, D. J. Robbins, and W. J. Stewart, "Magnetism from Conductors and Enhanced Nonlinear Phenomena", *IEEE Trans. Microwave Theory Tech.*, Vol. 47, no. 11, pp. 2075-2084, 1999

[3] R. A. Shelby, D. R. Smith and S. Schultz, "Experimental Verification of a Negative Index of Refraction", Science, Vol. 292, pp. 77-79, 2001

[4] G. V. Eleftheriades, A. Iyer and P. Kremer, "Planar Negative Refractive Index Media Using Periodically L-C Loaded Transmission Lines", *IEEE Trans. Microwave Theory Tech.*, Vol. 50, no. 12, pp. 2702-2711, 2002

[5] A. Sanada, C. Caloz and T. Itoh, "Planar Distributed Structures With Negative Refractive Index", *IEEE Trans. Microwave Theory Tech.*, Vol. 52, no. 4, pp. 1252 – 1263, 2004

[6] A. A. Oliner, "A periodic structure negative refractive index medium without resonant elements", *IEEE AP-S USNC/URSI National Radio Science Meeting Digest*, 2002, p. 41

[7] D. R. Smith, Willie J. Padilla, D. C. Vier, S. C. Nemat-Nasser and S. Schultz, "A Composite Medium with Simultaneously Negative Permeability and Permittivity", *Phys. Rev. Lett.*, Vol. 84, no. 18, pp. 4184-4187, 2000

[8] G. V. Eleftheriades, A. Iyer and P. Kremer, "Planar Negative Refractive Index Media Using Periodically L-C Loaded Transmission Lines", *IEEE Trans. Microwave Theory Tech.*, Vol. 50, no 12, pp. 2702-2711, 2002

[9] A. Sanada, C. Caloz and T. Itoh, "Planar Distributed Structures With Negative Refractive Index", *IEEE Trans. Microwave Theory Tech.*, Vol. 52, no. 4, pp. 1252–1263, 2004

[10] C. Caloz, and T. Itoh, *Electromagnetic Metamaterials: Transmission Line Theory and Microwave Applications*, John Wiley & Sons, Inc., New York, 2004

[11] G. Goussetis, A. P. Feresidis, S. Wang, Y. Guo, and J. C. Vardaxoglou, "Planar Left-Handed Artificial Metamaterials", *J. Opt. A: Pure Appl. Opt.* Vol. 7, no. 2, pp. S44–S50, 2005

[12] C. Caloz and T. Itoh, "Transmission Line Approach of Left-Handed (LH) Materials and Microstrip Implementation of an Artificial LH Transmission Line", *IEEE Trans. Antennas Propagat.*, Vol. 52, no. 5, pp. 1159 – 1166, 2004

[13] A. Grbic and G. V. Eleftheriades, "Dispersion Analysis of a Microstrip-Based Negative Refractive Index Periodic Structure", *IEEE Microwave and Wireless Components Letters*, Vol. 13, no. 4, pp. 155-157, 2003

[14] C.-Y. Cheng and R. W. Ziolkowski, "Tailoring Double-Negative Metamaterial Responses to Achieve Anomalous Propagation Effects Along Microstrip Transmission Lines", *IEEE Trans. Microwave Theory Tech.*, Vol. 51, no. 12, pp. 2306 – 2314, 2003

[15] M. A. Antoniades, G. V. Eleftheriades, "Compact Linear Lead/Lag Metamaterial

Phase Shifters for Broadband Applications", *IEEE Antennas Wireless Propag. Lett.*, Vol. 2, pp. 103-106, 2003

[16] S. Lim, C. Caloz, T. Itoh, "Metamaterial-Based Electronically Controlled Transmission-Line Structure as a Novel Leaky-Wave Antenna with Tunable Radiation Angle and Beamwidth", *IEEE Trans. Microwave Theory Tech.*, Vol. 53, no. 1, pp. 161–173, 2005

[17] H. Kim; A. B. Kozyrev, A. Karbassi, and D. W. van der Weide,"Linear Tunable Phase Shifter Using a Left-Handed Transmission Line", *IEEE Microwave and Wireless Components Letters*, Vol. 15, no. 5, pp. 366-368, 2005

[18] M. A. Antoniades, G. V. Eleftheriades, "A Broadband Wilkinson Balun Using Microstrip Metamaterial Lines", *IEEE Antennas Wireless Propag. Lett.*, Vol. 4, pp. 209-212, 2005

[19] M. A. Antoniades, G. V. Eleftheriades, "A Broadband Series Power Divider Using Zero-Degree Metamaterial Phase-Shifting Lines", *IEEE Microwave and Wireless Components Letters*, Vol. 15, no. 11, pp.808-810, 2005

[20] Islam, R., Elek, F. and Eleftheriades, G. V.: "Coupled-line metamaterial coupler having co-directional phase but contra-directional power flow", *Electronic Letters*, Vol. 40, pp. 315-317, 2004

[21] Islam, R. and Eleftheriades, G. V.: "Phase-agile branch-line couplers using metamaterial lines", *IEEE Microwave and Wireless Components Letters*, Vol. 14, pp. 340-342, 2004

[22] C. Caloz, A. Sanada, and T. Itoh, T.: "A novel composite right-/left-handed coupled-line directional coupler with arbitrary coupling level and broad bandwidth", *IEEE Trans. Microwave Theory and Techniques*, Vol. 52, pp. 980-992, 2004

[25] L. Liu, C. Caloz, and T. Itoh, "Dominant mode (DM) leaky-wave antenna with backfire-to endfire scanning capability", *Electronic Letters*, Vol. 38, pp. 1414-1416, 2000

[26] A. Sanada, M. Kimura, I. Awai, H. Kubo, C. Caloz, and T. Itoh,: "A planar zeroth order resonator antenna using left-handed transmission line", *European Microwave Conference Digest*, Vol. 2, pp. 1341-1344, 2004

[27] T. J. Yen, W. J. Padilla, N. Fang, D. C. Vier, D. R. Smith, J. B. Pendry, D. N. Basov and X. Zhang, "Terahertz Magnetic Response from Artificial Materials", *Science*, pp. 1494-1496, 2004

[28] A. Erentok, P. L. Luljak and R. W. Ziolkowski, "Characterization of a Volumetric Metamaterial Realization of an Artificial Magnetic Conductor for Antenna Applications", *IEEE Trans. Antennas Propagat.*, Vol. 53, no. 1, pp. 160-172, 2005

[29] *High Frequency Structure Simulator* (HFSS), ver. 9.0, Ansoft Corporation, 2003

[30] O. F. Siddiqui, M. Mojahedi and G. V. Eleftheriades, "Periodically Loaded Transmission Line With Effective Negative Refractive Index and Negative Group Velocity", *IEEE Trans. Antennas Propagat.*, Vol. 51, no. 10, pp. 2619-2625, 2003

5. Measurements of Planar Left-Handed Materials

5.1 Introduction

Novel planar left-handed materials have been introduced and validated by a full-wave software simulation in Chapter 4. The left-handed propagation has been theoretically proved. In order to confirm that the proposed structures support left-handed propagation in practice and thus verify that they are suitable to be used in practical microwave designs, experimental measurements are described in this chapter. The measurements are based on a microstrip transmission line feeding model, which is partly replaced by the planar left-handed materials. Full-wave 3D simulations (in HFSS^{TM}) of the proposed topologies are carried out prior to the experimental testing. According to the dispersion diagram in Chapter 4.3.3, power can be delivered through these structures in the frequency ranges where the left-handed (first) and right-handed

(higher) modes exist. In the remaining frequency ranges, the structures show band-gap features as those obtained in general from discontinued microstrip lines. The difference between the propagation in the frequency ranges of left-handed mode and right-handed mode is the following: the phase velocity of the surface-wave through the planar materials is negative in the left-handed mode, and in the right-handed mode, the wave is a slow wave but with a positive phase velocity. This enables us to prove the left-handed propagations by measuring the phase difference between the two ports for different lengths of these structures, as has been described in chapter 4.4.

5.2 Design of Left-Handed Materials Measurement

5.2.1 Initial Design

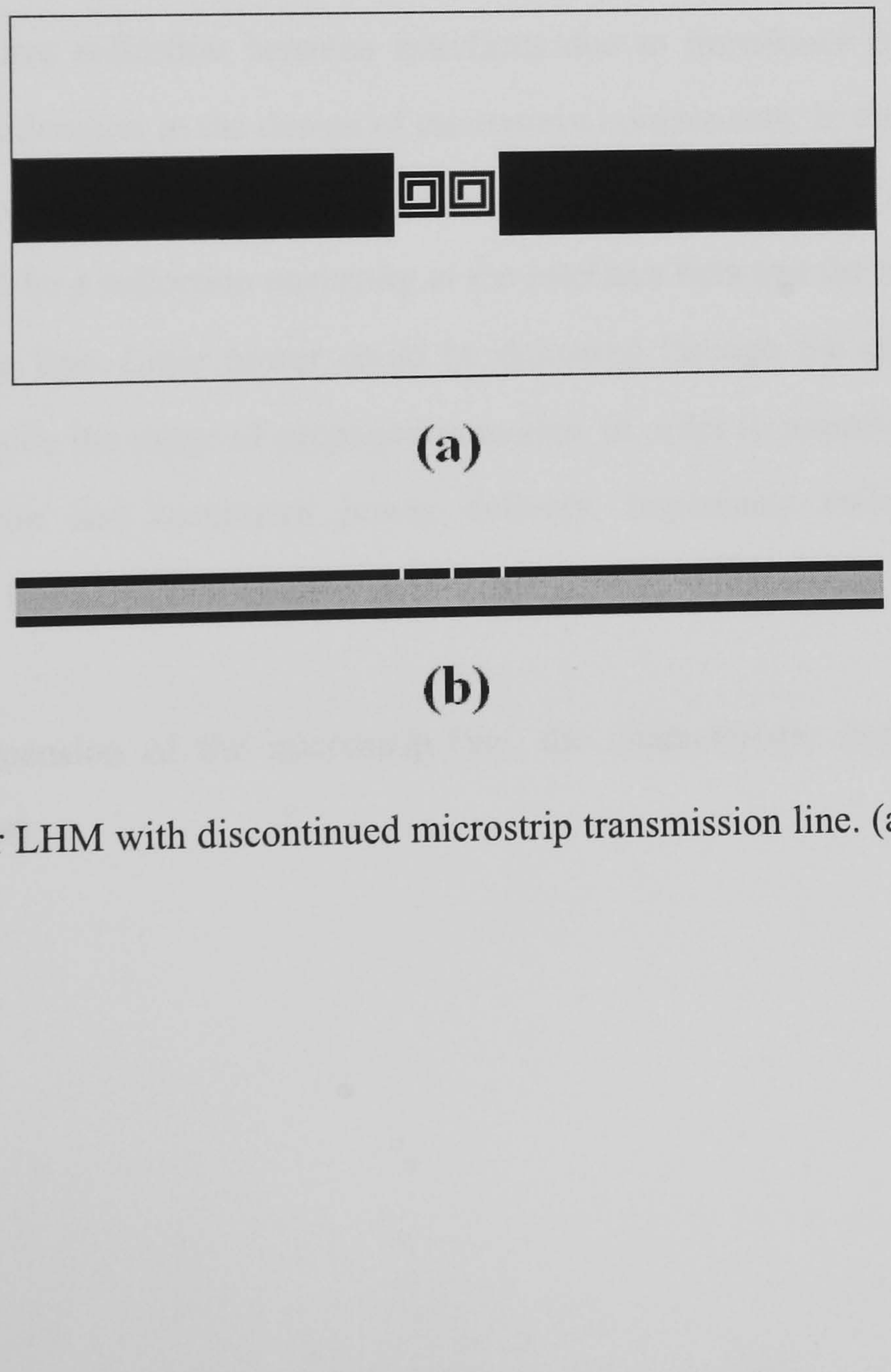

Fig. 5.1 Planar LHM with discontinued microstrip transmission line. (a) Top view. (b) Side view.

A microstrip transmission line feeding method is used here to measure left-handed materials [1]-[3]. Based on this idea, the initial design of the planar left-handed material measurement is as shown in Fig. 5.1. The 50Ω microstrip transmission line, with 3.5mm line-width and over a 1.13mm-thick grounded dielectric substrate (ε=2.2), is partly replaced by the isotropic planar left-handed material introduced in Chapter 4.3.3.. The frequency ranges of the S21 pass bands are expected to be corresponding with those of the propagation modes in the dispersion diagram in Fig. 4.13. Using a similar method to that of Chapter 4.4, the left-handed propagation can be differentiated with the right-handed propagations by comparing the S21 phases for different number of planar LHM unit cell insertions.

5.2.2 Impedance Matching and Tuning

Unexpected wave reflection between interfaces due to impedance mismatch, is an important consideration in the design of microwave components. In the design of Fig. 5.1, since the characteristic impedance of the planar left-handed material is other than 50Ω, there will be a reflection occurring at the interface between the material and the 50Ω microstrip line. Little power could be delivered through the structure even at frequencies inside the range of propagation modes. In order to improve the quality of the transmission and maximum power delivery, impedance matching plays an important role in microwave designs.

Given the dimension of the microstrip line, the characteristic impedance can be calculated as [4]

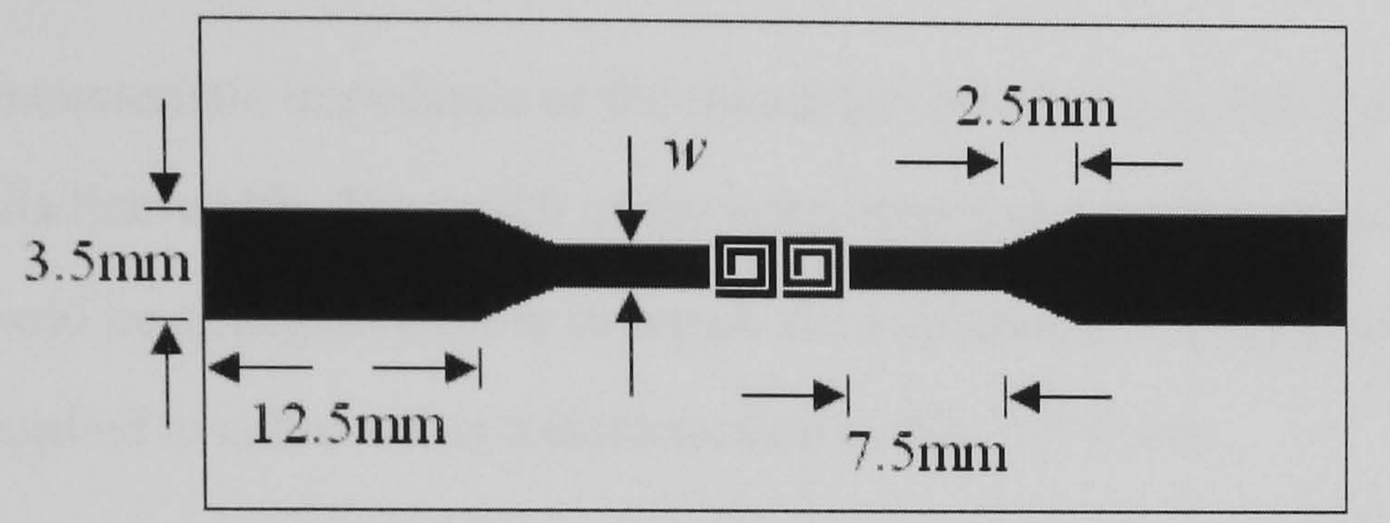

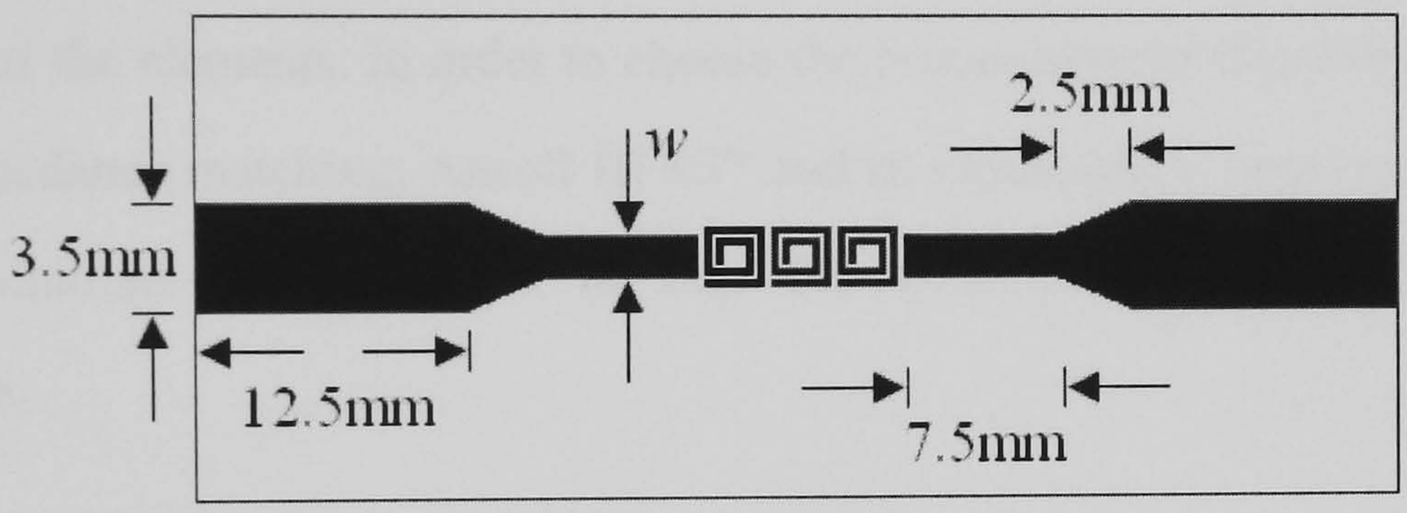

Fig. 5.2 Planar left-handed material with tapered microstrip transmission line.

$$Z_0 = \begin{cases} \dfrac{60}{\sqrt{\varepsilon_e}} \ln\left(\dfrac{8d}{W} + \dfrac{W}{4d}\right), & W/d \le 1 \\ \dfrac{120\pi}{\sqrt{\varepsilon_e}\left[W/d + 1.393 + 0.667\ln\left(W/d + 1.444\right)\right]}, & W/d \ge 1 \end{cases} \tag{5.1}$$

where d is the substrate thickness, W is the conductor width, and the effective dielectric constant of the microstrip line is given approximately by

$$\varepsilon_e = \frac{\varepsilon_r + 1}{2} + \frac{\varepsilon_r - 1}{2} \frac{1}{\sqrt{1 + 12d/W}} \tag{5.2}$$

Thus, the characteristic impedance of the microstrip transmission line can be changed by varying its line-width. The width of the microstrip line near the planar left-handed material should be changed in order to match the impedance. The tapered line method [4] can be applied to achieve this transformation as Fig. 5.2 shows.

However, unlike that of the microstrip lines, the characteristic impedance of the planar left-handed material is difficult to be derived by calculation because of the irregular geometry of the elements. In order to choose the proper tapered microstrip line-width for the impedance matching, Ansoft HFSS™ and its Optimetrics™ environment [5] are used to simulate the structures in Fig. 5.2 with different tapered microstrip line-widths.

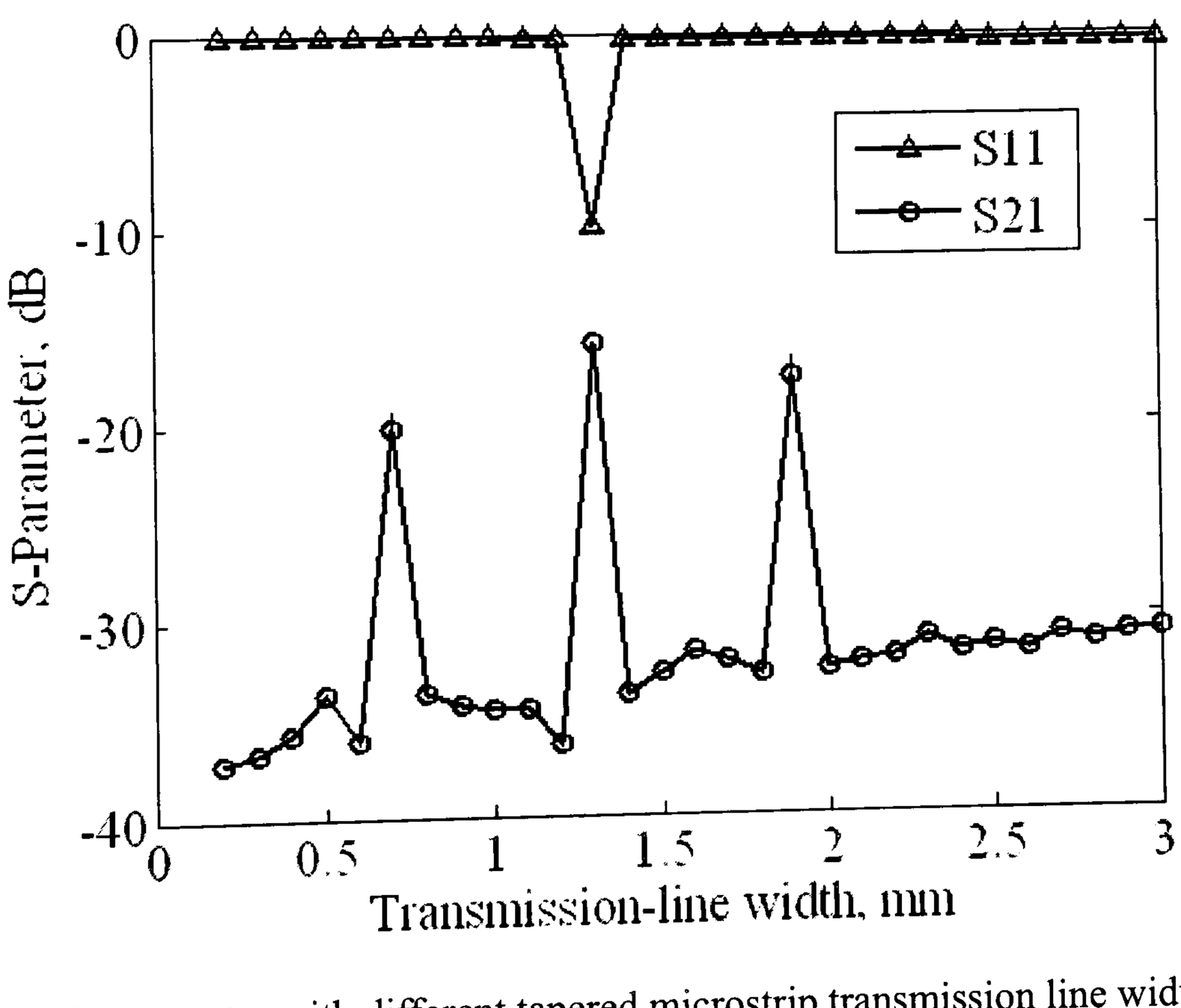

Fig. 5.3 S-parameter with different tapered microstrip transmission line widths *w*.

The exciting frequency in the simulation is chosen at 9.6GHz, which is inside the range of the left-handed mode. The result of S-parameter with different tapered microstrip transmission line widths is shown in Fig. 5.3. The line width varies from 0.2mm to 3mm. At width value of 1.3mm, there are simultaneously an S11 valley and an S21 peak. This is the proper line-width for impedance matching, because the return loss at this point is less than others.

5.2.3 Left-Handed Propagation

To verify the feasibility of the design in Fig. 5.2, simulations of the structures have been carried out in Ansoft HFSS™. The excitations are set to be wave ports on both ends of the substrate boards. The electric field distribution of the wave ports used in the model are shown in Fig. 5.4.

Fig. 5.5 shows the simulated S-parameters for two and three elements insertions. The first propagation mode at 9-10GHz and the second propagation mode at 20-23GHz can be clearly observed from the graph, which has a good agreement with the dispersion diagram in Fig. 4.13. It is worth noting that there are losses in transmission in the lower frequency range of the left-handed mode as Fig. 5.5(b) shows. This corresponds to impedance mismatch effects that degrade the S21. Only a small frequency band exhibits a relatively good transmission response, due to the narrow bandwidth of the LH mode (Fig. 4.13). The ripples in the passband are attributed to standing wave effects produced by the mismatches.

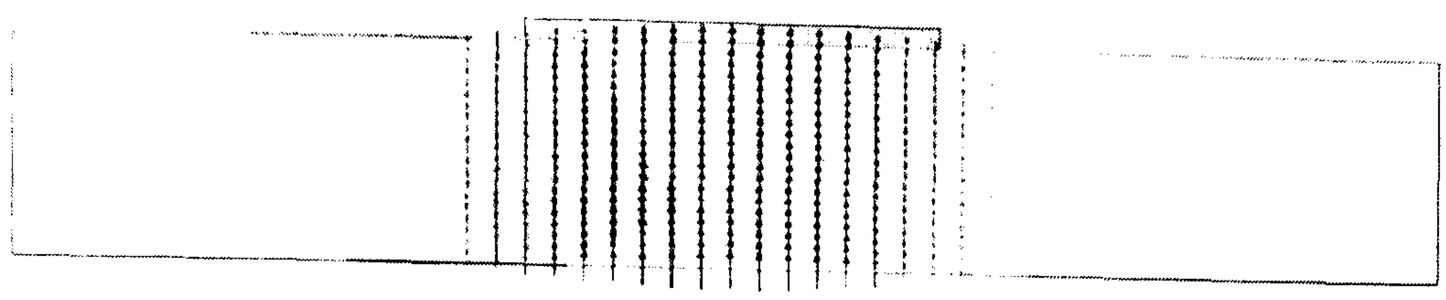

Fig. 5.4 E field distribution on the ports.

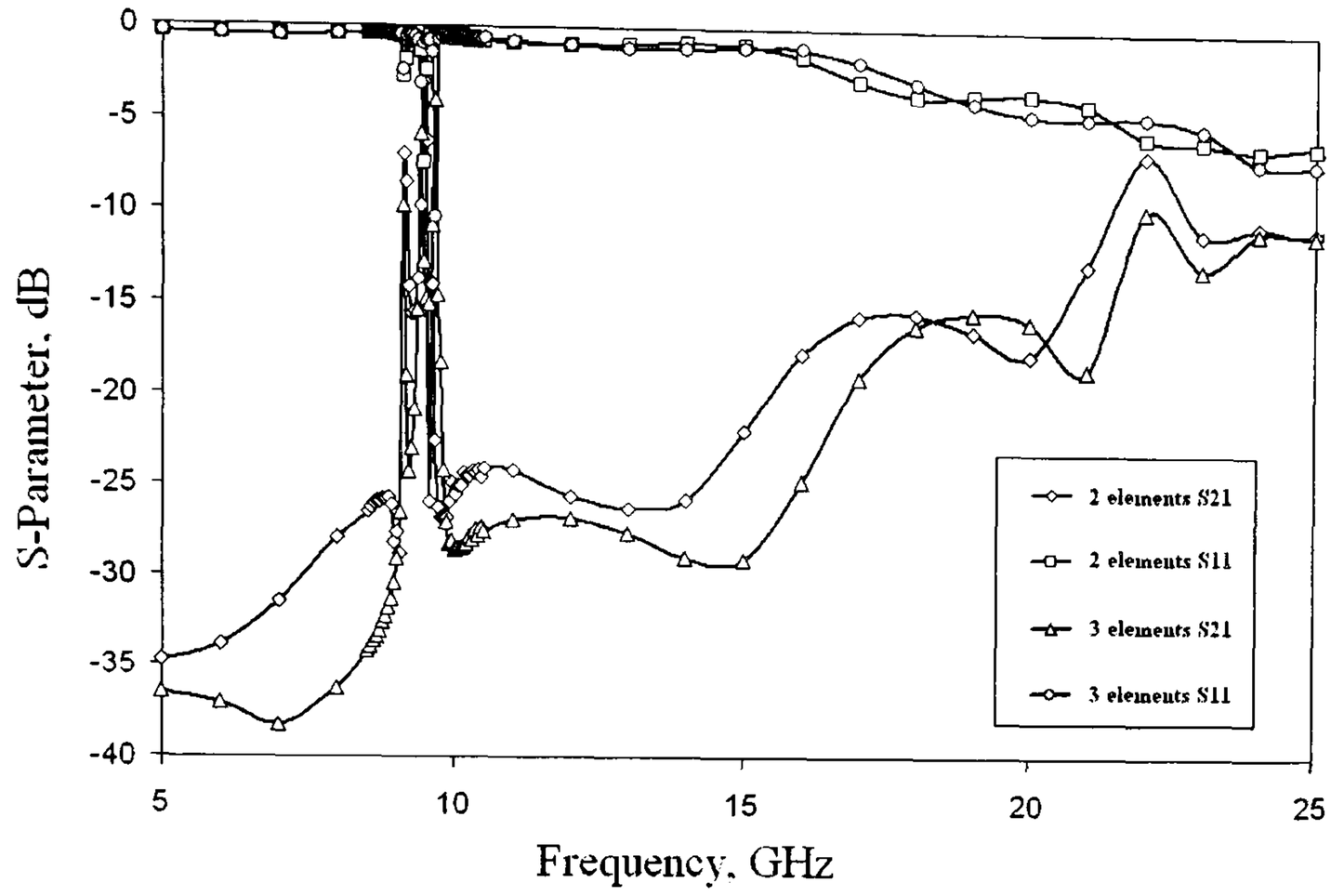

(a)

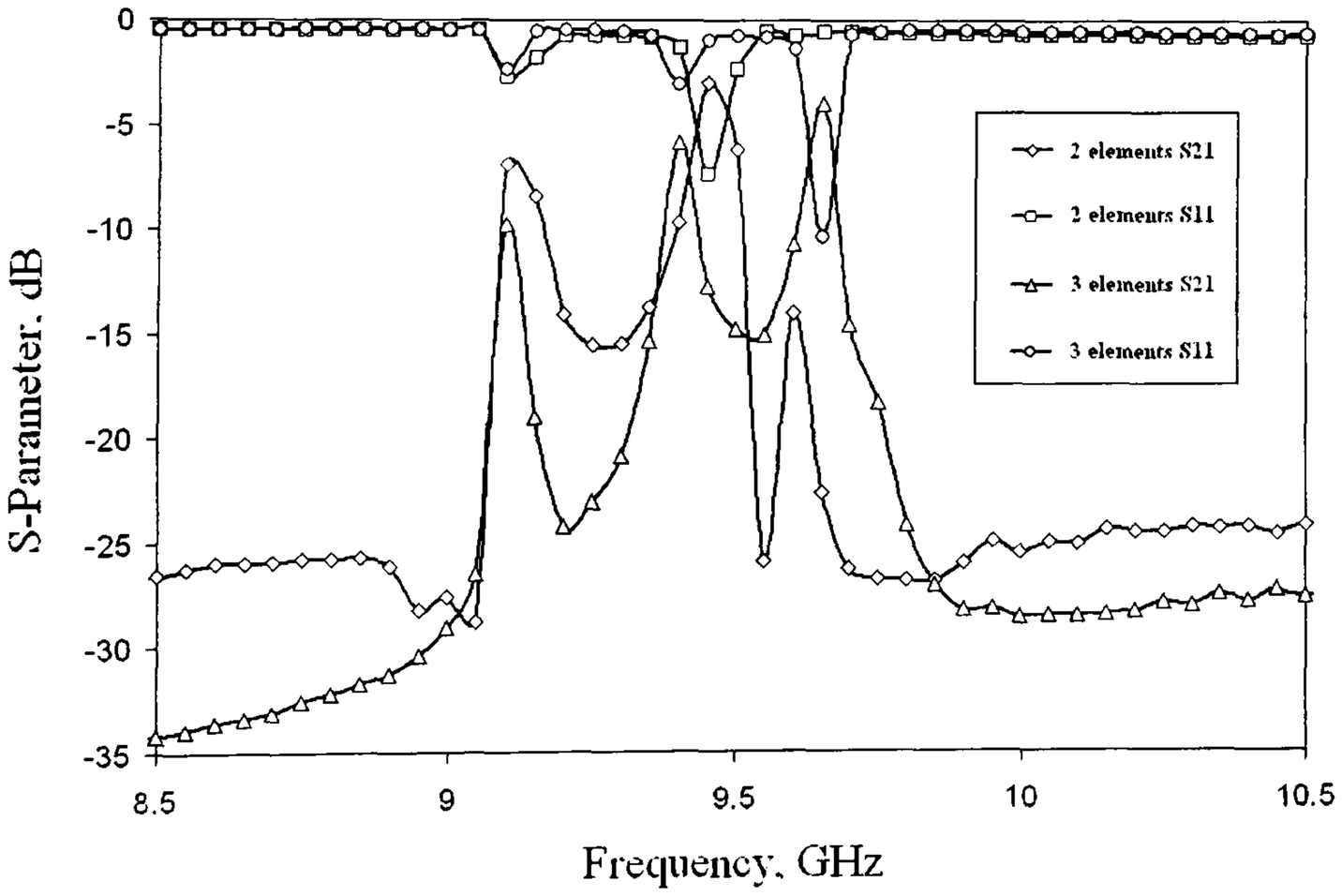

(b)

Fig. 5.5 Simulated S-parameters for two and three elements. (a) From 5GHz to 25GHz. (b) From 8.5GHz to 10.5GHz.

An animated plot of the electric field distribution inside the dielectric substrate for the three element design is also presented in Fig. 5.6. The excitation here is chosen to be 9.65GHz, which is inside the frequency range of the first mode and also corresponds to the best S21 value. Port 1 and port 2 are set on the left and the right side of the board respectively. Port 1 is the excitation and surface waves travel from the left side to the right side as they are excited. Three graphs are shown in Fig. 5.6 which are time samples from a complete animation within one period. The large cyan clouds on the sides are wave peaks supported by the transmission line and the small clouds with red and yellow colours in the middle are wave peaks supported by the planar left-handed material. It can be found from the graphs that the wave peaks supported by the transmission line travel from left to right and the wave peaks supported by the planar left-handed material travel from right to left. Since the power flow goes from the left side to the right side, it is proved that the waves have a positive phase velocity through the transmission line and have a negative phase velocity over the planar left-handed material.

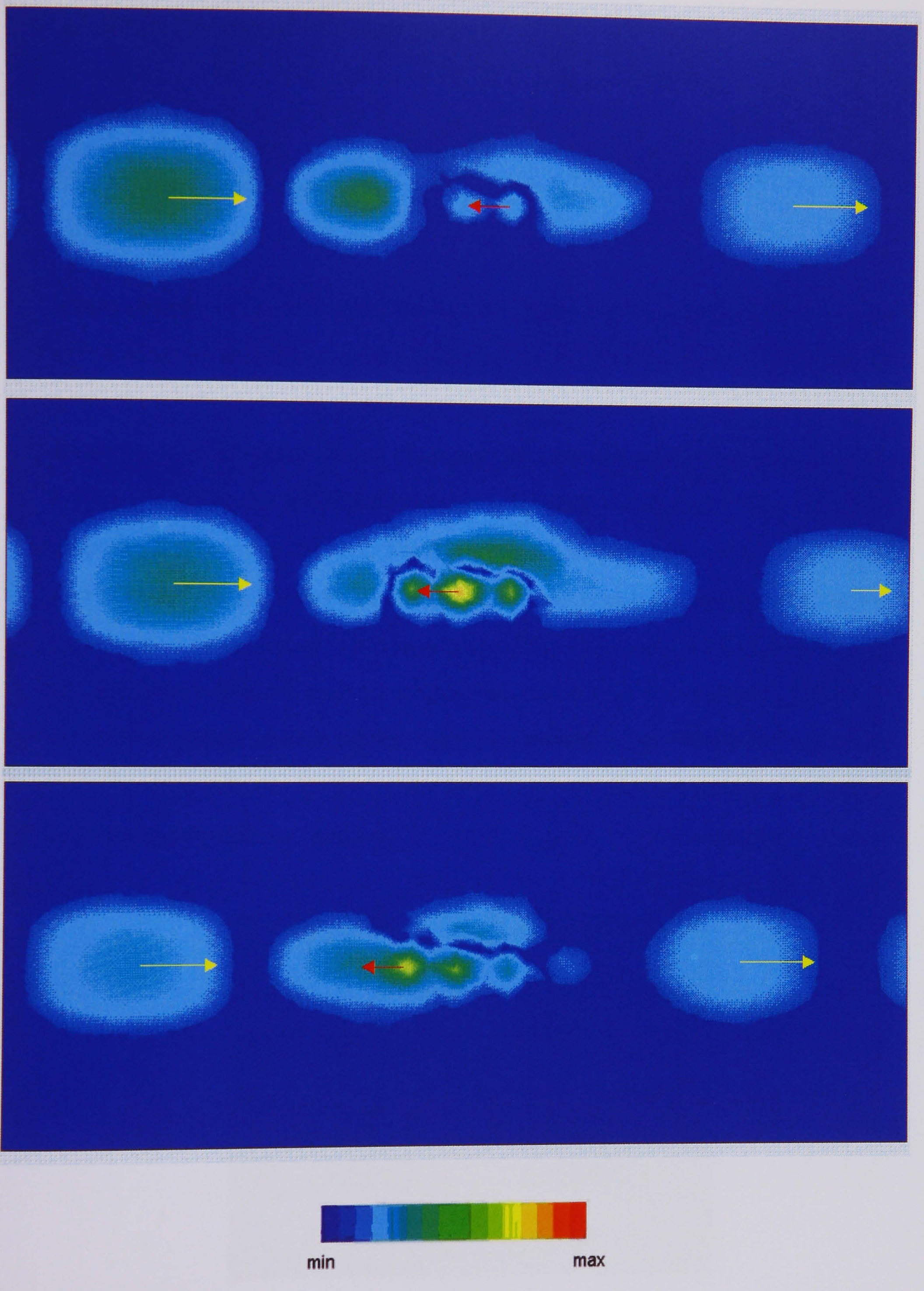

Fig. 5.6 Propagation with negative phase velocity.

5.3 Experimental Measurement

5.3.1 Measurement Setup

In the fabrication of the structures, Taconic™ TLY Printed Circuit Board (PCB) is used, with a thickness of 1.13mm, relative permittivity of 2.2 and dielectric loss tangent of 0.009. Two different boards with 2 and 3 left-handed material elements are made. The microstrip transmission lines and the planar left-handed materials are printed on the top layer of the boards which are grounded at the back. Photographs of the fabricated structures are shown in Fig. 5.7. The SMA connectors used here are RS Tab Contact End Launcher for 1.57mm PCB. The structures have been measured with the Anritsu Lightning™ 37000D Vector Network Analyser (Fig. 5.8), which is a high performance two-port vector network analyser for passive structures with a broadband frequency range up to 65GHz. Before measurements, the system is calibrated in the frequency range between 5GHz to 25GHz, where the first two propagation modes of the planar left-handed materials are expected.

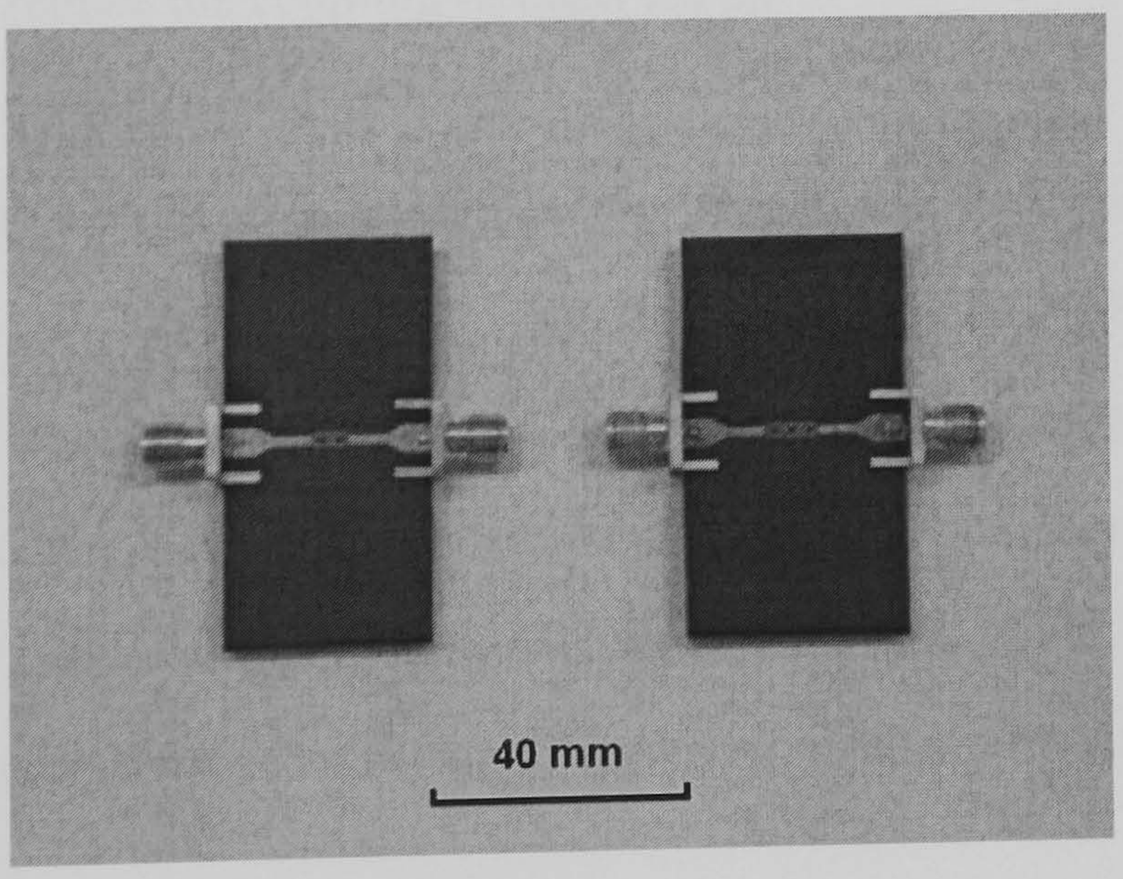

Fig. 5.7 Structures under measurement.

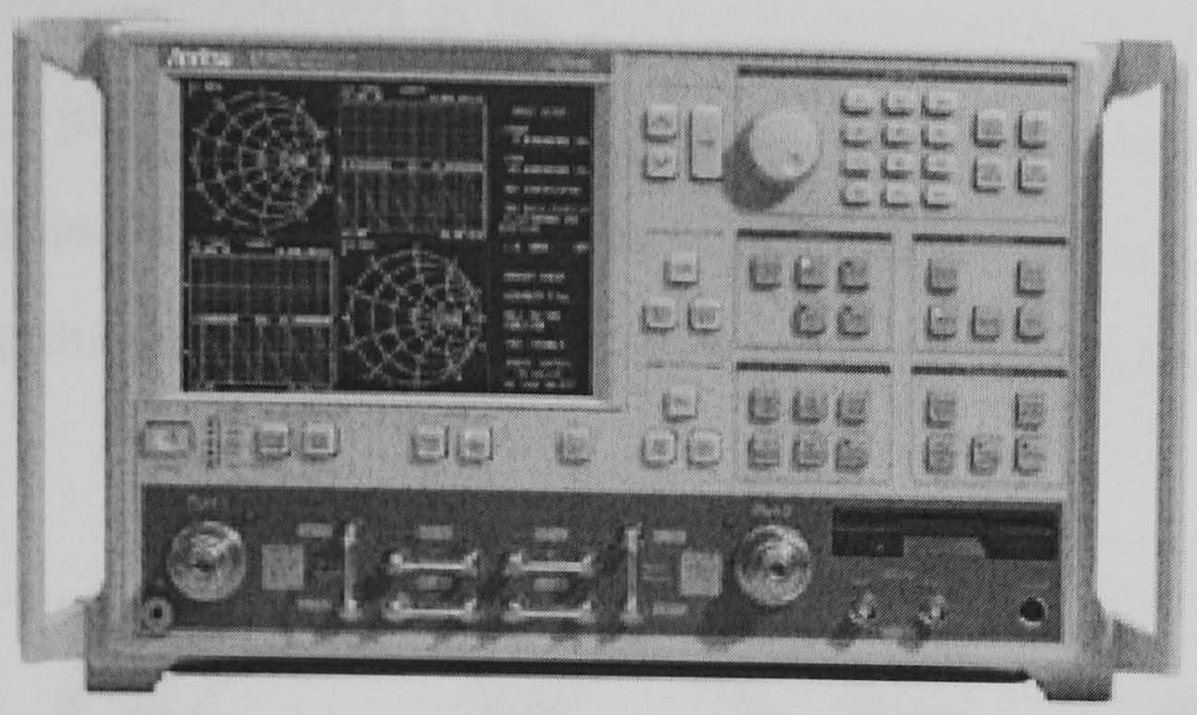

Fig. 5.8 Anritsu Lightning ™ 37000D Vector Network Analyser.

5.3.2 Measurement Results

Initially, the measurement uses structures with 2, 3, 4 elements and 15mm-long transmission lines. Magnitude and phase of S-parameters are shown in Fig. 5.9 – Fig. 5.12. Unexpected modes appear at about 14GHz and 18GHz because of the existence of the connectors and the direct coupling between the two lines at these frequencies. To minimise these effects, the feeding transmission lines are shortened to be 11mm. A vertical metal plate is also placed between the two "monopole antennas" at a distance from the board to reduce the coupling through the air

The measured magnitude of S-parameters for the 2-element structure with 11mm feeder lines and vertical metal plate is displayed in Fig. 5.13. The first mode at 9-10GHz and the second mode at 20-23GHz clearly appear as they are estimated in the software simulation. Reduced transmission in the lower frequency range of the left-handed mode can be observed as was described in Chapter 5.2.3. The extra mode produced by the connector effect can still be found at about 17 GHz, however it is now weakened. .

Similarly, measured S-parameters of the 3-element structure with 11mm feeder lines and vertical metal plate are also shown in Fig. 5.14. Compared with that of 2-element structure, greater insertion loss occurs for every mode, which is because of the longer distance between the ends of microstrip lines and more left-handed material elements inserted.

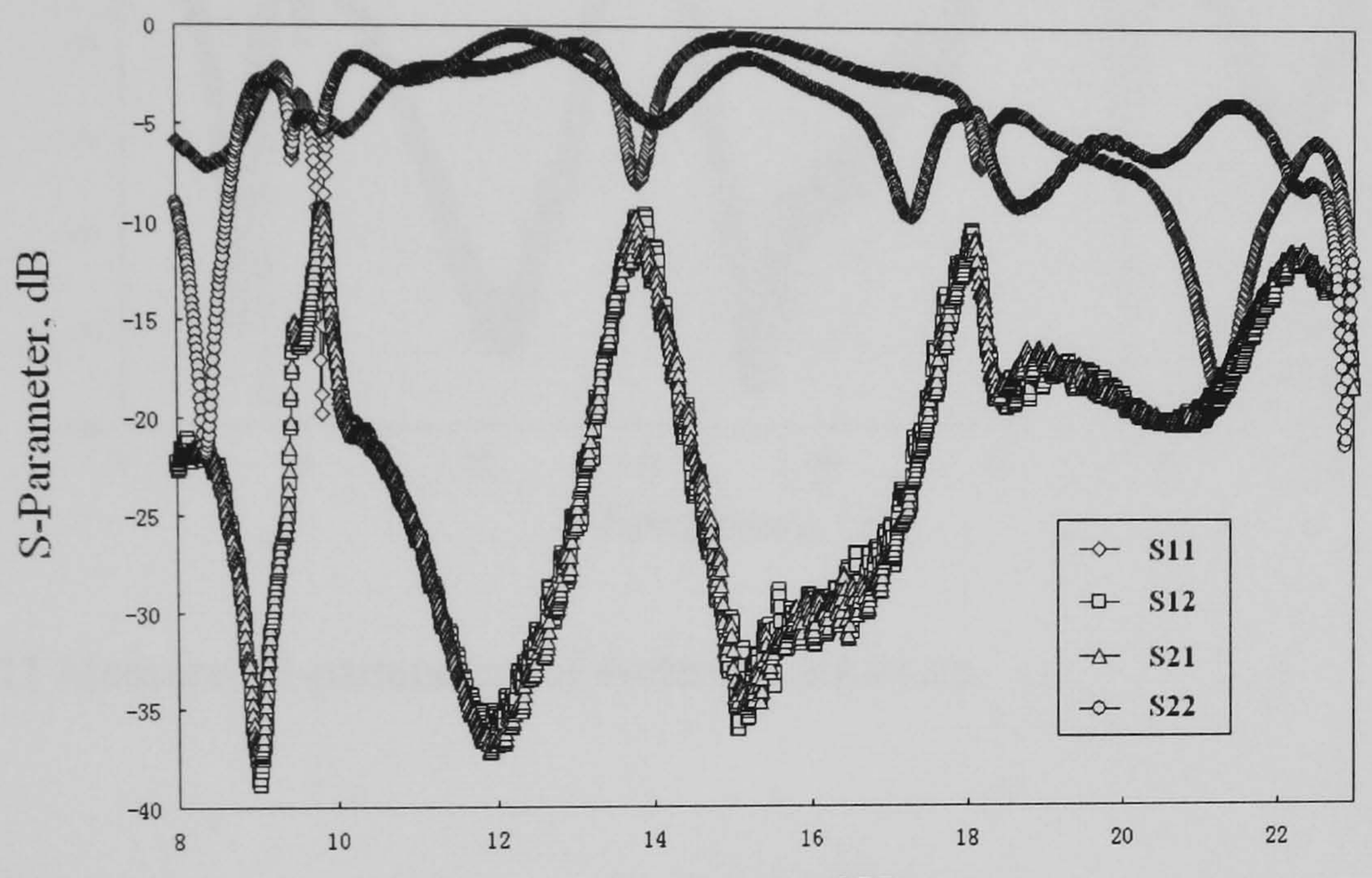

Fig. 5.9 Measured S-parameters of 2-element structure.

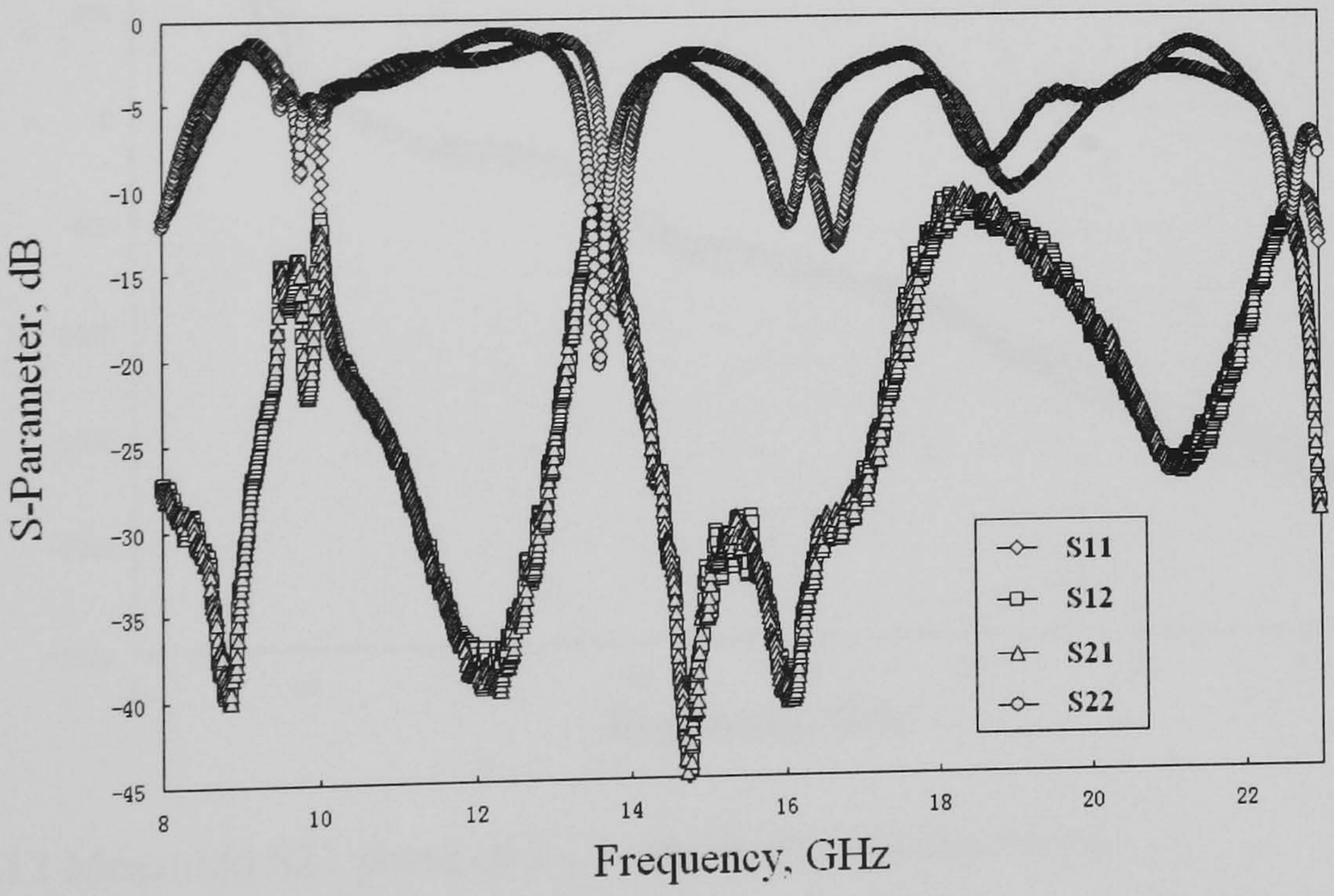

Fig. 5.10 Measured S-parameters of 3-element structure.

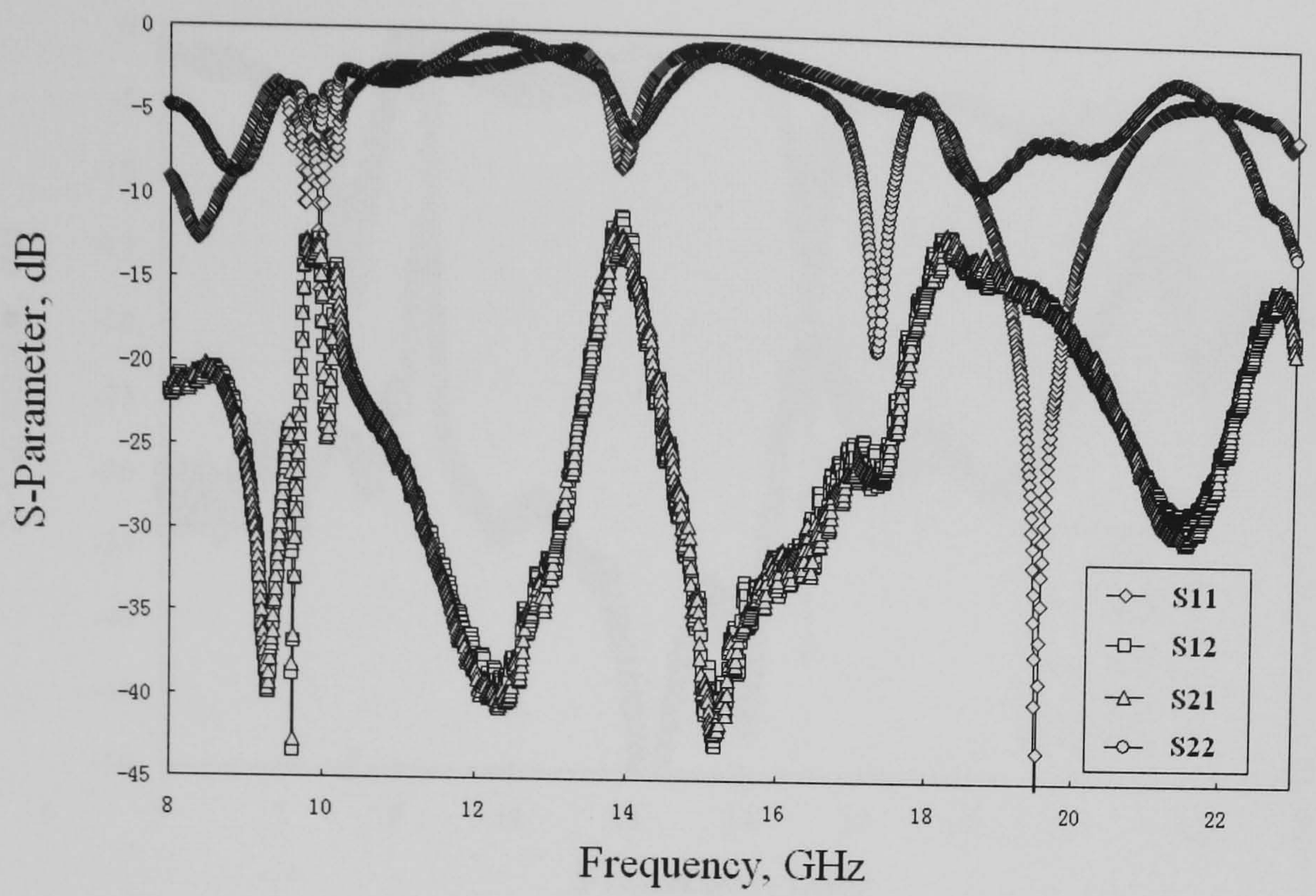

Fig. 5.11 Measured S-parameters of 4-element structure.

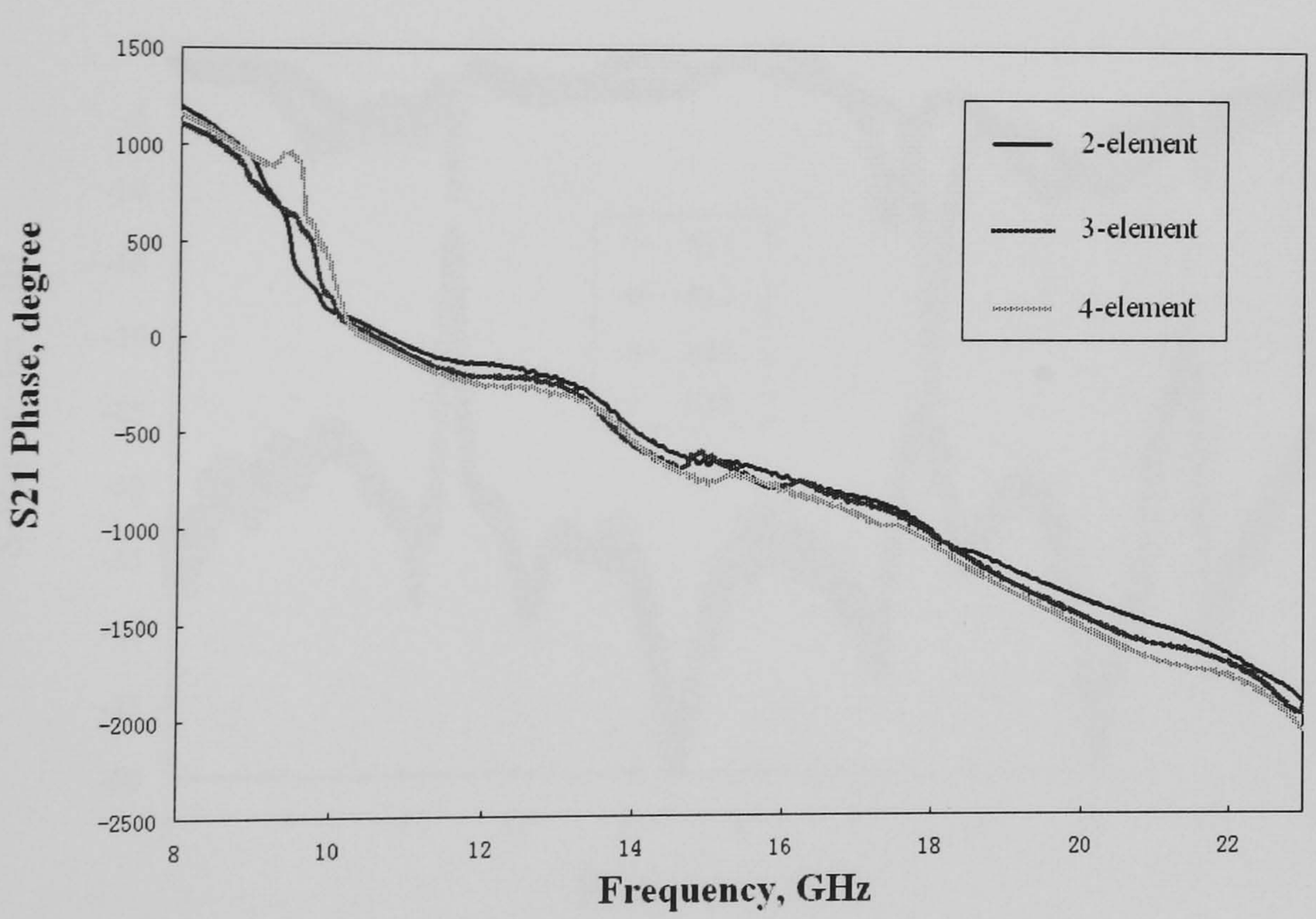

Fig. 5.12 Measured S21 phase of 2-, 3- and 4-element structures.

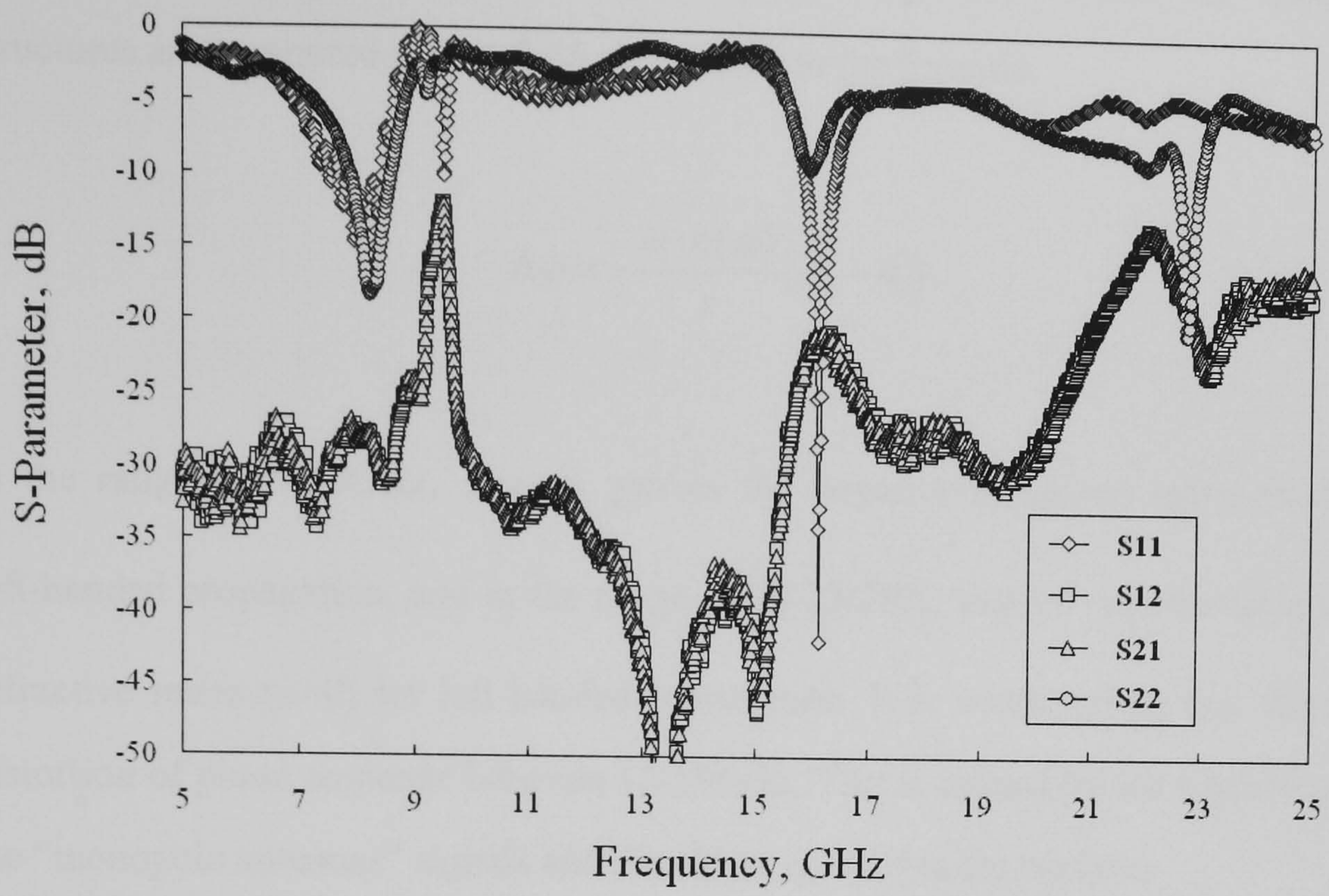

Fig. 5.13 Measured S-parameters of 2-element structure with metal plate.

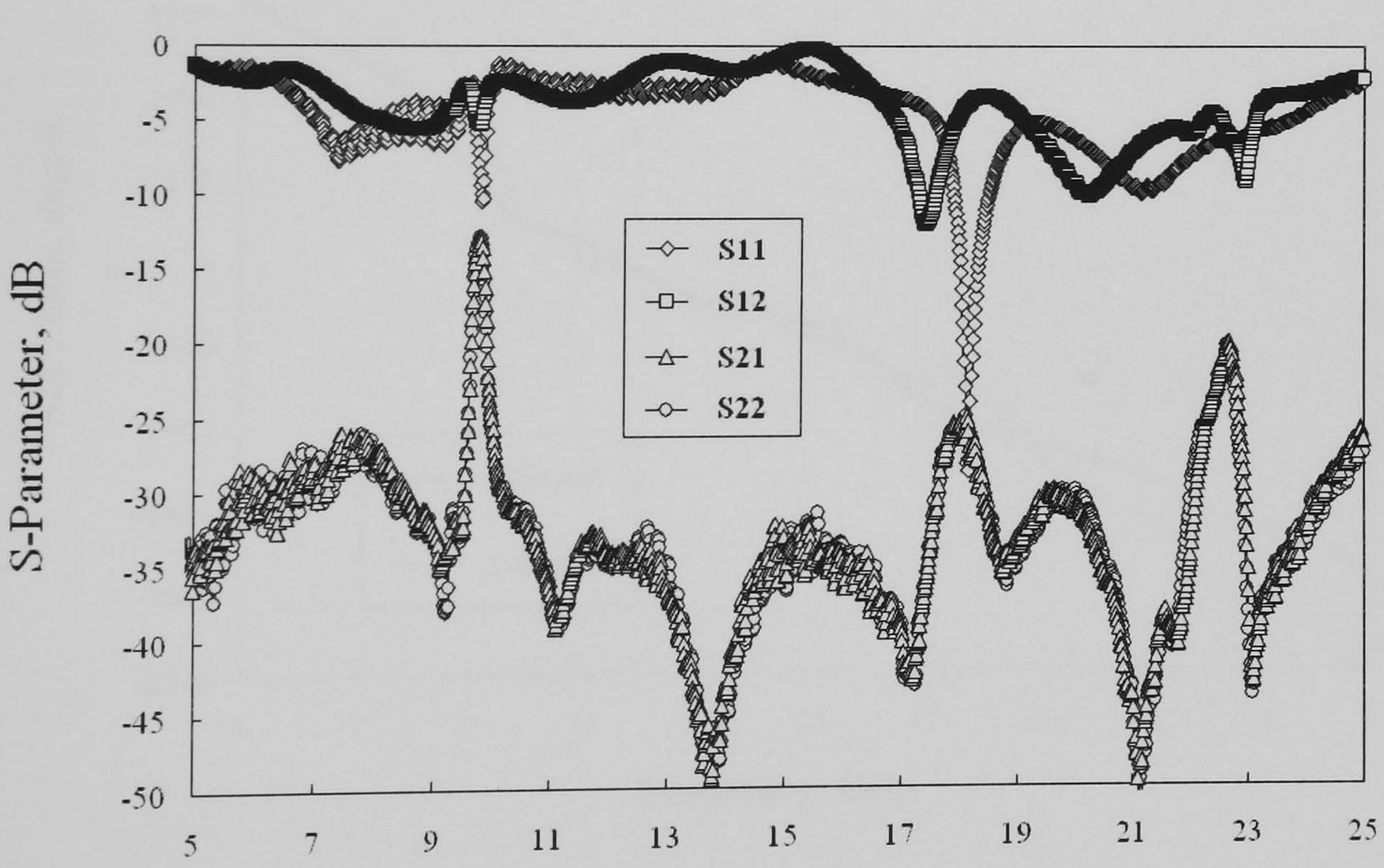

Fig. 5.14 Measured S-parameters of 3-element structure with metal plate.

Using the method in Chapter 4.5.2, the phase responses of S21 for these two structures are compared in Fig. 5.15. According to the formula

$$\Delta\varphi = -\frac{\omega \cdot n(\omega)}{c}(d_2 - d_1) \tag{5.3}$$

in the range of 9-10GHz, $\Delta\varphi > 0$ proves the negative refractive index (n<0) for left-handed propagation, and in the range of 20-23GHz, $\Delta\varphi < 0$ proves the positive refractive index (n>0) for left-handed propagation. It is worth noting that there is a distortion of phase response between 15-19GHz. This is caused by the interference of the "monopole antennas" signals and should be ignored in the analysis.

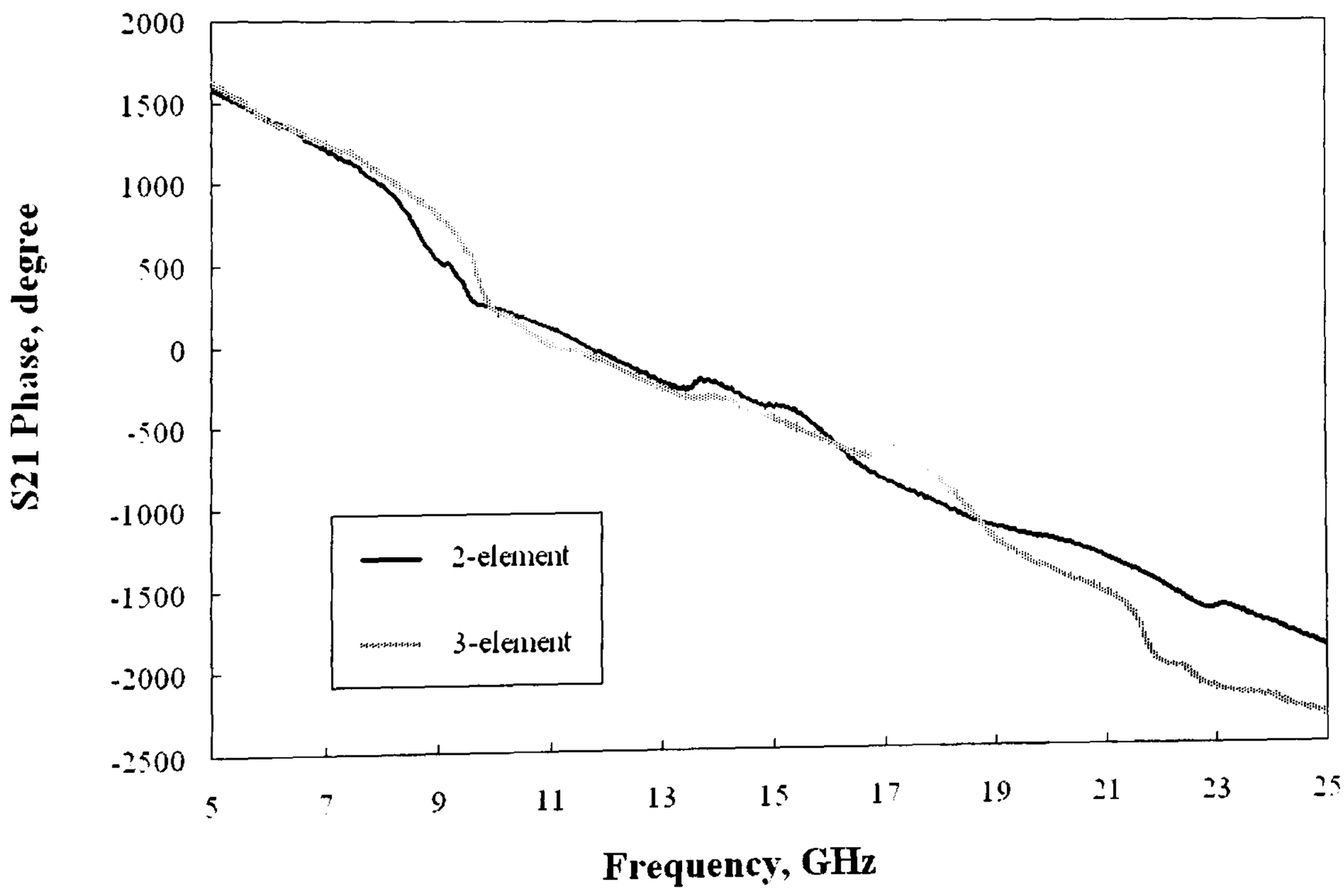

Fig. 5.15 Measured S21 phase of 2- element and 3-element structures with metal plate.

5.3.3 Highlighted LH Transmission

To highlight the LH transmission of the LH metamaterials, longer LH transmission-line structures like those in Fig. 5.7 are simulated in the commercial software HFSS. With the same configuration corresponding to Fig. 9 to Fig. 12, the LH transmission-line structures are fed by 15mm-long microstrip-lines. The numbers of the spiral elements are 2, 6 and 10. The phases of the transmission responses are presented in Fig. 5.16. Larger step of the element numbers makes the LH transmission more clear than those in Fig. 12 and Fig.15.

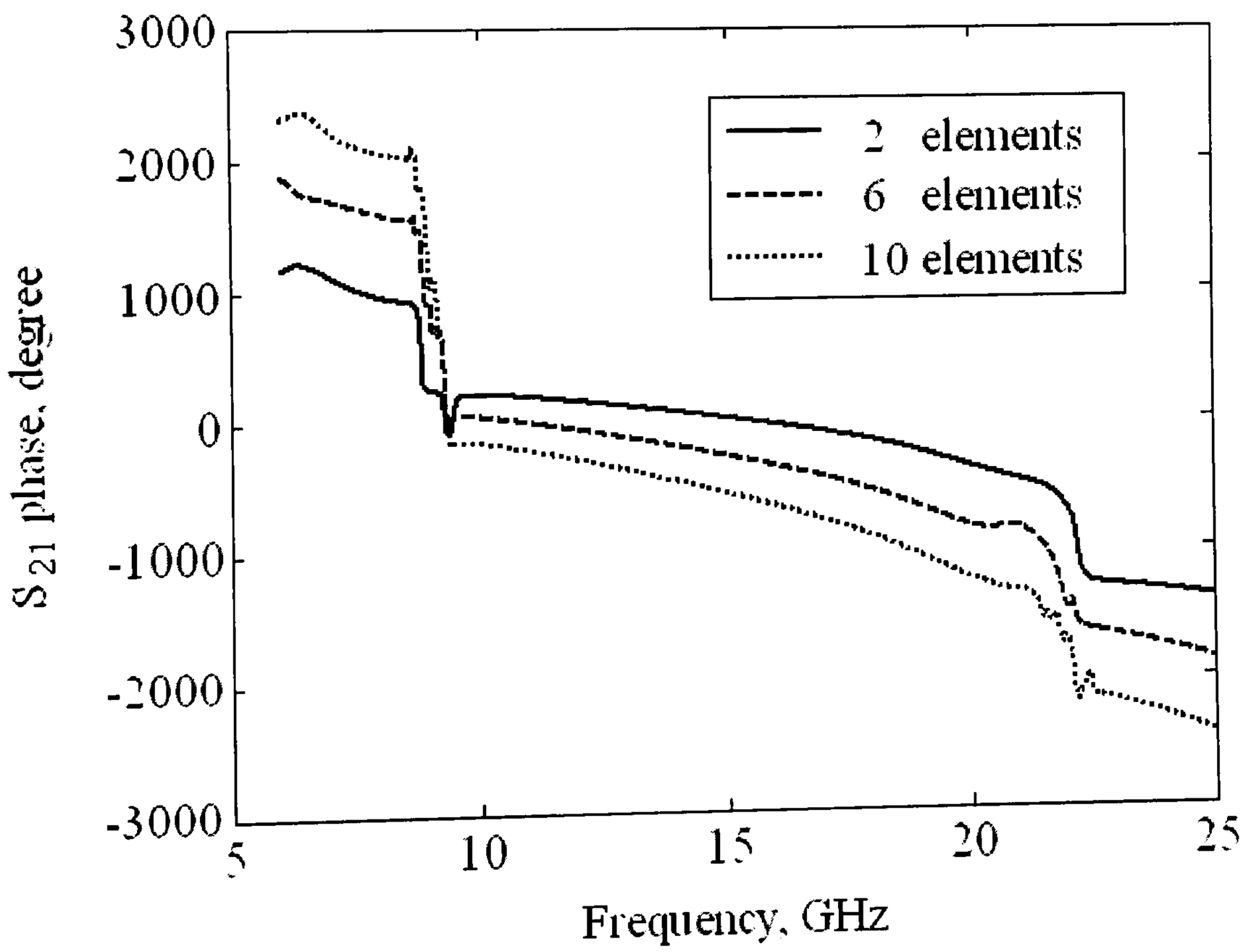

Fig. 5.16 Simulated S21 phase of 2-, 6- and 10-element structures.

5.5 Conclusions

The measurement of the planar left-handed materials are designed and set up in this chapter to validate the negative phase velocity propagation. Practical structures comprised of microstrip lines with the planar left-handed materials in the middle are used to assess surfaces wave propagations within the frequency ranges of the left-handed and right-handed modes. To meet the requirement of impedance matching, the microstrip lines are tapered at the ends towards the left-handed materials. S parameters are obtained in the simulations and measurements. Left-handed propagation through the planar left-handed materials is proved in two ways: the simulated animation of the electric fields inside the dielectric substrate that clearly shows a wavefront travelling in reversed direction with the energy flow, which indicates that the phase velocity and the group velocity are anti-parallel; and the comparison of the transmission phase in actual measurements similar with those in chapter 4. Parasitic modes are found in the experimental measurement. To weaken these unwanted effects, the feeding microstrip lines are shortened, and a vertical metal plate is putting between the feeders to impair their coupling. A software simulation of the measured structures with larger step of the elements is also given out to highlight the LH transmission better.

References

[1] O. F. Siddiqui, M. Mojahedi and G. V. Eleftheriades, "Periodically Loaded Transmission Line With Effective Negative Refractive Index and Negative Group Velocity", *IEEE Trans. Antennas Propagat.*, Vol. 51, no. 10, pp 2619-2625, 2003

[2] C.-Y. Cheng and R. W. Ziolkowski, "Tailoring Double-Negative Metamaterial Responses to Achieve Anomalous Propagation Effects Along Microstrip Transmission Lines", *IEEE Trans. Microwave Theory Tech.*, Vol. 51, no. 12, pp. 2306 – 2314, 2003

[3] C. Caloz and T. Itoh, "Transmission line approach of left-handed (LH) materials and microstrip implementation of an artificial LH transmission line", *IEEE Trans. Antennas Propagat.*, Vol. 52, no. 5, pp. 1159-1166, 2004

[4] D. M. Pozar, *Microwave Engineering*, Second Edition, John Wiley & Sons, Inc., New York, 1998

[5] *High Frequency Structure Simulator* (HFSS), ver. 9.0, Ansoft Corporation, 2003

[6] *Anritsu Lightning™ 37000D Vector Network Analyser Manual*, Anritsu, 2004

6. Conclusions

6.1 Summary

Novel advanced numerical techniques are introduced in this thesis to analyse the properties of novel planar metamaterials. Metamaterials are periodic metallodielectric structures and functionally classified as Frequency Selective Surfaces (FSS), Electromagnetic Band Gap Materials (EBG), Artificial Magnetic Conductors (AMC) and Left-handed Materials (LHM). Traditional methods to analyse these structures in frequency domain usually adopt Method of Moments (MoM) with electric field integral equations (EFIE) using entire-domain and rooftop sub-domain basis functions in the modelling of the elements. Periodic Green's function in spectral domain is used for the periodicity. The MoM equations are solved at every point in the studied frequency range. Recently, some new-type metamaterials with complex element

shapes, e.g. the miniaturised electromagnetic band-gap materials and the left-handed materials, have been introduced into the metamaterial family by other researchers. To model these complex-shape elements exactly, sub-domain triangular-patch basis function, which is also known as Rao-Wilton-Glisson (RWG) basis function, is used in replacement of the entire-domain and rooftop basis functions. Moreover, homogeneous version of MoM equations is solved to analyse the surface-wave responses of these materials by plotting the dispersion diagrams. Unlike the resonant behaviours and rapid frequency variations of the currents and fields, the impedance matrix elements usually have a regular and smooth variation versus frequency. That makes it possible to calculate the impedance matrix at only few frequency points and get the impedance matrix at other points of the remaining frequency range of interest using interpolation, which could drastically accelerate the computing. This technique can be applied to derive the transmission and reflection responses for plane waves as well as the dispersion diagrams for surface waves in this thesis. The research work to analyse and design novel electromagnetic metamaterials is mainly based on these techniques.

Miniaturised and multiband EBG and AMC surfaces were designed in Chapter 3. Three tripole-based examples as periodic-loaded tripole, fractal tripole and convoluted tripole arrays were introduced to meet the requirement of miniaturisation and multi-resonance. Fractal tripole arrays were studied in detail to explain how the higher order resonances are generated by adding higher order fractal branches into the original tripole array. Plane-wave response, surface current and dispersion diagram were derived in the analysis using the efficient modelling techniques introduced above. The features of miniaturisation and multiband were achieved according to the results of the calculation and the measurement. The numerical errors were discussed. Computational predictions were also verified by comparing with experimental results.

In Chapter 4, novel planar left-handed metamaterials were designed. A study was carried out with regards to the effect of the interpolation step on the accuracy of the results. According to the error analysis, the dispersion diagrams of the proposed structures have been produced with an interpolation step of 1GHz which resulted in a good accuracy. The method was validated by comparison with commercial software (HFSS). The refraction index of the structures has been derived. A thorough investigation of the modal field distribution provided a detailed explanation of the left-handed properties of the structures based on the dual transmission line concept. A full-wave based validation of the left-handedness has been presented. The unit cell is as small as $\lambda/24$ which allows for an equivalent effective medium model. The structures are simple, compatible with low-cost fabrication techniques and scalable to higher frequencies.

In order to prove the feasibility of the designs in Chapter 4, a measurement of the planar left-handed materials are designed and set up in Chapter 5 to validate the negative phase velocity propagation. Microstrip lines with the replacement of the planar left-handed materials in the middle are used to support the surfaces wave propagations within the frequency ranges of the left-handed and right-handed modes. To meet the requirement of impedance matching, the microstrip lines are tapered at the ends towards the left-handed materials. S parameters are obtained in the simulations and in measurement. Left-handed propagation through the planar left-handed materials is proved by means of the simulated animation of the electric fields inside the dielectric substrate and the comparison of the transmission phases for sections of different length in the measurement.

6.2 Future Work

Advanced numerical techniques in modelling of novel electromagnetic metamaterials have been introduced in this thesis. The techniques are concerned with single-layer planar periodic structures over grounded dielectric substrate. However, with the rapid development of the radio design, more requirements have been brought out to the numerical approaches for the analysis and design of metamaterials.

Large-scale integrated circuit in radio frequency is a trend in modern radio system design. Multi-layered structures play more and more important roles especially in the area of Microwave Monolithic Integrated Circuit (MMIC) and Multi-Chip Module (MCM) designs. This requires the modelling techniques to be applicable to multi-layered metamaterials. To meet this requirement, the Green's functions (2.41) and (2.42) need to be improved as the closed-form Green's functions of multi-layer in [1]-[5].

Moreover, as what has been introduced in Chapter 3, miniaturised and multiband features are required in modern wireless communication systems. With the growth of the printed circuit techniques, much more complex and finer metamaterials appear in recent years. This brings a heavy burden to the frequency-domain numerical techniques to deal with enormous impedance matrices with tens of thousands elements. Computing time and computer memory will face big challenges even at a single frequency calculation. Thus, techniques such as Multilevel Fast-Multipole Algorithm (MLFMA) [6], [7] and Adaptive Basis Functions / Diagonal Moment Matrix (ABF/DMM) [8] should be adopted to create sparse or diagonal impedance matrices, which could greatly reduce the size of the problems.

Besides, due to the novelty of the metamaterials especially the left-handed materials, the application of these materials in radio frequency design is a key point to be regarded. Although some applications have been proposed recently [9]-[18], the remaining potential of metamaterials is still to be exploited.

Reference

[1] M. J. Tsai, F. D. Flaviis, O. Fordham and N. G. Alexopoulos, "Modeling Planar Arbitrary Shaped Microstrip in Multilayered Media", *IEEE Trans. Microwave Theory Tech.*, Vol. 45, no. 3, pp. 330-337, 1997

[2] G. Dural, and M. I. Aksun, "Closed-Form Green's Functions for General Sources and Stratified Media", *IEEE Trans. Microwave Theory Tech.*, Vol. 43, no. 7, pp. 1545-1552, 1995

[3] R. A. Kipp and C. H. Chan, "Complex Image Method for Sources in Bounded Regions of Multilayer Structures", *IEEE Trans. Microwave Theory Tech.*, Vol. 42, no. 5, pp. 860-865, 1994

[4] Y. L. Chow, J. J. Yang, D. G. Fang, and G. E. Howard, "A Closed-Form Spatial Green's Function for the Thick Microstrip Substrate", *IEEE Trans. Microwave Theory Tech.*, Vol. 39, no. 3, pp. 588-592, 1991

[5] P. Yla-Oijala, and M. Taskinen, "Efficient Formulation of Closed-Form Green's Functions for General Electric and Magnetic Sources in Multilayered Media", *IEEE Trans. Antennas Propagat.*, Vol.51, no. 8, pp. 2106-2115, 2003

[6] J. M. Song and W. C. Chew, "Multilevel Fast-Multipole Algorithm for Solving Combined Field Integral Equations of Electromagnetic Scattering", *Microwave Opt. Technol. Lett.*, Vol. 10, pp. 14-19, 1995

[7] Z. Liu, J. He, Y. Xie, A. Sullivan, and L. Carin, "Multilevel Fast Multipole

Algorithm for General Targets on a Half-Space Interface", *IEEE Trans. Antennas Propagat.*, Vol. 50, no. 12, pp 1838-1849, 2002

[8] M. L. Waller and S. M. Rao, "Application of Adaptive Basis Functions for a Diagonal Moment Matrix Solution of Arbitrary Shaped Three-Dimensional Conducting Body Problems", *IEEE Trans. Antennas Propagat.*, Vol. 50, no. 10, pp 1445-1452, 2002

[9] M. A. Antoniades, G. V. Eleftheriades, "Compact Linear Lead/Lag Metamaterial Phase Shifters for Broadband Applications", *IEEE Antennas Wireless Propag. Lett.*, Vol. 2, pp. 103-106, 2003

[10] S. Lim, C. Caloz, T. Itoh, "Metamaterial-Based Electronically Controlled Transmission-Line Structure as a Novel Leaky-Wave Antenna with Tunable Radiation Angle and Beamwidth", *IEEE Trans. Microwave Theory Tech.*, Vol. 53, no. 1, pp. 161–173, 2005

[11] H. Kim; A. B. Kozyrev, A. Karbassi, and D. W. van der Weide,"Linear Tunable Phase Shifter Using a Left-Handed Transmission Line", *IEEE Microwave and Wireless Components Letters*, Vol. 15, no. 5, pp. 366-368, 2005

[12] M. A. Antoniades, G. V. Eleftheriades, "A Broadband Wilkinson Balun Using Microstrip Metamaterial Lines", *IEEE Antennas Wireless Propag. Lett.*, Vol. 4, pp. 209-212, 2005

[13] M. A. Antoniades, G. V. Eleftheriades, "A Broadband Series Power Divider Using Zero-Degree Metamaterial Phase-Shifting Lines", *IEEE Microwave and Wireless Components Letters*, Vol. 15, no. 11, pp.808-810, 2005

[14] Islam, R., Elek, F. and Eleftheriades, G. V.: "Coupled-line metamaterial coupler having co-directional phase but contra-directional power flow", *Electronic Letters*, Vol. 40, pp. 315-317, 2004

[15] Islam, R. and Eleftheriades, G. V.: "Phase-agile branch-line couplers using metamaterial lines", *IEEE Microwave and Wireless Components Letters*, Vol. 14, pp. 340-342, 2004

[16] C. Caloz, A. Sanada, and T. Itoh, T.: "A novel composite right-/left-handed coupled-line directional coupler with arbitrary coupling level and broad bandwidth", *IEEE Trans. Microwave Theory and Techniques*, Vol. 52, pp. 980-992, 2004

[17] L. Liu, C. Caloz, and T. Itoh, "Dominant mode (DM) leaky-wave antenna with backfire-to endfire scanning capability", *Electronic Letters*, Vol. 38, pp. 1414-1416, 2000

[18] A. Sanada, M. Kimura, I. Awai, H. Kubo, C. Caloz, and T. Itoh,: "A planar zeroth order resonator antenna using left-handed transmission line", *European Microwave Conference Digest*, Vol. 2, pp. 1341-1344, 2004